Superconductivity in AuGeNi Ohmic contacts to a GaAs-based high mobility two-dimensional electron gas

Christopher Brian Beauchamp

Supervisor: Dr James Nicholls

Thesis submitted in part fulfilment of the requirement for the degree of Doctor of Philosophy from Royal Holloway, University of London

Declaration of Authorship

I, Christopher Brian Beauchamp, hereby declare that this thesis and the work presented in it is entirely my own. Where I have consulted the work of others, this is always clearly stated.

_____ _____

Christopher Brian Beauchamp Date

I dedicate this thesis to my God who made this happen by His grace and mercy, to my children who will reap the benefit of this and to Gemma who was a constant source of love and support. Despite my behaviour and the way I have treated her, her steadfast patience, dedication, kindness and thoughtfulness measures beyond words; she is a fantastic wife and mother and deserves all the praise for supporting this work.

בָּרוּךְ אַתָּה יְיָ אֱלֹהֵינוּ מֶלֶךְ
הָעוֹלָם שֶׁהֶחֱיָנוּ וְקִיְּמָנוּ
וְהִגִּיעָנוּ לַזְּמַן הַזֶּה

Baruch Atah Adonai Eloheinu, melech
ha-olam, shehecheyanu, vikiyemanu
vehigiyanu lazman hazeh.

Blessed are You, Adonai our God, ruler
of the world, who has given us life, sustained us,
and brought us to this time.

Acknowledgements

As I stand atop the craggy, weather beaten, misty mountain, that is this PhD and stare into the precipice of what comes next, I am grateful for those who have brought me here; it marks the end of a decade long crumbly road, inspired by a dream and has been a journey of learning how much I do not know.

This, in many ways, is a bittersweet moment closing a chapter of my life that may have had a different ending. It has been a humbling experience filled with many emotions, including many mistakes, many trials, many losses and many gains. As a result, I have changed enough to know that I have to confront problems and cannot simply runaway; a PhD is a great lesson in problem solving and conquering tribulations, but I have also learned there are some problems you just cannot solve. In the overall time I have spent studying, my young family grew from one child to four, two of which I delivered myself at home, this is my greatest achievement.

This PhD has been a truly life-changing experience for me and it would not have been possible to do without the support and guidance that I received from so many people.

Firstly, I would like to say a very big thank you to my supervisor Dr. James Nicholls, without whom this PhD would not have happened at all. I am extremely grateful for his selflessness, kindness, invaluable advice, continuous support, and patience during my PhD study. His immense knowledge and experience has been an encouragement and without his guidance and constant feedback, this PhD would not have been achievable.

I would also like to thank Dr. Andrew Casey for the use of ND4, Professor Brian Cowan for many conversations and Terje Theisen for proof reading this thesis .

Of course, I would like to express my extreme gratitude to the Matts' for their support in the early years, my parents, my wife and my children, without their tremendous understanding, patience and encouragement, it would be impossible for me to complete my study.

Finally, I thank the Lord God Almighty and I commit these works to Him.

Abstract

The initial aim of this thesis was to cool two-dimensional electrons down to temperatures below $10\,\mathrm{mK}$. In order to cool a high mobility two-dimensional electron gas (2DEG) at a GaAs–AlGaAs heterojunction to milliKelvin temperatures, different processing techniques and recipes for low resistance Ohmic contacts based on alloys of Au, Ni, and Ge are fabricated on these semiconductor devices. Scanning electron microscope (SEM) and Energy Dispersive X-ray (EDX) images establish that the Ohmic contacts have the same inhomogeneous microstructure observed in the literature.

The unexpected result from electrical measurements of the contact resistance R_C, the four-terminal resistance along the top of a single contact R_{top}, and the vertical resistance R_V, is that there is superconductivity in the Ohmic contact below $0.9\,\mathrm{K}$. Measurements for different Ohmic contacts investigated, show some have multiple superconducting transitions, whereas others have a single transition; there is no correlation discovered between the annealing recipe and the number of transitions. $I-V$ measurements show the superconductor is turned completely normal with a DC current of $2.1\,\mathrm{mA}$ and in a magnetic field, the superconductor is turned completely normal with a magnetic field of $0.15\,\mathrm{T}$.

This thesis speculates on the superconductor, suggesting that the Ohmic contact is a granular superconductor comprised of multiple alloys of different phases, and reviews the possible compounds that may be superconducting below $0.9\,\mathrm{K}$.

There is a discussion on how this superconductivity affects electrical transport measurements in similar systems such as quantum conductance, four-terminal Hall measurements and electron cooling experiments in 2DEGs below $0.1\,\mathrm{K}$.

Publications

C. B. Beauchamp *et al* "Superconductivity in AuNiGe Ohmic contacts to a GaAs-based high mobility two-dimensional gas", *Applied Physics Letters*, vol. **117**, p. 162104, (2020).

Contents

List of Figures

List of Tables

Chapter 1

Introduction

1.1 Cooling electrons in low-dimensional systems

In the pursuit to discover new many-body states in low-dimensional electron systems, two-dimensional electron gas (2DEG) devices are cooled to the lowest possible temperature T; extreme cooling of 2DEGs is necessary to study many fundamental physical phenomena, such as Tomonaga-Luttinger liquids[1], the Kondo effect [2] or fractional quantum Hall states[3] where a low electron temperature T_e is needed.

However, it remains challenging to cool the conduction electrons below $10\,\mathrm{mK}$. When trying to cool the 2DEG to ultra low temperatures, experimentalists face many unfavourable physical scaling laws; the heat capacity of the conduction electrons falls with temperature, as does their thermal coupling to other electronic systems and to phonons in the host lattice.

At low temperature the lattice and electrons thermally decouple, and if there is a heat leak to the electrons they heat up to an electron temperature T_e that is higher than the lattice temperature T_L; when the temperature decreases, the thermal coupling between conduction electrons and the host lattice weakens and the heat capacity of the electronic system falls. This makes T_e more sensitive to parasitic heating[4].

To understand how the electrons are cooled, Joule heating the electron gas with a power P is used. In this way, the electrons thermalise at a temperature T_e and the rate at which they lose their excess energy to the lattice at T_L is expressed as,

$$P = \dot{Q}(T_e) - \dot{Q}(T_L). \tag{1.1}$$

From Appleyard *et al*[4] it was experimentally shown that,

$$\dot{Q}(T) = aT^5 + bT^2 \tag{1.2}$$

where the T^5 term is electron-phonon cooling and the T^2 term is cooling via the Ohmic contacts; at high T, T^5 dominates, but when $T < 100\,\mathrm{mK}$ the electrons are mainly cooled through the Ohmic contacts. Therefore, when $T > 100\,\mathrm{mK}$ the most important term is T^5.

To achieve T_e that is close to the base T of the cryostat requires strong thermal coupling, achieved by minimising the contact resistance R_C between the 2DEG and the Ohmic contact [5]. The lowest reported 2DEG temperature is $T_e \approx 6\,\mathrm{mK}$ [6] measured using three in situ primary thermometers, but its in a magnetic field and cooling in the the quantum Hall regime is different to cooling in zero magnetic field.

In the literature, it is assumed that Ohmic contacts do not change their electrical characteristics as a function of temperature during experiments[7], however, this thesis shows and characterises the unexpected discovery that AuGeNi Ohmic contacts become superconducting when $T < 1\,\mathrm{K}$.

1.2 Outline of the thesis

The chapter outline of this thesis is as follows:

- **Chapter two** presents the underlying engineering and physics beginning with a discussion on two-dimensional electron gases, the samples used in this thesis. Following this, the physics and principles of Ohmic contacts are given. The chapter finishes off with a basic synopsis of superconductivity.

- In **Chapter three**, the fabrication of two-dimensional electron gas devices is reviewed this includes wafer characteristics, Ohmic contact processing conditions and Ohmic contact microstructure.

- **Chapter four** discusses the low-temperature experimental techniques used to obtain the measurements. The chapter discusses the dilution refrigerator and $4.2\,\mathrm{K}$ Dewar, the diagnostic thermometry and the electrical transport measurement circuits applied such as four-terminal and two-terminal circuits.

- **Chapter five** investigates the resistance of different-shaped devices by simulation using the partial differential equation PDE solver, FlexPDE. Within this chapter, simulations are made for a $4\,\mathrm{mm} \times 4\,\mathrm{mm}$ device, a key device in the used to cool electrons to ultra low temperatures.

- **Chapter six** shows experimental evidence of superconductivity in AuGeNi Ohmic contacts. Results are presented for the Ohmic contact resistance R_C, the vertical resistance R_V, and the resistance R_{top} along the top of the contact.

- **Chapter seven** shows R_V and R_{top} $I-V$ and dV/dI measurements of the superconductor, with notable measurements of the critical current and magnetic field data.

- **Chapter eight** speculates on: possible candidates for the superconductor, the effect superconducting AuGeNi Ohmic contacts have on future electron cooling experiments and the effect AuGeNi superconducting Ohmic contacts have on other transport measurements.

- **Chapter nine**, discusses future work and outlook. The chapter summarises how the initial aim of the thesis, cooling low dimensions electrons down, is impacted by the unexpected results in the project and suggestions are then made for future work to overcome the problems encountered in this field of research.

Chapter 2

Physics background

2.1 Introduction

This chapter presents an overview of the physics in this thesis, this includes two-dimensional electron gases (2DEGs) fabricated in a GaAs/AlGaAs heterostructure, Ohmic contacts, which give electrical connections to the 2DEG, and superconductivity.

2.2 Two-dimensional electron gas systems

A 2D sheet of electrons confined to two-dimensions is known as a two dimensional electron gas (2DEG). In this section, we discuss the basic concepts and principles of electron transport in these systems and how this is modified in the presence of a magnetic field B. We begin with describing how quantum confinement of electrons is achieved and then, in order to interpret correctly the transport properties, the physics is covered.

2.2.1 Electron confinement

If there exists a 3D box of non-interacting electrons in a volume $V = L_x \times L_y \times L_z$, the solution of the 3D time-independent Schrödinger equation is

$$E\Psi(\mathbf{r}) = [-\frac{\hbar^2}{2m}\nabla^2 + V(r)]\Psi(\mathbf{r}), \tag{2.1}$$

where $\mathbf{r} = (x, y, z)$ is the position vector and $\mathbf{k} = (k_x, k_y, k_z)$ is the wavevector given by

$$\Psi(\mathbf{r}) = \frac{1}{\sqrt{V}} e^{(\mathrm{i}\vec{\mathbf{k}}\cdot\vec{\mathbf{r}})}. \tag{2.2}$$

The Schrödinger equation can be solved to give eigenvalues of the form

$$E_k = \frac{\hbar^2 k^2}{2m^\star} = \frac{\hbar^2}{2m^\star}(k_x^2 + k_y^2 + k_z^2), \tag{2.3}$$

where $m^\star$ is the effective mass of the electron.

If the sample dimension in the z-direction is such that $L_z < \lambda_F$, where λ_F is the Fermi wavelength, the system is considered as 2D. The electron eigenstate in a 2DEG is a plane wave for motion in xy-plane and shows confinement in the z-direction as,

$$\Psi(\mathbf{r}) \propto e^{ik_x x} e^{ik_y y} u(z). \tag{2.4}$$

As the Schrödinger equation reduces to its 1D form in the z variable

$$\epsilon u(z) = \left[-\frac{\hbar^2}{2m^\star} \frac{d^2}{dz^2} + V(z) \right] u(z), \tag{2.5}$$

where ϵ is the energy of the 2D subband, the electron energy is given by the dispersion relation

$$E_{n,k} = E_n + \frac{\hbar^2}{2m^\star}(k_x^2 + k_y^2), \tag{2.6}$$

where k_x, k_y are the in-plane wavevectors and E_n is the quantised energy corresponding to $u_n(z)$. For each bound state n, there is a continuum of states associated with free motion in the xy-plane; the dispersion relation gives a parabola for each value of integer n.

2.2.2 Density of states

The density of free electron states in 1D, 2D and 3D is defined as

$$g(E) = \frac{dn}{dE}, \tag{2.7}$$

where g(E) is the number of available states per unit energy per unit volume and is also called the density of available states per unit energy; the number of electrons available at the Fermi energy $g(E_F)$ determine all the physical properties of a metal[8].

Whatever the dimension d ($d = 0 - 3$) the density of states (DOS) can be written as

$$g(E) = \frac{dn}{dE} = \frac{dn}{dk} \times \frac{dk}{dE} = g(k) \times \frac{dk}{dE}, \tag{2.8}$$

and the kinetic energy of free electrons is given by,

$$E = \frac{\hbar^2 k^2}{2m}, \tag{2.9}$$

so,

$$\frac{dk}{dE} = \left(\frac{dE}{dk}\right)^{-1} = \frac{m^\star}{\hbar^2 k}, \tag{2.10}$$

and thus, Eq. 2.8 becomes

$$g(E) = \frac{dn}{dE} = \frac{dn}{dk} \times \frac{dk}{dE} = g(k)\frac{m^\star}{\hbar^2 k}. \tag{2.11}$$

In thermal equilibrium, electrons occupy the available states according to the Fermi-Dirac statistics described by,

$$f_0(E, E_F, T) = \left[1 + e^{\left(\frac{E-E_F}{k_B T}\right)}\right]^{-1}, \tag{2.12}$$

where E_F is the Fermi energy, T is the temperature, and k_B is the Boltzmann constant. At low T, the Fermi function turns into

$$f_0(E, E_F, T) \xrightarrow[T\to 0]{} \Theta(E_F - E), \tag{2.13}$$

This is the *degenerate limit* of an electron gas and all the states with energy lower than the Fermi energy, $E \leq E_F$, are occupied.

In GaAs/AlGaAs systems the energy separation between the 2D subbands is , $E2 - E1 \approx 25\,\mathrm{meV}$, so only one 2D subband is occupied. The electrons behave two-dimensionally, with a single step-like density of states written as

$$n_{2D} = \frac{m^\star}{\pi\hbar^2}\int_0^\infty \Theta(E - E_1)\Theta(E - E_F)dE = \frac{m^\star}{\pi\hbar^2}(E_F - E_1), \tag{2.14}$$

where $\Theta(x)$ is the unit step function, as shown in Fig. 2.1(a).

In 2D, the number of available states in **k**-space is determined by the number of points contained in the radius k_F and thickness dk; the boundary between the occupied and unoccupied states is called the *Fermi circle*. If $k > k_F$ the states are unoccupied and those states $k < k_F$ are filled up to k_F, see Fig. 2.1(b). The DOS per unit volume in **k**-space is

$$\frac{dn}{dk} = g(k) = \frac{4\pi k}{(2\pi)^2} = \frac{k}{\pi}. \tag{2.15}$$

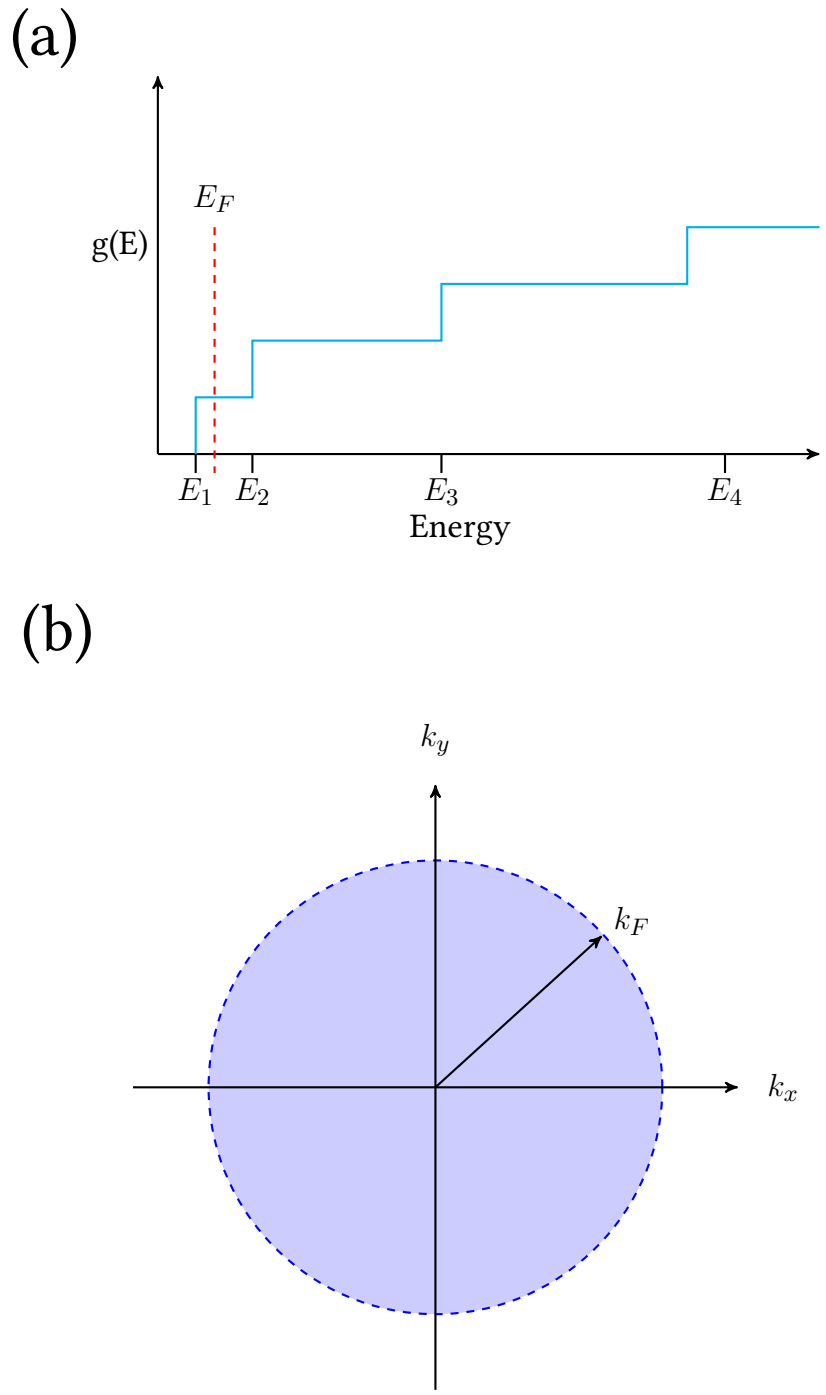

Figure 2.1: (a) Density of states for a 2DEG as a function of energy in a 2D system; E_1, E_2, E_3, E_4 are the energies for the four lowest energy levels and a step in DOS corresponds to populating the next higher subband. The DOS is given by, $g(E) = \sum_{i=1}^{3} \frac{m^\star}{\pi\hbar^2}\Theta(E - E_n)$. If the Fermi energy E_F is between $E_1 < E_F < E_2$, then only the lowest 2D subband is occupied. (b) States at $T = 0\,\mathrm{K}$ are filled up to the radius k_F and states $k > k_F$ are unoccupied.

2.2.3 Drude theory of transport

When $T = 0\,\mathrm{K}$, the electron states are filled up to E_F and all electrons acquire the same average drift velocity v_d when induced by an electric field E, causing the Fermi circle to shift in **k**-space in the direction of the field; in the presence of E, electrons accelerate in the direction of the field with v_d. This relationship between v_d and E is defined as,

$$v_d = \frac{Ee\tau}{m^\star} = \mu E, \tag{2.16}$$

where τ is the mean time between momentum relaxing collision events, the charge of a single electron is $e = 1.602 \times 10^{-19}\mathrm{C}$ and μ is mobility. This allows the mean free path l_m to be denoted as

$$l_m = \tau v_F, \tag{2.17}$$

where the Fermi velocity v_F is given by

$$v_F = \frac{\hbar k_F}{m^\star}. \tag{2.18}$$

If there is no magnetic field B present, the current density J is given by

$$J = nev_d = \frac{ne^2\tau E}{m^\star} = \sigma E, \tag{2.19}$$

where n is the electron density and σ is the Drude conductivity calculated as,

$$\sigma = \frac{ne^2\tau}{m^\star} = ne\mu. \tag{2.20}$$

μ is an important quantity in the classification of 2DEGs and it is the common way of specifying the quality of a 2DEG. The scattering rate and thus the mobility depends strongly on the disorder; the lower the disorder, the higher the mobility.

In this thesis, the 2D electron density n_{2D} is measured from the Hall resistance R_H through the relation,

$$n_{2D} = \frac{1}{R_H e}; \tag{2.21}$$

the electron density depends on the doping concentration and thickness of the AlGaAs spacer between the 2DEG and the doping plane and illumination and gate voltage, if the device has them.

Drude transport theory assumes that all electrons contribute to the current, since each electron acquires the same average v_d in the electric field. However, all states below the Fermi level are filled and the electric field changes the distribution of electrons at the Fermi level; only the states at the Fermi surface contribute to the conductivity. The response of the electrons near the Fermi level to an electric field is expressed in the Einstein relation,

$$\sigma = e^2 g(E_F) D, \tag{2.22}$$

where $g(E_F)$ is the density of occupied electron states and D is the diffusion constant, which is 2D is given by

$$D = \frac{v_F l_m}{2} = \frac{v_F \tau}{2}. \tag{2.23}$$

2.3 Ohmic contacts

Ohmic contacts are necessary to make electrical and thermal contact to the 2DEG. In this section, we begin with a discussion on AuGeNi Ohmic contacts before presenting the physics of the contact and resistivity models.

2.3.1 AuGeNi Ohmic contacts

Introduction

Au, Ni and Ge alloys are the routinely employed material of choice to make Ohmic contact to the electrons in GaAs-based devices, due to the excellent contact resistivity, reliability, and usefulness over a wide range of doping levels[9]; Sn contacts used by Gunn et al[10] evolved into AuGeNi contacts introduced by Braslau et al[11] in 1967.

In this thesis, two different Au, Ge and Ni alloy Ohmic contact processing methods are used for the samples; these methods are called eutectic or layered, in both cases rapid thermal annealing (RTA) is used. Eutectic fabrication is the deposition of a AuGeNi (83:12:5 atomic weight) eutectic 'slug' from a single evaporation boat; this technique has little control over the final deposited thickness of the contact. The layered technique requires the separate evaporation of Ni, a AuGe eutectic (88:12 atomic weight) and Au in a layered manner; this technique has more control of metal thickness and the order of evaporation. There are reports[12, 13] showing that the specific contact resistance of the layer by layer deposited Ohmic contact is more reproducible and the surface morphology is smoother than by the AuGeNi alloy evaporation; Ref.[14] also suggests the contact resistances depends on the orientation of the edges with respect to the crystal directions of the substrate.

The role of Au, AuGe and Ni in Ohmic contact formation

From the literature, there is a consensus on the roles of each metal, Table 2.1 summarises different recipes of AuGeNi Ohmic contacts found in the literature. The layer of Au on top reportedly improves surface morphology, reduces the sheet resistance and enhances the effect of making more uniform Ohmic contacts[15, 16]. Some reports on the formation mechanism claim that a contact is formed when AuNiGe originating from the metallisation penetrates the heterostructure in concentrated spikes[17, 18]; however, the literature generally supports the mechanism of homogeneous formations, where the metal diffuses consistently[19].

It is believed that annealing AuGeNi Ohmic contacts is a balance of Ge in-diffusion and Ga out-diffusion in the boundary layer of the substrate which forms a negatively doped layer, allowing electron tunnelling[20]; Ge is said to diffuse from the AuGe alloy, into the depth of the 2DEG to make contact[21]. In this mechanism, the metal on the surface segregates into Ni-rich and Au-rich phases, where the Ni phases contain most of the Ge; these phases penetrate the heterostructure and grow towards the 2DEG in large grains diffusing the Ge deeper[22]; excess As transports to the surface where it either resides or vaporises.

It is understood that Ni enhances the diffusivity of Ge in GaAs forming compounds and making good electrical contact to GaAs[23]; from around $300\,^{\circ}\mathrm{C}$ reports have identified grains such as, Ni_2Ge, Ni_3Ge, γ-NiAs, Ni_2As, NiAs, Ga_4Ni_3, $(GeNi)_{80}$ and $GeNi_2$ moving toward the wafer making contact to the GaAs[24–26]; the Ni_2GeAs grains reportedly grow with increasing temperature causing inhomogeneity at the interface[27–30]. Without Ni, AuGe contacts have poor contact resistance, morphology, and have large variations in contact resistance[31–34].

It is believed, when $T > 375\,^{\circ}\mathrm{C}$, Ga diffuses up through the Ni layer, reacting with Au forming phases such as α-AuGa[35–37], β-AuGa[38], Au_2Ga, Au_7Ga_2, A_3Ga[37], Au_4Ga[39] and Au(Ge, As)[40]. Voids formed by the loss of As are filled with different Ge compounds like AuGe and NiGe (between $407\,^{\circ}\mathrm{C} - 425\,^{\circ}\mathrm{C}$)[41]; the kinetically favoured AuGa reaction will continue until the supply of Au is exhausted.

In depth studies on phases and compounds of AuGeNi Ohmic contacts in Ref.[42] and references therein, report a final AuGa matrix a mixture of α-, α‘-, β-, β‘- AuGa phase islands with NiGe and NiGeAs clusters.

From the given description of annealing and the different recipes and conditions used shown in Table 2.1 some conclusions can put forward as bullet points.

1. There is no defined recipe or condition used in every group, each group has their own recipe and annealing conditions. However, there are similar results observed in each group regarding compound formation at certain temperatures.

2. Annealing is a balance of Ge in-diffusion and Ga out-diffusion[20], Ge diffuses from the AuGe alloy into the depth of the 2DEG to make contact[21] and excess As transports to the surface where it either resides or vaporises.

3. Ni enhances the diffusivity of Ge in GaAs forming compounds and making good electrical contact to GaAs[23].

4. From $300\,^{\circ}\mathrm{C}$ Ni_2Ge, Ni_3Ge, γ-NiAs, Ni_2As, NiAs, Ga_4Ni_3, $(GeNi)_{80}$ and $GeNi_2$ grains make contact to the GaAs[24–26] and Ni_2GeAs grains grow with increasing temperature [27–30].

5. When $T > 375\,^{\circ}\mathrm{C}$, Ga diffuses up through the Ni layer, reacting with Au forming α-AuGa[35–37], β-AuGa[38], Au_2Ga, Au_7Ga_2, A_3Ga[37], Au_4Ga[39] and Au(Ge, As) [40] phases.

6. Between $407\,^{\circ}\mathrm{C} - 425\,^{\circ}\mathrm{C}$ the voids formed by the loss of As are filled with different Ge compounds like AuGe and NiGe [41].

Table 2.1: Different recipes of AuGeNi Ohmic contacts on GaAs/AlGaAs from the literature.

Recipe	Anneal method	Anneal Temperature	Anneal time	Ref.
250 nm AuGe (12%wt Ge)/110 nm Ni	Furnace	240 °C→365 °C	5 mins	[27]
50 nm Ni/270 nm AuGe (12%wt Ge)/140 nm Ni	Furnace	240 °C→365 °C	5 mins	[27]
160 nm AuGe (107.2 nm/52.8 nm)/40 nm Ni	RTA	370 °C for 120 s then 440 °C for 50 s	170 s	[14]
100 nm AuGe (12%wt Ge)/30 nm Ni/300 nm Au	RTA	390 °C→450 °C	45 s	[21]
100 nm AuGe (12%wt Ge)/20 nm Ni/50 nm Au	Furnace	490 °C	90 s, 115 s, 200 s	[23]
240 nm AuGe (12%wt Ge)/30 nm Ni/120 nm Au	Furnace	430 °C	3 s→24 s	[24]
5 nm Ni/100 nm AuGe/100 nm Ni/200 nm Au	Furnace	350 °C→450 °C	30 s	[20]
5 nm Ni/17 nm Ge/30 nm Au/15 nm Ni/200 nm Au	Furnace	420 °C	30 s	[40]
0 nm-10 nm Ni/100 nm AuGe (27%wt Ge)/50 nm Au	Furnace	350 °C→600 °C	2 mins	[38]
5 nm Ni/45 nm Au/20 nm Ge	Carbon heater	450 °C	30 s	[41]
20 nm Ni/20 nm Ge/300 nm Au	Furnace	460 °C	8 mins→16 mins	[30]

The different recipes and processing methods of AuGeNi Ohmic contacts used in the literature. The elements are listed in order of evaporation and the "/" symbol indicates an evaporation layer, where this is not the case it is a eutectic, such as AuGe.

2.3.2 The physics of Ohmic contacts

Ohmic contacts of metals on semiconductors are Schottky junctions[43, 44] of a sufficiently narrow energy barrier so that extensive tunnelling across it causes the effective barrier height to become zero[45]. The requirement of the Ohmic contact is that it must allow electric currents to flow in and out of the device while the current-voltage $I - V$ relationship should be linear and remain Ohmic at low temperatures and high magnetic fields, see Fig. 2.2.

The dominant electron transport mechanism in the Ohmic contact is field emission. The current density J for field emission has the form,

$$J \approx \exp(-q\phi_b/E_{00}), \tag{2.24}$$

where E_{00} is a material dependent constant expressed as,

$$E_{00} = \frac{q\hbar}{2}\sqrt{\frac{N}{\epsilon_s m^\star}}, \tag{2.25}$$

where $\epsilon_s = \epsilon_r\epsilon_0$ is the semiconductor permittivity, N is the doping factor, m^* is the effective mass, ϕ_b is barrier height and q is the electron charge[46].

Other current transport mechanisms include thermionic emission, see Fig. 2.2(a), and thermionic-field emission, see Fig. 2.2(b). In thermionic emission, the depletion region is too thick due to low doping concentrations and minimal or no tunnelling takes place across the interface. Thermionic-field emission is a combination of thermionic and field emission where tunnelling takes place at energies between the top of the barrier and the Fermi level; in this mechanism, electrons have enough thermal energy to reach the upper narrower portion of the barrier where tunnelling may occur.

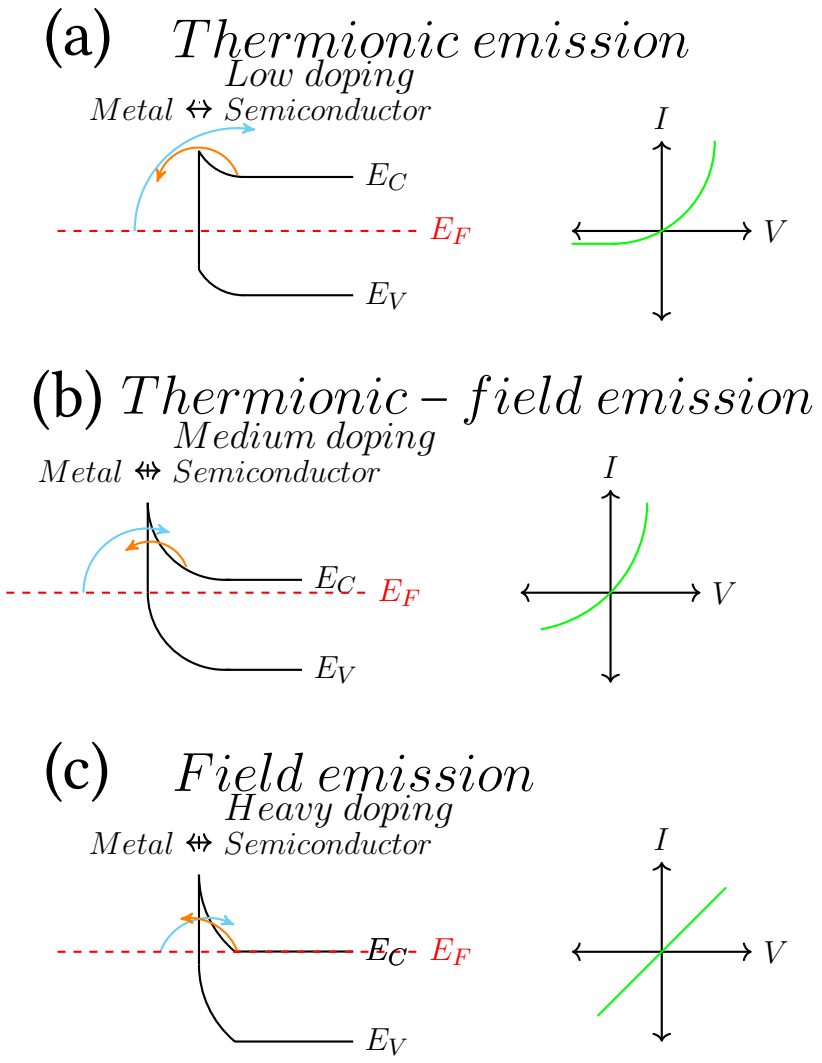

Figure 2.2: Band diagrams and $I - V$ plots showing three models for current transport mechanisms in metal-semiconductor junction. (a) An example of current transport in the thermionic emission regime where electrons may cross the potential barrier by having enough thermal energy to pass over. The depletion region is so wide that the only way for electrons to jump the potential barrier is by emission over its maximum. (b) Current transport in the thermionic-field emission regime. At moderately high doping, the barrier is slightly narrower then (a). Only electrons with sufficient thermal energy to tunnel near the top of the barrier produce a significant current. (c) Current transport in the field emission regime; the transport regime for Ohmic contacts. At very high doping, the barrier can be thin enough to permit field emission; as the width of the depletion layer decreases with increasing doping, quantum-mechanical tunnelling of electrons through the barrier occurs, this exhibits Ohmic behaviour.

Fabricating the Ohmic contact for field emission relies on the formation of the tunnelling metal-semiconductor junction by creating a thin heavily doped semiconductor layer at the interface between the two materials. To achieve this, the presence of a highly doped material, between the metal and semiconductor is necessary with the required value of doping for n-GaAs of the order $1{\times}10^{19}\text{cm}^{-3}$[47], in AuGeNi contacts Ge is the dopant. This highly doped semiconductor layer is formed during the contact preparation and heat treatment drives this dopant into the semiconductor[48]; by increasing the doping density, narrowing the potential barrier, at low T the Fermi energy lifts closer to the conduction band E_C and the depletion depth is decreased, resulting in a higher tunnel probability producing field emission, see Fig. 2.2(c).

When the metal and the semiconductor make contact, a Schottky barrier forms because of band bending in the valence band E_V and conduction band E_C due to electronic states at the semiconductor and metal interface; E_C and E_V in the semiconductor bend to make the Fermi level E_F align with the metal.

For Ohmic contacts, this barrier must be low enough for electrons to cross by field emission and introducing impurities on the semiconductor surface reduces barrier height ϕ_b and presents surface states for Fermi level pinning[49]; surface states set the barrier height for current to flow and occur in the gap between E_C and E_V and is a function of the semiconductor and independent of the metal[50].

Figure 2.3 shows the energy band diagrams of the metal-semiconductor junction. As the barrier height,

$$\Phi_b = \Phi_m - \chi_s, \tag{2.26}$$

is due to the difference between the work function of the metal Φ_m and the semiconductor electron affinity χ_s, carriers travelling from the metal to the semiconductor need to have an energy greater than Φ_b to pass over it; but carriers travelling from the semiconductor to the metal need to have an energy greater than V_{bi}, where V_{bi} is the built-in potential given as,

$$V_{bi} = \Phi_m - \Phi_s. \tag{2.27}$$

In these possible transport mechanisms, a potential difference must exist across the barrier to cause current to flow; this is the fundamental origin of contact resistance.

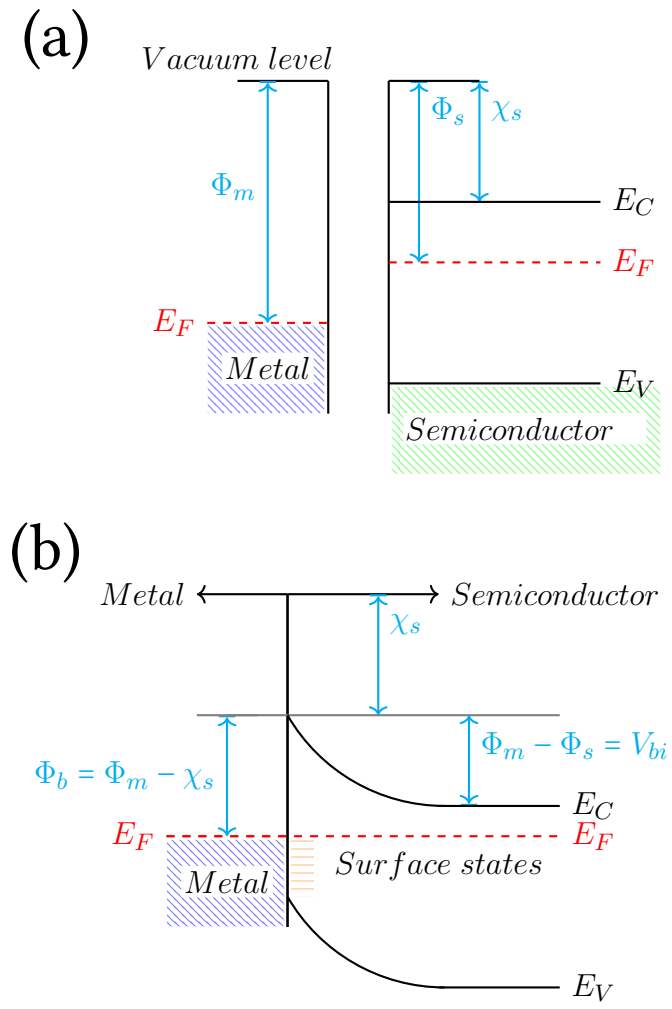

Figure 2.3: Energy band diagrams of the metal-semiconductor junction. (a) Before the two materials make contact, there is a difference between the E_F of the metal and semiconductor. (b) After contact, a Schottky barrier forms and charge transfer bends E_C and E_V in the semiconductor to make E_F align with the metal. The barrier height Φ_b, is due to the difference between the work function of the metal Φ_m and the semiconductor electron affinity χ_s given as, $\Phi_b = \Phi_m - \chi_s$. Surface states, a function of the semiconductor and independent of the metal, set the barrier height V_{bi} for current to flow and occur in the gap between the E_C and the E_V bands.

Contact resistivity

In this section, we review the transfer length method (TLM)[51] where the total resistance R_T between any two contacts of length L_C and width W separated by a distance L could be measured and plotted as a function of L.

The common method for quantitatively evaluating the performance of Ohmic contacts to semiconductors is to measure the value of the specific contact resistance $\rho_C(\Omega$ cm^2) and the TLM provides a method to achieve this; for the purposes of measurement, the contact resistance R_C is the common parameter. The R_C of a 2DEG is the resistance between top of the Ohmic contact and the edge of 2DEG and the primary resistance determining the cooling of the sample through the leads, it arises during the annealing process. Figure 2.4(a) shows a TLM test structure with a pattern of unequal spacing of length L_n between the contacts, where $n = 1, 2, 3, 4$. To determine the contact parameters with the TLM, resistance measurements are made between the adjacent contacts and the total resistance R_T between any two contacts is given by

$$R_T = 2R_C + \frac{R_\square L}{W}, \tag{2.28}$$

where W is the width of the semiconductor channel and $R_\square$ is the sheet resistance of the 2DEG per square. By plotting the measured resistances as a function of the contact spacing, the transfer length L_T, the $R_\square$ and the contact resistance R_C is deduced from the x-intercept and the y-intercept, see Fig. 2.4(b) where the slope = $\frac{R_\square}{W}$ and intercepts R_T at $2R_C$ and the x-axis at $-2L_T$.

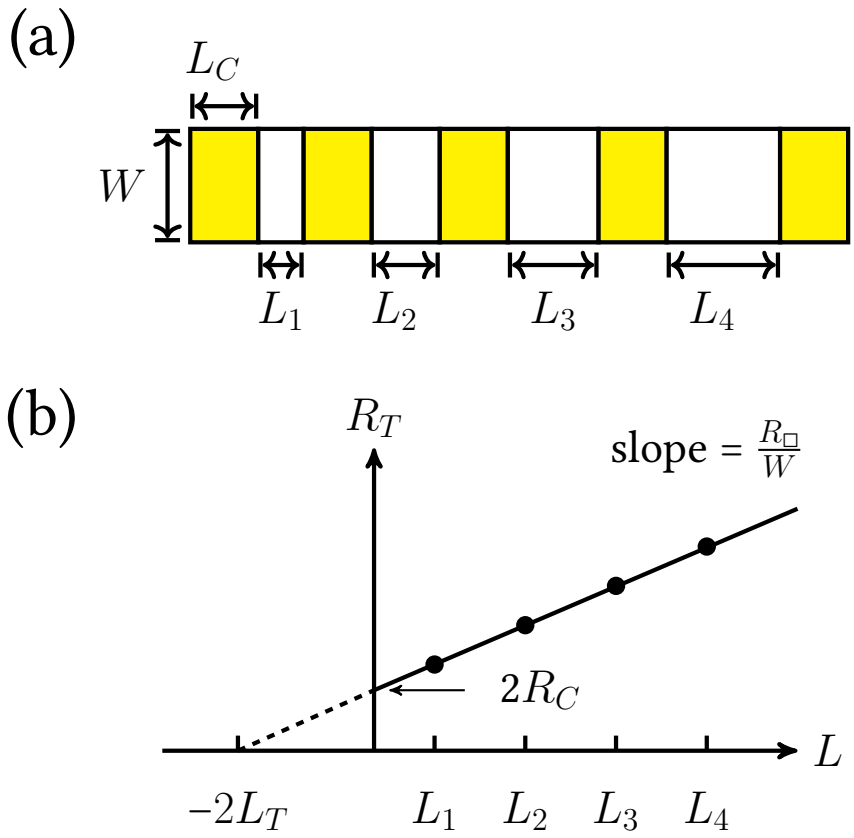

Figure 2.4: (a) Schematic of a TLM device. The mask shows the length of the semiconductor spacing (white) labelled as L_n, where $n = 1, 2, 3, 4$ increases between the metal contacts (yellow) which remain the same length L_C; the width W of the device remains the same. (b) Plotting the total resistance between the contacts as a function of spacing. The intercept is twice the contact resistance R_C and the slope represents the bulk resistivity. The parameter extracted from the x-intercept is the transfer length $-2L_T$, the effective length needed for the current to transfer from the metal to semiconductor, and the parameter extracted from the y-intercept is the contact resistance $2R_C$.

Figure 2.5 shows the current crowding model[52, 53], where the current does not flow uniformly out of the whole length contact length L_C but only from the transfer L_T, see Fig. 2.5(a); L_T accounts for the current crowding at the edge and across the length of the contact and is an indication of the resistance due to the contact's finite size. Figure 2.5(b) shows that current flowing into or out of a contact can crowd into a portion of the contact. In this model, the current I flow goes as

$$I(x) = I_o e^{-(x/L_T)} \tag{2.29}$$

where I is the current and x is the distance through the contact.

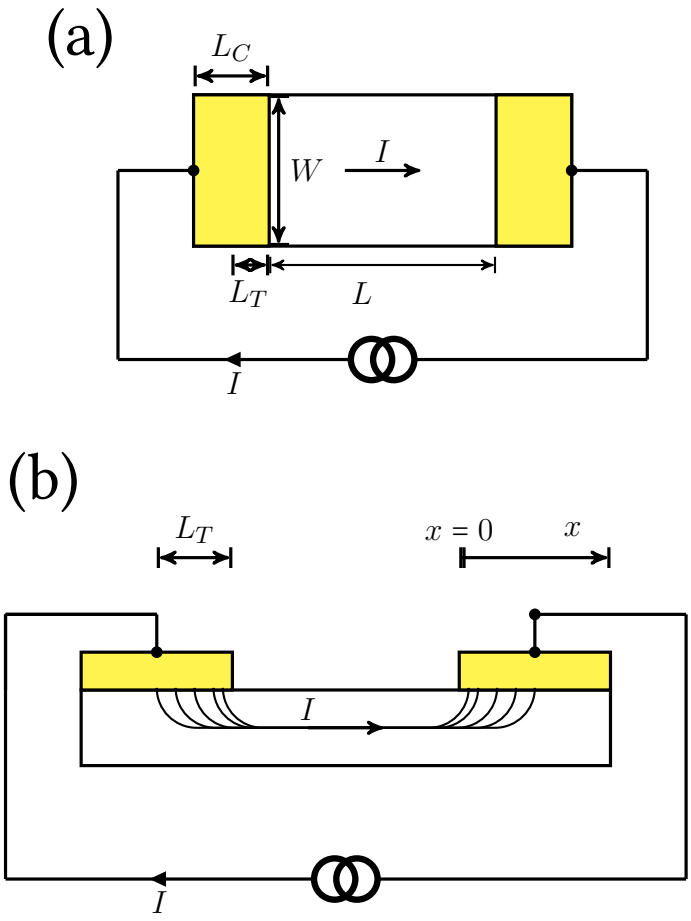

Figure 2.5: Illustration of current crowding and the transfer length L_T. a) Applying a voltage across the metal contacts results in the current not taking the entire cross section to enter the semiconductor from the metal, but instead it takes a very small fraction to enter the semiconductor from the metal – this is the transfer length L_T. b) The current flow encountered beneath the planar contact. The current flow decreases exponentially in the semiconductor layer from the edge in the form $I(x) = I_o e^{-(x/L_T)}$ where I is the current and x is the distance. The Ohmic contacts in this thesis have a $L_T \ll L_C$.

In the TLM model, $R_{\square}$ and the resistance R_{sk} of the 2DEG underneath the contact are the same. However, in an interpretation of the TLM data Ref.[54] shows the 2DEG under the contact is damaged brought about by the alloying process occurring at the metal-semiconductor interface, resulting in $R_{\square} \neq R_{sk}$. Due to annealing, R_{sk} cannot be accurately defined because the boundary between the contact and access regions is difficult to determine; this is a product of the diffusion between the metal and semiconductor, so the current flow into this region is not homogeneous. This model became more sophisticated by Reeves[55], who showed that L_T and the specific contact resistance $\rho_C(\Omega cm^2)$ can be obtained; in this model, R_C is shown to be

$$R_C = \coth\left(\frac{L_C}{L_T}\right) \times \frac{R_{sk}L_T}{W}, \tag{2.30}$$

where

$$L_T = \sqrt{\frac{\rho_C}{R_{sk}}}; \tag{2.31}$$

where ρ_C is the specific contact resistance (Ωcm^2) and rearranging Eq. 2.31, R_{sk} is calculated to be,

$$R_{sk} = \frac{\rho_C}{{L_T}^2}. \tag{2.32}$$

Therefore for $L_C \gtrsim 2L_T$,

$$R_T = \frac{2R_{sk}L_T}{W} + \frac{R_{\square}L_n}{W}. \tag{2.33}$$

Reeves[55] shows that if R_{sk} is modified, the correct value of ρ_C and L_T is found by measuring the vertical resistance R_V, this is the resistance between the top of the Ohmic contact and the semiconductor directly underneath this is defined as,

$$R_V = \sqrt{\frac{R_{sk}\rho_C}{W}} \times \frac{1}{\sinh\left(\frac{L_C}{L_T}\right)} = \frac{\rho_C}{L_T W} \times \frac{1}{\sinh\left(\frac{L_C}{L_T}\right)}. \tag{2.34}$$

on eliminating R_{sk} using Eq. 2.31. From Eq. 2.30, 2.31, 2.34, since

$$\frac{R_C}{R_V} = \cosh\left(\frac{L_C}{L_T}\right). \tag{2.35}$$

then L_T may be found and ρ_C can be determined from Eq. 2.34 .

2.4 Superconductivity

2.4.1 Basic phenomena

Here the basic ideas of superconductivity are covered.

A superconductor is an element, intermetallic alloy or a compound that exhibits two related phenomena, perfect electrical conductivity and the Meissner effect, in which below the critical temperature T_c and critical magnetic field B_c, the superconductor completely expels all magnetic fields B from the interior. The Meissner effect distinguishes a superconductor from a perfect conductor because a perfect conductor, such as a pure metal at $T = 0\,\mathrm{K}$, can have zero resistance, but cannot to expel magnetism. Figure 2.6 illustrates the perfect electrical conductor in a sketch showing electrical resistance R as a function of temperature $R(T)$.

Superconductivity occurs when normal electrons inside the material form Cooper pairs below T_c, resulting in a condensate with a lower energy than the normal electrons. Cooper pairs have spatial extent of the order of the coherence length ξ, the length inside which any change to the electron wavefunction at one point will propagate to the other electrons. At $T = 0\,\mathrm{K}$ all the Cooper pairs are in the ground state, separated from the allowed excited states by an energy gap $\Delta(T)$. From BCS theory the energy gap at $T = 0\,\mathrm{K}$ relates to T_c (independent of material) by

$$2\Delta(T = 0) = 3.5 k_B T_c, \tag{2.36}$$

where k_B is the Boltzmann constant[56].

Only the electrons within an energy range $k_B T_c$ of the superconducting ground state take part in the superconductivity. For $T > 0\,\mathrm{K}$ some of the Cooper pairs break-up and quasiparticles are generated; quasiparticles include both electron-like and hole-like excitations. With increasing T the quasiparticles are excited across the gap and there are fewer Cooper pairs in the superconducting ground state so that $\Delta(T) \to 0\,\mathrm{K}$ at $T = T_c$ and the number of Cooper pairs reduces to zero.

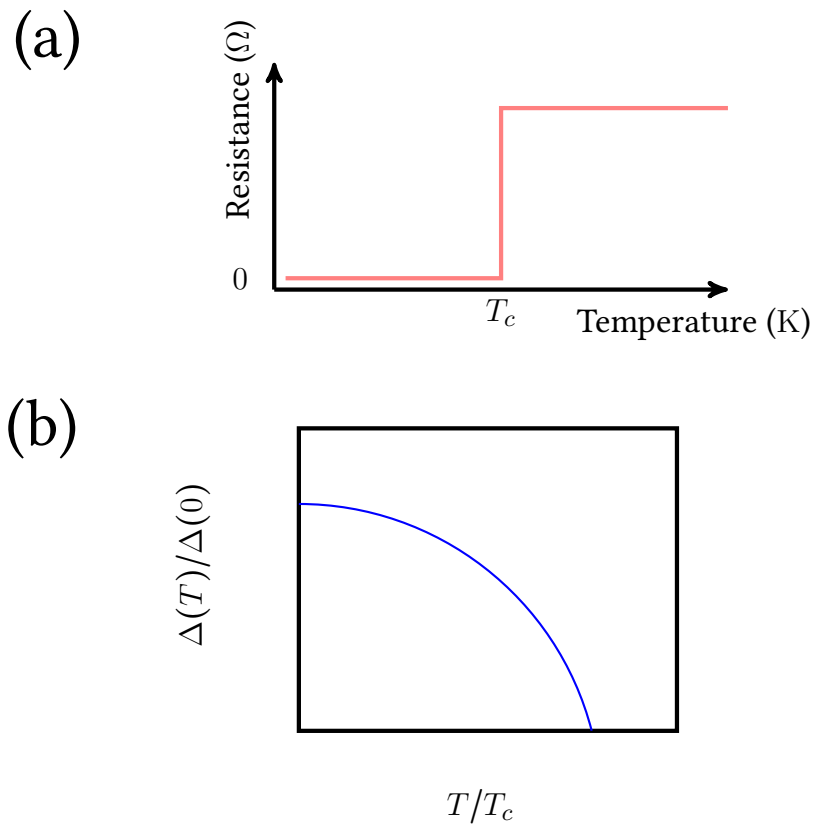

Figure 2.6: (a) A schematic showing of the typical transition from normal to superconducting behaviour in the resistance $R(T)$ of a superconductor, below the critical temperature T_c a temperature unique to the specific material, the superconductor loses its electrical resistance. In all superconductors, the current I is carried by Cooper pairs. When the temperature is less than the critical temperature, $T < T_c$, the binding energy of the Cooper pairs is large compared to the thermal energy, resulting in Cooper pairs propagating through the material and therefore, current flowing without any resistance. (b) BCS theory predicts that the normalised excitation gap $\Delta(T)/\Delta(0)$ as function of reduced temperature T/T_c follows a universal curve, the ratio $2\Delta = 3.52 k_B T_c$ is universal.

In the Meissner effect the externally applied magnetic field B is screened from the bulk of the superconductor by screening currents flowing on the surface of the superconductor. The screening currents allow B to penetrate the superconductor up to a length inside the superconductor, called the penetration depth λ_L; screening currents can only screen B up to a certain B_c and when $B > B_c$ superconductivity is destroyed and the superconductor will return to its normal state. Figure 2.7 shows the Meissner effect, where B is completely expelled from the material for $T < T_c$, superconductors below T_c to exclude B as long it does not exceed their unique critical magnetic field B_c.

A DC current I_{DC} flowing in the superconductor can also destroy the superconductivity. The critical current density J_c is the maximum current that a superconductor can support; above J_c the current breaks the Cooper pairs destroying the superconducting state.

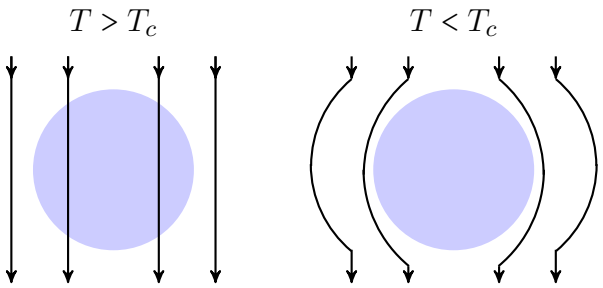

Figure 2.7: Schematic showing the Meissner effect. When the temperature $T < T_c$, the magnetic field B is completely expelled from the material, but when $T > T_c$, B penetrates the material.

In the presence of B the free energy of the normal state is lower and the superconductivity is quenched, this happens at the critical magnetic field B_c. This puts a limit on the current, called the critical current I_c, which may be carried by a superconductor due to B induced by the current itself. The relationship between B_c at any T below T_c is given by,

$$B_c \approx B_c(0)\left[1 - \left(\frac{T}{T_c}\right)^2\right]. \tag{2.37}$$

In both Type I and Type II superconductors B is completely excluded from the interior and is superconducting when B is less then the critical magnetic field B_c or B_{c1}; however, above B_c or B_{c2}, the material is no longer superconducting.

Figure 2.8(a) shows that in Type I superconductors, B is expelled completely from the interior for fields below B_c, this is the Meissner effect, but applying B in excess of B_c quenches superconductivity and returns the material to its normal state. In Type II superconductors, see Fig. 2.8(b), it is thermodynamically favourable for the superconductor to exist in a mixed normal and superconducting state. Fields in excess of B_{c1} penetrates the superconductor in the form of vortices where B is confined; in real materials, vortex cores exist in non-superconducting regions like defects or grain boundaries[56, 57].

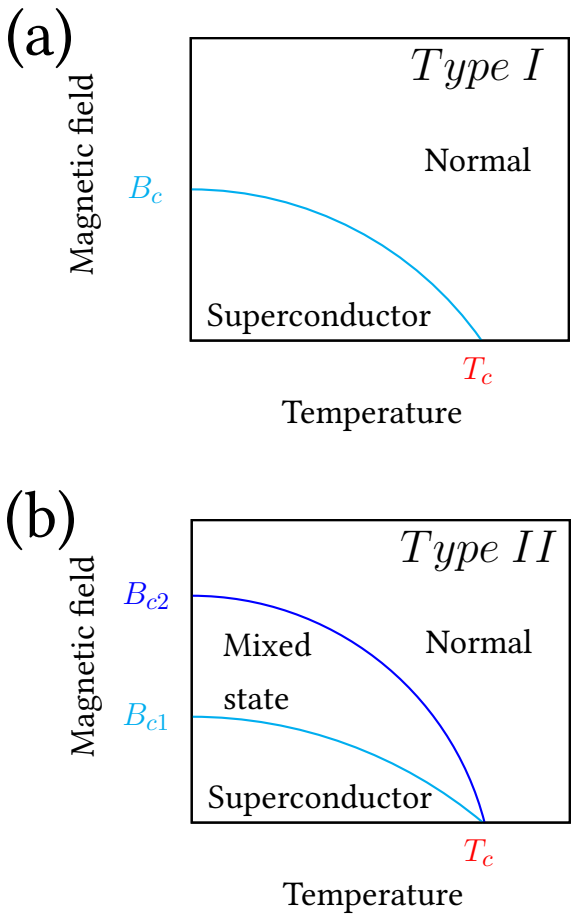

Figure 2.8: Phase diagrams for Type I and Type II superconductors. (a) In the superconducting state, Type I superconductors completely expel B from the interior when $B < B_c$, this is the Meissner effect. When $B > B_c$, the external applied magnetic field quenches superconductivity and returns the material to its normal state; Type I superconductors have only one critical magnetic field B_c. (b) Type II superconductors exhibit a mixed state ordinary and superconducting properties at intermediate temperature and fields above B_{c1}, but below B_{c2}. The superconducting phases in this mixed state features the formation of magnetic field vortices. The vortex density increases with increasing field strength and when $B > B_{c2}$, superconductivity is destroyed returning the material to its normal state.

Chapter 3

Two-Dimensional Electron Gases

3.1 Introduction

This chapter describes the two-dimensional electron gas in practice, this includes discussion on the GaAs/AlGaAs heterostructure, sample fabrication methods and Ohmic contact processing techniques. The wafer characteristics and the Ohmic contact processing conditions for the samples are covered in this chapter. Also presented in this chapter are microstructure and morphology investigations of Ohmic contacts.

3.2 GaAs/AlGaAs heterojunctions

The advantage semiconductor structures have over metallic films is the charge carriers can have a higher mobility and secondly, by doping or by applying an electric field, the carrier concentration can be varied. The carrier density is much lower than in metals with a Fermi wavelength comparable to structures fabricated by lithographic methods, making possible the study of diffusive, quasi-ballistic and ballistic transports regimes, examples include the integer and quantum Hall Effect[58, 59] and one-dimensional conduction[60].

Electronic transport in a system is described as two-dimensional, when potential barriers constrain the electrons in one direction. To quantise the motion of a particle in one direction, the confining potential must have a width comparable to the de Broglie wavelength $\lambda = h/p$ of the particle, in a semiconductor this is $10\,\mathrm{nm}$. If the kinetic energy of the electron is smaller than the confining potential energy, the momentum and energy associated with the motion in the confined direction is quantised and the electron will lose one or more degrees of freedom; depending on the number of confinement directions, the system will be two, one or zero-dimensional. Modern lithographic and molecular beam epitaxy (MBE) techniques produce systems that behave as planes, wires and dots; the heterostructures in this thesis are grown by MBE.

The electric transport of conducting materials like metals or semiconductors are understood using the Drude model of the free electron gas. The transport properties at low temperatures are determined by the electrons close to the Fermi level E_F. Therefore, the electron gas will be considered two-dimensional if one of the dimensions are comparable to the Fermi wavelength λ_F, the de Broglie wavelength of the electrons at E_F; λ_F, the length scale which determines whether an electron is confined or not is given by,

$$\lambda_F = \sqrt{\frac{2\pi}{n_{2D}}}, \tag{3.1}$$

where n_{2D} is the carrier concentration.

3.2.1 MBE growth

Molecular-beam epitaxy (MBE) allows semiconductor crystals such as GaAs/AlGaAs, to be grown layer-by-layer with atomic precision[61], with the opportunity to engineer the band structure, Fig. 3.1 shows a schematic of a MBE chamber. The starting point for growth is a very clean, high purity crystal of GaAs mounted on a rotating heated substrate holder, connected to a Continual Azimuthal Rotation (CAR) in an ultra-high vacuum chamber. The wafer is grown a monolayer at a time in an ultra-high vacuum (10^{-8}–10^{-12} Torr) and the Al, Si (*n*-type dopant), Ga and As are individually heated in separate sources called effusion or Knudsen cells; the molecular beams of each element are controlled by shutters. The growth rate and surface cleanliness before and during epitaxy is observed using reflection high-energy electron diffraction (RHEED).

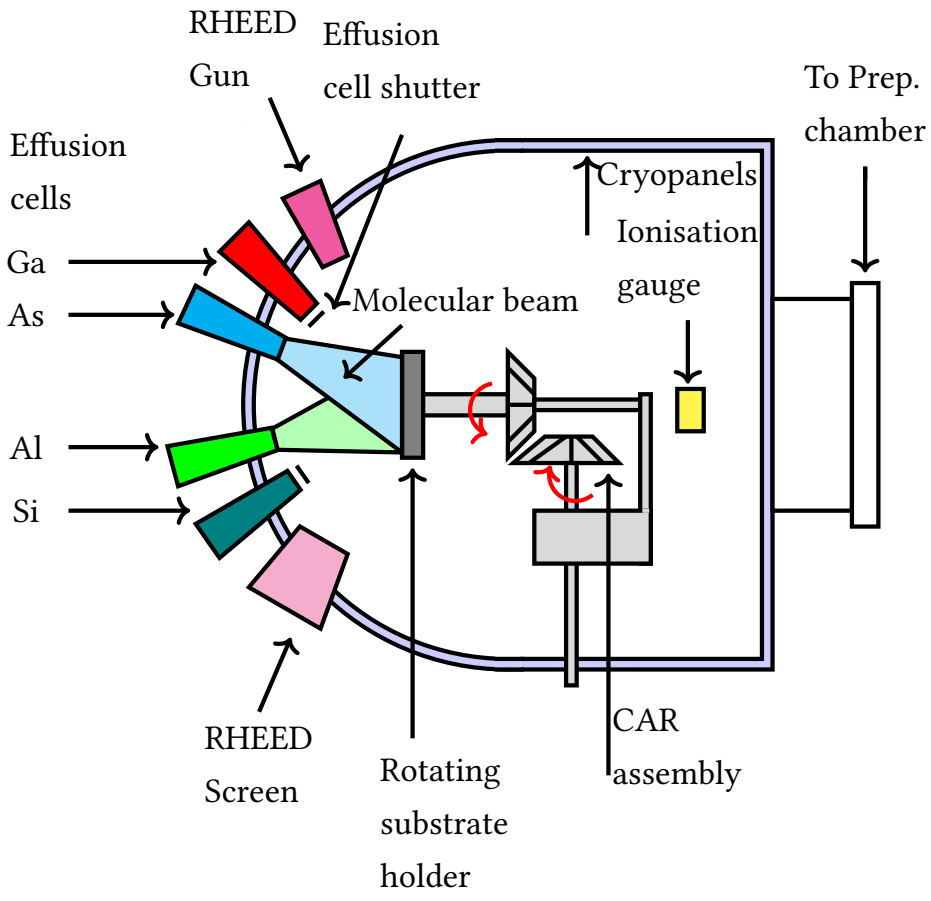

Figure 3.1: A schematic of a MBE chamber used to grow the GaAs/AlGaAs heterostructures. There are four different effusion cells Ga, As, Al and Si that evaporated from solid sources in heated cells known as Knudsen or effusion cells; the atoms of the material effuses toward the heated substrate in collimated beams. Within these beams, the particles neither react nor collide with one another and the rotation of the heated substrate allows uniform deposition. The deposition onto the substrate is ballistic and the particles undergo molecular flow, thus the name molecular-beam epitaxy.

3.2.2 Modulation-doped heterostructures

High quality mobility AlGaAs/GaAs heterostructure have close matched lattice constants to reduce strain and dislocations and by nature, is the ideal crystal to produce high mobility 2D samples. In GaAs, it is possible to control the band gap E_g through band gap engineering. If a fraction x of the Ga atoms in GaAs is replaced by Al atoms, then the alloy $Al_xGa_{1-x}As$ is produced. If the substitution is achieved randomly, then the band gap of the resulting alloy $E_g(Al_xGa_{1-x}As)$ is given by,

$$E_g(\mathrm{Al}_x\mathrm{Ga}_{1-x}\mathrm{As}) = (1.424 + 1.247x)\mathrm{eV}; \tag{3.2}$$

in this thesis $x = 0.33$. The matched lattice parameter between GaAs and $Al_{0.33}Ga_{0.67}As$ means that one can be grown on top of the other and at the heterojunction, there will be little strain. Therefore, very few dislocations will be formed at the junction, which will be atomically sharp; the lack of strain and dislocations means there will be few scattering centres in the 2DEG.

Due the growth of GaAs and $Al_xGa_{1-x}As$, the conduction band E_C and the valence band E_V are shifted in the $Al_xGa_{1-x}As$ relative to the GaAs, so that a quantum well is formed for both electrons and holes in the GaAs layers, see Fig. 3.2. The free carriers are now confined along the *z*-axis and form standing waves in the potential well, but they are still free to move in the *xy*-plane.

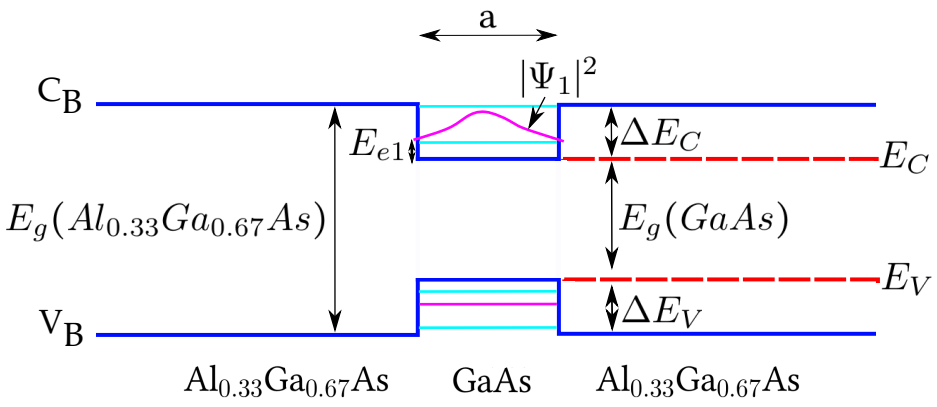

Figure 3.2: A quantum well made up of a layer of GaAs width a, sandwiched between two layers of $Al_{0.33}Ga_{0.67}As$; the electronic structure shows $E_g(GaAs) = 1.42\,\mathrm{eV}$ is the gap of bulk GaAs and the lowest confined level of E_C is E_{e1}.

Figure 3.3 shows a finite depth GaAs quantum well surrounded by AlGaAs, with the E_C profile shown. Due to $E_g(GaAs) < E_g(AlGaAs)$, the well in E_C occurs in the region composed of GaAs. If the system is doped with electrons only one state in the quantum well is occupied, labelled as E_1; if growth and electron confinement occurs in the z-direction, then the electron is free in the xy-plane creating a 2DEG.

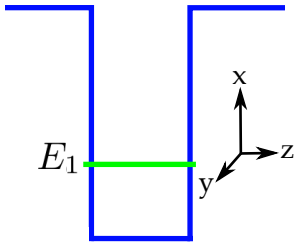

Figure 3.3: Finite depth GaAs quantum well surrounded by AlGaAs. The square well potential provides confinement in the z-direction, but the electron is still free to move in the xy-plane. The electron wavefunction and energy in the 2DEG are given by $\Psi = Ae^{ik_x x}e^{ik_y y}u(z)$ and $E = \hbar^2(k_x^2 + k_y^2)/2m + E_1$.

However, a simpler structure is the single heterostructure, see Fig. 3.4, where band bending gives rise to a triangular confinement well. To increase the purity of the heterojunction, it is modulation doped[62]; the *n*-type dopant, Si in this thesis, is introduced into the wide band gap AlGaAs at some distance from the 2DEG formed at the heterojunction interface. Therefore, the positive ionised Si atoms, upon donating their electrons will be situated further from the 2DEG leaving the narrow band gap GaAs free from intentional doping.

Figure 3.4 shows the conduction bands line-up when the two layers are first brought in contact and that E_F is constant throughout the sample. The bottom of E_C in the AlGaAs region is much higher than E_F and the electrons only populate the narrow gap GaAs. At temperatures $T > 100\,\mathrm{K}$, the thermally activated electrons spill over from the *n*-AlGaAs across the electrostatic barrier, leaving the positively charged donors. This space charge causes band bending, which prevents electrons returning to their donors.

The electrons transferred into the lower lying E_C of GaAs are confined in a triangular potential well, producing a 2DEG, see Fig. 3.4; the triangular potential well has a $10\,\mathrm{nm}$ width, which is comparable to the Fermi wavelength of the electrons. Trapped electrons donated by Si dopants in the AlGaAs populate the well and with motion quantised in the growth direction of the crystal, the electrons are free to move in the plane parallel to the interface. If a large increase in the density of free electrons in the AlGaAs region occurs, the minimum in E_C within the doped AlGaAs layer falls below E_F creating a second population of electrons to appear in the doped AlGaAs region causing parallel conduction.

Whilst Si-doped AlGaAs provides excess electrons, not all the donor atoms are ionised releasing their electrons to the DX centres; the energy of the DX centres lies within E_C for AlGaAs, typically mid-gap[63]. At temperatures $T < 150\,\mathrm{K}$, the DX centres freeze out and there is not enough thermal energy to excite the electrons out of the DX centres. However, the band gap energy for this system $E_{g,Al_{0.33}Ga_{0.67}As} \approx 1.834eV$ corresponds to a wavelength of $\approx 676\,\mathrm{nm}$[64], the wave length of red light, and by illuminating the sample with a red light-emitting diode (LED), the electrons in the DX centres are excited enough to allow them to reach the heterojunction thus, increasing the carrier density of the 2DEG[65]; this is known as persistent photoconductivity or 'flashing' and is used as a means of changing the carrier density of the 2DEG in this thesis. If the sample remains at low T, there is not enough energy for the electrons to overcome the jump in E_C and return to the AlGaAs layer, allowing the 2DEG to maintain its higher density. However, if the sample is thermally cycled, it will return to its original state.

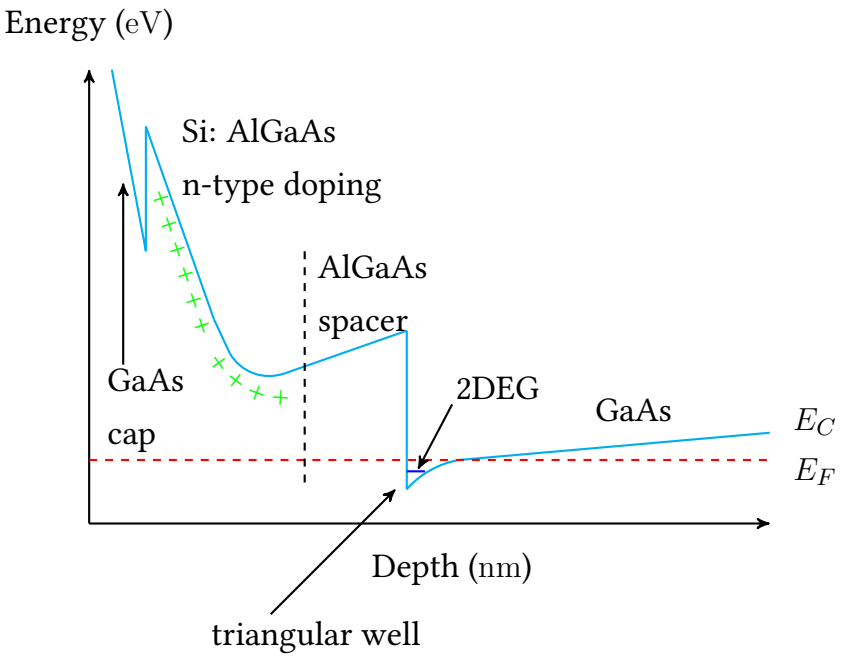

Figure 3.4: Conduction band E_C profile of a modulation-doped AlGaAs/GaAs heterostructure. The GaAs/AlGaAs heterostructure is fabricated by growing the ternary compound $Al_xGa_{1-x}As$ ($x \approx 0.33$) on a GaAs substrate. The crystal has few lattice defects because the mismatch in lattice spacing between the two materials is very small. At the interface between the two materials, the edge of the E_C (blue) is bent to form a potential well and electrons donated by Si dopants (green +) in the AlGaAs are trapped in the potential well at the interface. The ionised dopants are spatially separated from the 2DEG by a spacer layer reducing the scattering of the electrons by the ionised dopants.

3.2.3 Wafer details

Figure 3.5 shows the MBE grown structure of wafers W476, V827 and V834. In this structure, the 2DEG is created $90\,\mathrm{nm}$ below the sample surface at the $Al_{0.33}Ga_{0.67}As$/GaAs interface; on top of the undoped GaAs there is $80\,\mathrm{nm}$ of $Al_{0.33}Ga_{0.67}As$, capped with a $10\,\mathrm{nm}$ GaAs top layer; there is Si-doping in the upper $40\,\mathrm{nm}$ of AlGaAs, giving a spacer layer distance of $40\,\mathrm{nm}$ between the dopants and the 2DEG.

Table 3.1 summarises the carrier density n_{2D} and the mobility μ for each wafer.

Table 3.1: Assessment laboratory carrier density n_{2D} and the mobility μ characteristics of wafers used in this thesis.

Wafer	$\mu(\mathrm{x10^6 cm^2/Vs})$ dark	$\mathrm{n_{2D}(x10^{11} cm^{-2})}$ dark	$\mu(\mathrm{x10^6 cm^2/Vs})$ light	$\mathrm{n_{2D}(x10^{11} cm^{-2})}$ light
W476	3.0	1.9	5.2	3.5
V834	1.34	1.67	3.44	3.57
V827	1.19	1.58	3.17	3.41
W939	2.22	5.8	3.64	9.7

Assessment laboratory characteristics of the wafers in this thesis, data taken at $1.5\,\mathrm{K}$. The wafers were grown in two different molecular beam epitaxy machines (V and W) by Ian Farrer (W476, W939) and Harvey Beere (V827 and V834).

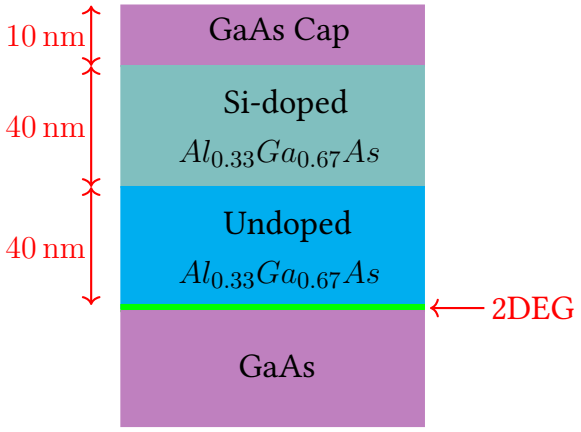

Figure 3.5: Schematic diagram of the MBE grown structure of wafers W476, V834 and V827, which are modulation-doped AlGaAs/GaAs heterostructures with the 2DEG created $90\,\mathrm{nm}$ below the surface.

3.3 Fabrication

After removal of the wafer from the MBE vacuum system, a series of processing stages is required to produce a device suitable for measurement. The process of device fabrication begins by blowing with dry nitrogen to remove any GaAs dust and then rinsing in acetone, propanol and deionised water. In this thesis, the minimum size of an Ohmic contact is $60\,\mu\mathrm{m} \times 80\,\mu\mathrm{m}$ and the maximum is $4\,\mathrm{mm} \times 1\,\mathrm{mm}$, for this ultra-violet (UV) optical lithography is required.

3.3.1 Photolithography of mesa structures

Figure 3.6 shows the process of optical lithography, processing begins by cleaving the wafer into chips and then coating with negative photoresist and baked, see Fig. 3.6(a). Patterning follows in Fig. 3.6(b) by placing the chip in a mask aligner and exposing it to an ultra-violet (UV) source through a photomask. Next, as shown in Fig. 3.6(c), the chemical development removes exposed areas on the chip followed by rinsing afterwards. Wet etching removes areas between the various mesas on the chip to provide isolation and define the conducting channel, see Fig. 3.6(d); it is necessary to etch beyond the Si-doped AlGaAs layer to isolate the 2DEG in the mesa.

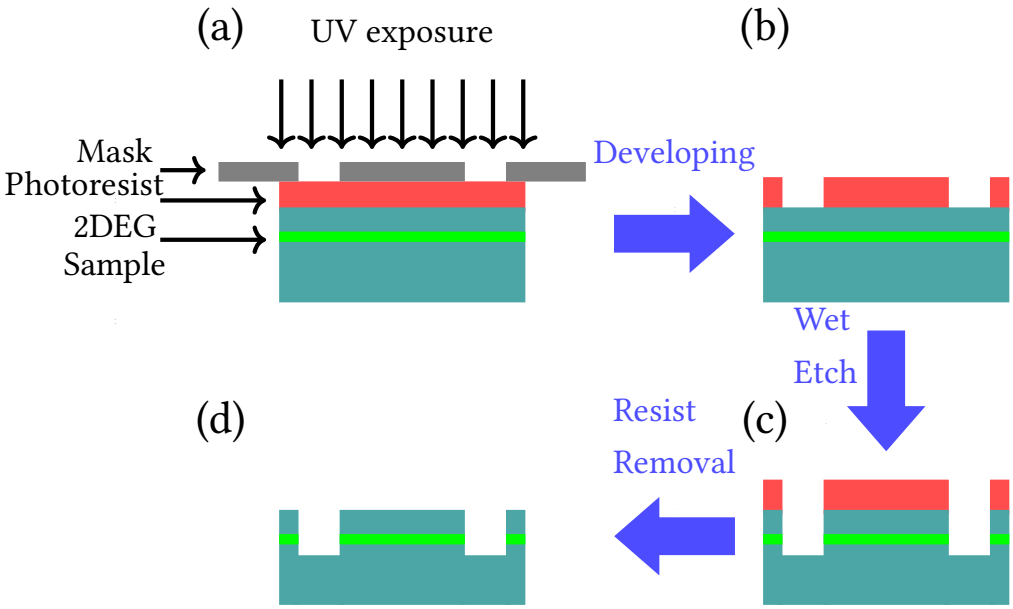

Figure 3.6: (a) Fabricating the mesa begins by depositing a photoresist layer on the chip surface and exposing it to a UV source through a mask; the mask contains the pattern of the mesa structure which is projected to the sample by exposure to UV light. (b) Development removes the exposed photoresist and (c) wet etching etches the regions not protected by the photoresist; transferring the required pattern onto the chip after etching, (d) leaving a raised area referred to as the mesa.

3.4 Technical details

In this thesis, ten samples are measured. These high electron mobility transistor (HEMT) structures are made from one of four wafers: W476, V827, V834 and W939; the substrate growth temperature was $625\,^{\circ}\mathrm{C}$-$630\,^{\circ}\mathrm{C}$, as measured by band-edge thermometry. The wafers were grown in two different molecular beam epitaxy machines by Ian Farrer (W476, W939) and Harvey Beere (V827 and V834) at the University of Cambridge; the V-chamber is a Veeco ModGENII and the W-chamber is a Veeco GENIII. Table 3.1 gives the carrier density n_{2D} and mobility μ is given for each wafer and Fig. 3.5 (W476, V827 and V834) shows the growth layer structures. Table 3.2 summarises the Ohmic contact processing conditions, processing is by Graham Creeth, Patrick See and Pedro Vianez using layered or eutectic metal deposition techniques.

3.4.1 Ohmic contacts

As shown in Fig. 3.7(a), after the mesa etch, Ohmic contact fabrication begins by coating the chip first in positive photoresist and then exposing it to UV light through a photomask. The chip is then soaked in chlorobenzene, which hardens the surface of the resist and develops slowly producing an undercut profile, see Fig. 3.7(b); it is important to create a break in the evaporated metal layer deposited on the surface because it would be impossible to remove the underlying resist and therefore, the unwanted metal from the structure. Following this in Fig. 3.7(c), evaporation commences and a quartz crystal monitor measures the approximate deposition thickness of the evaporated metal onto the chip; the metal is either evaporated as a AuGeNi (83:12:5 atomic weight) eutectic or in layers of Ni, a AuGe eutectic (88:12 atomic weight) and Au. Removing the photoresist and the metal on top after evaporation leaves only the metal deposited into the developed regions, as shown in Fig. 3.7(d). Finally in Fig. 3.7(e), all the contact metal lies on the surface of the chip and annealing diffuses the material down into the crystal to achieve the Ohmic contact to the conducting layer. This takes place in a rapid thermal annealer (RTA) at $430\,^{\circ}\mathrm{C}$ for $80\,\mathrm{s}$.

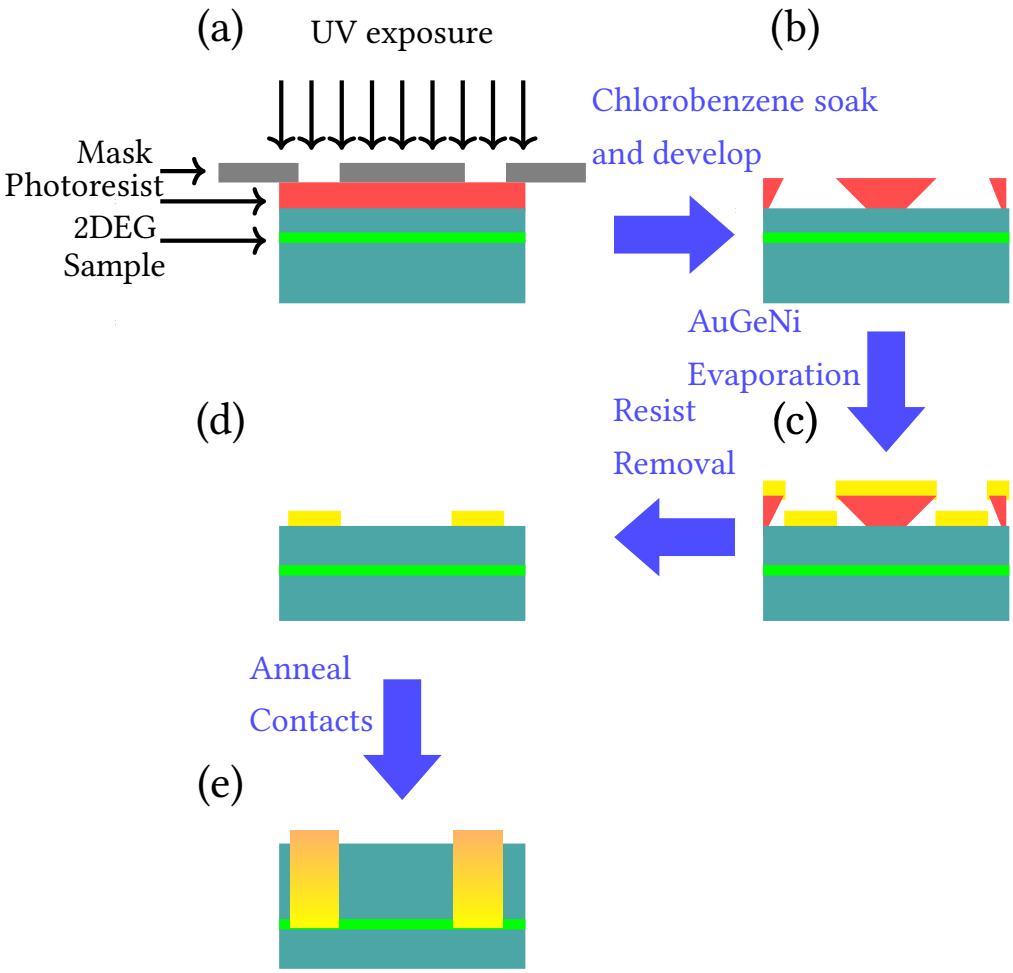

Figure 3.7: Electrical connection to the 2DEG is through the fabrication of Ohmic contacts. (a) Photolithography begins by exposing the resist-coated chip to a pattern using UV light. (b) After exposure with the mask aligner, the sample is soaked in chlorobenzene. (c) The chlorobenzene hardens the surface of the resist so that it develops more slowly, resulting in an undercut profile without this, it is not possible to remove the underlying resist and the unwanted metal from the structure. (d) The chip is developed and loaded into an evaporator for metal deposition; resist and excess metal removal follows. (e) Rapid thermal annealing (RTA) enables the diffusion of deposited metal into the crystal, creating a contact to the conducting layer.

3.4.2 Ohmic contact processing conditions

Samples A and E were fabricated using the eutectic metal deposition technique, by thermally evaporating $120\,\mathrm{mm}$ of AuGeNi from a eutectic slug (by weight: 83% Au, 5% Ni, 12% Ge). The layered samples were fabricated in different batches using the layered metal deposition technique by evaporating either a $0\,\mathrm{nm}$ or $3\,\mathrm{nm}$ Ni layer, then a eutectic AuGe (by weight: 88% Au, 12% Ge), then a further Ni layer and finally a Au capping layer. Annealing conditions for all contacts were the same: annealed in a forming gas (N2 + H2) at $430\,^{\circ}\mathrm{C}$ in a rapid thermal annealer (RTA) for $80\,\mathrm{s}$. These conditions give the lowest R_C, in agreement with the U-shaped dependence of R_C on annealing temperature [12, 13, 19, 66]. The Ohmic contact processing conditions for all samples are summarised in Table 3.2.

Table 3.2: Ohmic contact processing conditions used in this thesis

Sample	Wafer	Batch	Metal deposition method	Recipe
A	W476	I	Eutectic	Au:Ge:Ni = 83:12:5 wt% = 160 nm
B	V834	II	Layered	3 nm Ni/136 nm AuGe/30 nm Ni/180 nm Au
C	V827	II	Layered	3 nm Ni/136 nm AuGe/30 nm Ni/180 nm Au
D	V834	III	Layered	0 nm Ni/130 nm AuGe/50 nm Ni/164 nm Au
E	W939	VI	Eutectic	Au:Ge:Ni = 83:12:5 wt% = 160 nm
F	V834	II	Layered	3 nm Ni/136 nm AuGe/30 nm Ni/180 nm Au
G	V834	III	Layered	0 nm Ni/130 nm AuGe/50 nm Ni/164 nm Au
H	V834	IV	Layered	0 nm Ni/139 nm AuGe/35 nm Ni/175 nm Au
I	V834	V	Layered	0 nm Ni/123 nm AuGe/30 nm Ni/200 nm Au
J	V834	II	Layered	3 nm Ni/136 nm AuGe/30 nm Ni/180 nm Au

Table of Ohmic contact processing conditions for the samples in this thesis. Samples A (Graham Creeth) and E (Pedro Vianez) were fabricated using the eutectic metal deposition technique, by thermally evaporating 120 mm of AuGeNi from a eutectic slug (by weight: 83% Au, 5% Ni, 12% Ge). Patrick See processed the layered contacts, fabricated in different batches by evaporating either a 0 nm or 3 nm Ni layer, then a eutectic AuGe (by weight: 88% Au, 12% Ge), then a further Ni layer and finally a Au capping layer. All contacts were annealed in a forming gas (N2 + H2) at 430 °C in a rapid thermal annealer (RTA) for 80 s.

3.5 Ohmic contact microstructure

To investigate the structural and chemical make-up of the Ohmic contacts used in this thesis, Scanning Electron Microscope (SEM) and Energy Dispersive X-ray (EDX) techniques are used to investigate the contacts on Sample J. As shown in Fig. 3.8, investigations take place in two locations of the Ohmic contact, the centre (bulk) and the edge. Two perspectives of the contact are investigated: the top and a cross-sectional side-view, achieved using a Ga-ion beam to mill a trench; the side-view images where taken are by Dr. Joanna Waldie, who gave technical help, at the University of Cambridge.

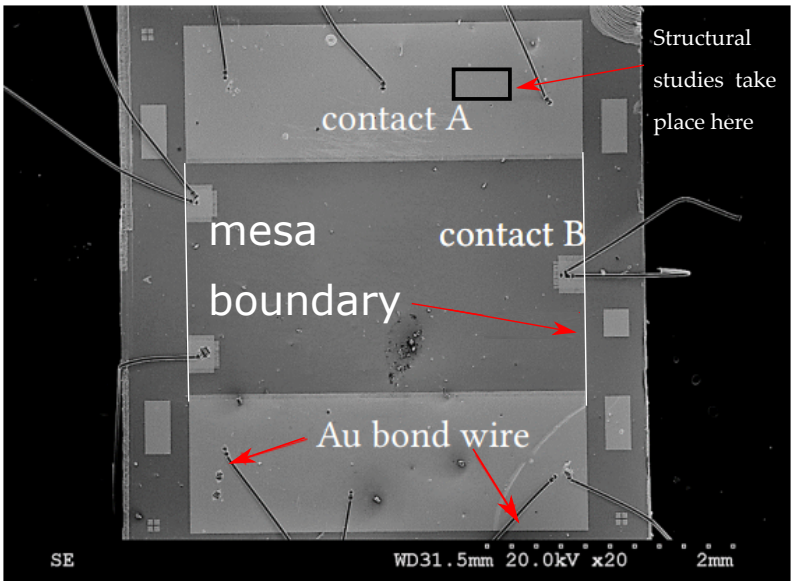

Figure 3.8: Scanning Electron Microscope (SEM) and Energy Dispersive X-ray (EDX) analysis of Sample J. The lighter grey bonded regions are the Ohmic contacts and indicated with a white line, the mesa boundary. Surface SEM images and EDX data is taken from contact A and B; cross sectional data is taken from contact A.

3.5.1 In the bulk of the contact

Figure 3.9(a) shows a surface study in the centre of contact B where a $5\,\mu m \times 5\,\mu m$ region is chosen from a larger $25\,\mu m \times 25\,\mu m$ area. The images show a surface morphology with a grains of order $\approx 1\,\mu m$. In Fig. 3.9(b) EDX mapping reveals a Au rich surface that surrounds the Ni-rich grain with a presence of Ga and of Al as reported[67, 68]; it is not clear what has replaced Al if Al has diffused out. The dark areas in the SEM images are shown to be Ni, As and Ge-rich regions, this has been previously reported by Kumar[69] and Ga is present everywhere.

Figure 3.9(c) shows the sidewall of a trench cut into contact B, using a Ga focused ion beam. The light material just below the surface is Au-rich, within it and near the semiconductor interface are dark Ni-rich inclusions that are $0.1\,\mu m - 0.5\,\mu m$ in size; the Ni-rich regions viewed from above are larger grains penetrating down. The EDX maps show that the inclusions contain no Au, but have high concentrations of Ni and As, as shown in the surface data.

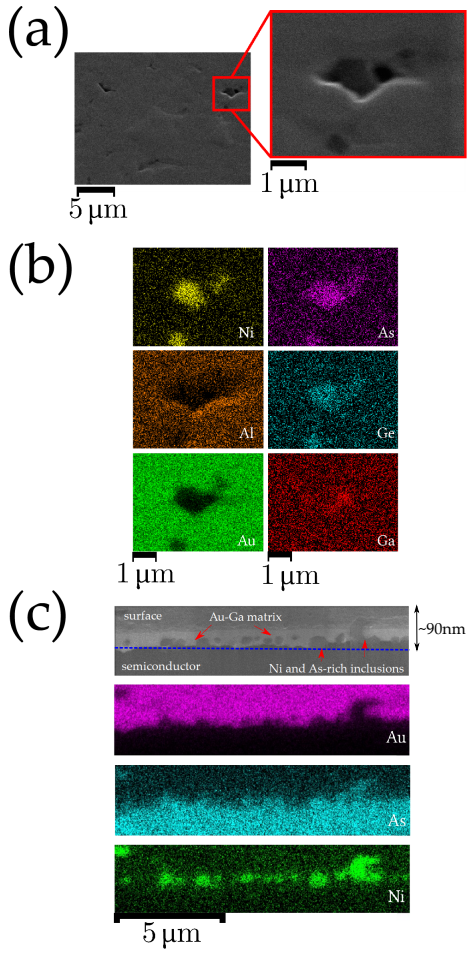

Figure 3.9: Surface and cross-sectional SEM and EDX data of the bulk of the Ohmic contact of Sample J. (a) The surface morphology shows dark grains of the order $5\,\mu m$ or less. (b) Surface EDX elemental mapping not only reveals a contrast between the Au and Al region and the Ni, Ge and As-rich grains, but also that Ga seems to be ubiquitous. (c) The sidewall structure and EDX mapping exposes an As region and Ni-rich inclusions below the Au-rich surface. It is observed that the larger Ni inclusion on the far right-hand side is big enough to protrude up to the surface.

3.5.2 At the edge of the contact

Figure 3.10 shows at the edge of the contacts are 'fingers' $\approx 5\,\mu m$ wide and $30\,\mu m$ long. The Au-rich smooth surface contains smaller amounts of Al and Ga while the edges of the fingers are Ni and Ge-rich. Underneath the surface is Ni, Ge and As-rich inclusions $<1\,\mu m$. At the edge of the fingers are sub-micron to μm regions where the material appears to be 'eaten up'. Spectra point analysis shows these regions contain high amounts of Au, Ga, Ge, Ni and As, see inset of Fig. 3.10(b); the C shown in the analysis is the carbon tab that the sample is mounted to.

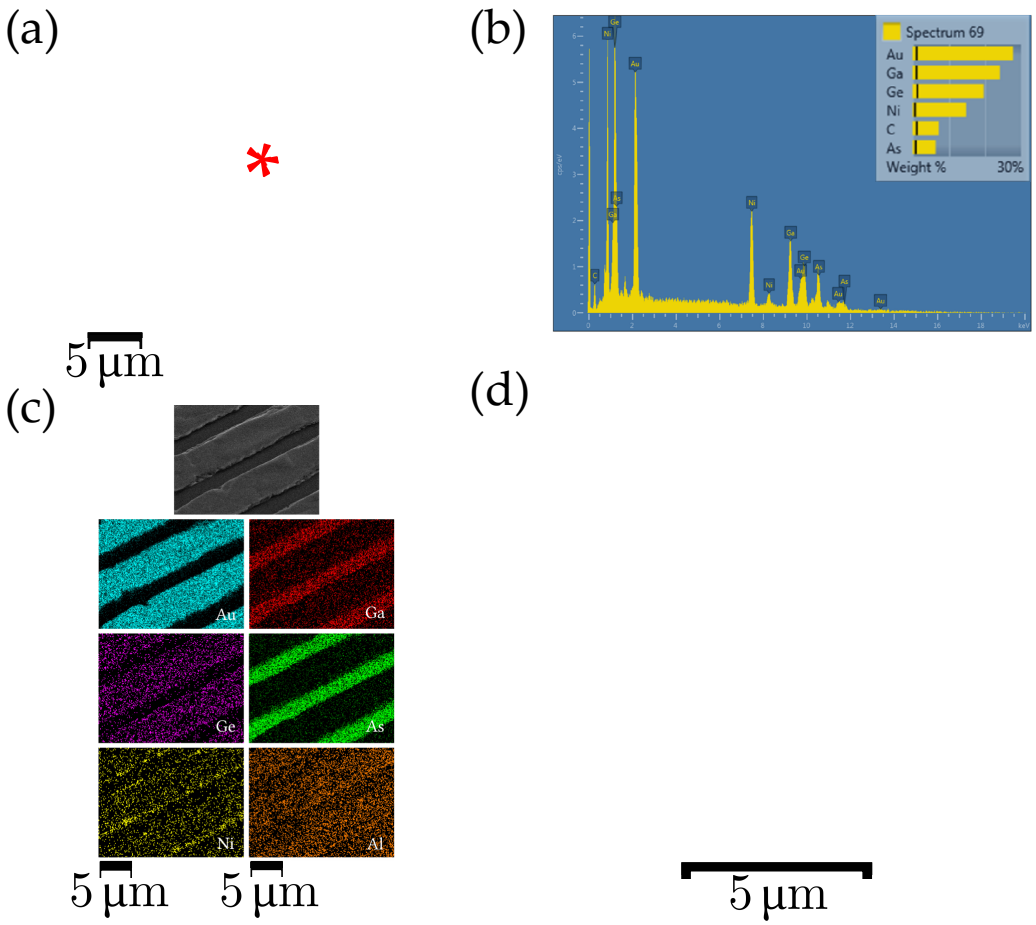

Figure 3.10: Surface and cross-sectional SEM and EDX data at the edge of the Ohmic contact of Sample J. (a) The surface morphology of the fingers is generally smooth except at the edges where the material appears to be 'eaten up' leaving µm rougher surface regions. EDX spectra is taken at the red ⋆. (b) The EDX spectra shows the region rich in Au and Ga with a weaker presence of Ni, Ge and As. (c) Elemental surface mapping unveils Ni-rich edges and a Ge and Au-rich surface with a weaker presence of Al, Ga and As; the rich Ga and As regions between the fingers is the mesa. (d) Below the Au-rich surface is Ni, Ge and As-rich inclusions <1 µm.

3.5.3 Discussion

The investigation shows the surface consists of Ni, Ge and As-rich grains surrounded by Au, Ga and Al similar to Refs.[67, 69, 70]. The Au and Ga may be a form of AuGa alloy such as those already seen in AuGeNi contacts [23, 38, 39, 42, 67, 71–73]. Due to the use of a Ga-ion beam to achieve the side-view, Ga is not shown on EDX side-view mapping, but it is assumed to be present based on EDX spectra. Below the surface lies Ni, Ge and As-rich inclusions of order μm, this is concentrated at the semiconductor interface which, in some cases, consumes some of the GaAs unevenly, at the edge, the inclusions are $<1\,\mu\mathrm{m}$; this is identified to be NiAs, NiAs(Ge) or Ni_2GeAs[23, 25, 27–30, 36, 39, 40, 72]. Larger examples of these structures visible from above as Ni-rich grains, penetrate about $200\,\mathrm{nm}$ deeper than the Au-rich layer, probably reaching the 2DEG. Edge EDX maps confirm reports[74] that Ge leaves the metal layers and diffuses into the GaAs to be the *n*-type dopant in the GaAs.

Chapter 4

Low-temperature experimental techniques

4.1 Introduction

In this chapter, the experimental techniques applied to low-temperature measurements are shown. The chapter begins with a discussion on the low-temperature cryostat, this includes the $4.2\,\mathrm{K}$ liquid He Dewar and the dilution refrigerator and its operation. Thermometry for low-temperatures are then discussed including current sensing noise thermometry (CSNT). Then finally, the electrical transport section presents the circuits required to understand the measurements taken. In all measurements, sample data acquisition is by Cryomeas, written by Professor C. J. B. Ford at the University of Cambridge and the thermometry is read by Noise-fit, an in-house program designed for CSNT measurements, and Oxford Instruments' software that reads the resistor thermometers.

4.2 The dilution refrigerator and $4.2\,\mathrm{K}$ Dewar

Before samples are mounted onto a dilution refrigerator for an experiment, it is important to characterise the samples at low temperatures done using a $4.2\,\mathrm{K}$ liquid He Dewar. The typical protocol for assessment of samples at $4.2\,\mathrm{K}$ requires the sample to be mounted onto a measurement probe that is then inserted into the liquid He, this is called 'dipping'. The advantage of this process allows fast sample turn around and analysis; dilution refrigerator systems take much longer to cool down and warm-up and thus, it is important to have a known working and characterised sample so that fridge time is not wasted.

A dilution refrigerator is capable of achieving temperatures of $10\,\mathrm{mK}$, therefore samples mounted on these systems are able to be cooled down further then $4.2\,\mathrm{K}$ allowing temperature dependent behaviour to have a greater effect.

The main cooling process of the dilution fridge takes place in the mixing chamber where a mixture of ^{3}He and ^{4}He separate into a concentrated ^{3}He-rich phase and a ^{4}He-rich dilute phase; the separation occurs when $T \approx 0.7\,\mathrm{K}$. For the atoms to be pushed across the boundary, excess He needs to be removed using the still which acts as a distillation chamber, evaporating ^{3}He and is operated when $T \approx 0.7\,\mathrm{K}$. ^{3}He has a lower boiling point than ^{4}He, so heating the mixture distils the ^{3}He out of the ^{4}He creating less ^{3}He atoms in the mixture causing the ^{3}He atoms to cross the phase boundary from the concentrated phase into the dilute phase, absorbing heat; the entropy increases when atoms move from a pure phase into a dilute phase, cooling the system.

The dilution refrigerator is able to run continuously if the pumped ^{3}He gas from the dilute phase is cooled and returned to the concentrated phase; backing and roots pumps control the continuous circulation of the mixture. The ^{3}He returns via a nitrogen cooled cold trap and a He cooled cold trap to freeze out any impurities. The condenser is connected to the 1 K pot, which is cooled by pumping and cools to the temperature of the pot; the refilling of the 1 K pot is controlled with a manually operated needle valve and is continuously filled from the ^{4}He bath, for further information see Ref.[75]. Figure 4.1 shows a schematic of the operation of a dilution refrigerator.

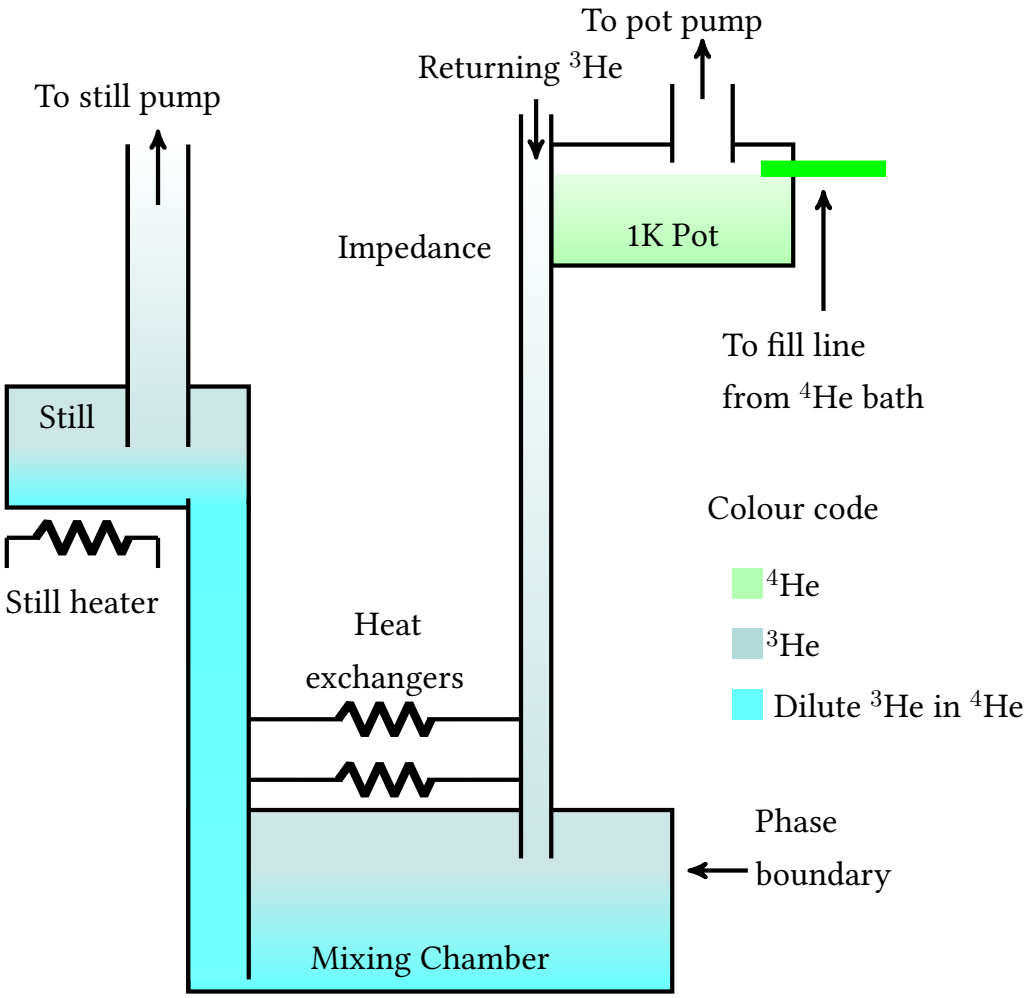

Figure 4.1: Schematic of the dilution refrigerator. The essential cooling process of the dilution fridge takes place in the mixing chamber. When $T \approx 0.7\,\mathrm{K}$, the mixture of ^{3}He and ^{4}He separates into a concentrated ^{3}He rich phase and a dilute ^{4}He rich phase. Upon cooling the mixture further, the top concentrated phase tends to $100\,\%$ of ^{3}He and the dilute phase tends to $6.6\,\%$ of ^{3}He, this is maintained even as $T \to 0$; the ^{3}He is pumped from the dilute phase in the still. In order to maintain the $6.6\,\%$ dilute phase, ^{3}He is evaporated causing cooling to occur. The heat exchangers are on the return line for the incoming hot ^{3}He. To run the dilution refrigerator continuously, the pot pump and still pump keep the pot running and the system circulating. The still is heated to increase circulation and cooling power via the still heater. The $1\,\mathrm{K}$ pot is maintained at $1\,\mathrm{K}$ and is continuously filled from the liquid ^{4}He bath.

In this thesis, there are two Oxford Instruments dilution refrigerators used for different experiments, the Kelvinox 400 and the Triton 200 cryogen-free dilution refrigerator.

Figure 4.2(a) shows the Oxford Instruments' Kelvinox 400 conventional 'wet' refrigerator that operates as described; the term 'wet' means there is a main ^{4}He bath. The cryostat can be controlled and the temperature data can be read by the Kelvinox Integrated Gas Handling monitor (IGH monitor), this is software provided by Oxford Instruments. The diagnostic thermometry is measured using calibrated resistor thermometers and the magnetic field is created by a superconducting magnet sitting inside the main He bath.

Figure 4.2(b) shows the Triton 200 cryogen-free dilution refrigerator; cryogen-free or 'dry' means there is not a main ^{4}He bath. This system is automated and it is a closed cycle system, so no transfer of helium is required. The dilution unit is the same as that used in a conventional dilution refrigerator and there is a small mixture of ^{4}He and ^{3}He in a helium gas tank or 'dump', but instead of a He bath, the cooling is achieved with a pulse tube pre-cooling stage. For a full cool down, the pulse tube is turned on and the pre-cool circuit is cooled to $3\,\mathrm{K}$. Once cold, the mixture is added from the dump and is circulated through the dilution unit where it continues cooling on each cycle of the liquid until the base temperature is reached.

In a conventional wet fridge, the size of the experimental stages is limited by the size of the neck of the He Dewar; the He Dewar has a neck with a small diameter, to reduce the rate of liquid He boil off. In a cryogen-free system, the diameter of the plates is not limited by this factor, so they can be much larger, increasing the amount of experiments that can be run at one time. Typically, the cryogen-free refrigerator is not ideal for sensitive measurements, the pulse tube is a source of mechanical noise, but in the Triton 200 cryogen-free dilution refrigerator the pulse tube is decoupled from the system reducing the vibrations. Both refrigerators typically have a base temperature $T \approx 10\,\mathrm{mK}$.

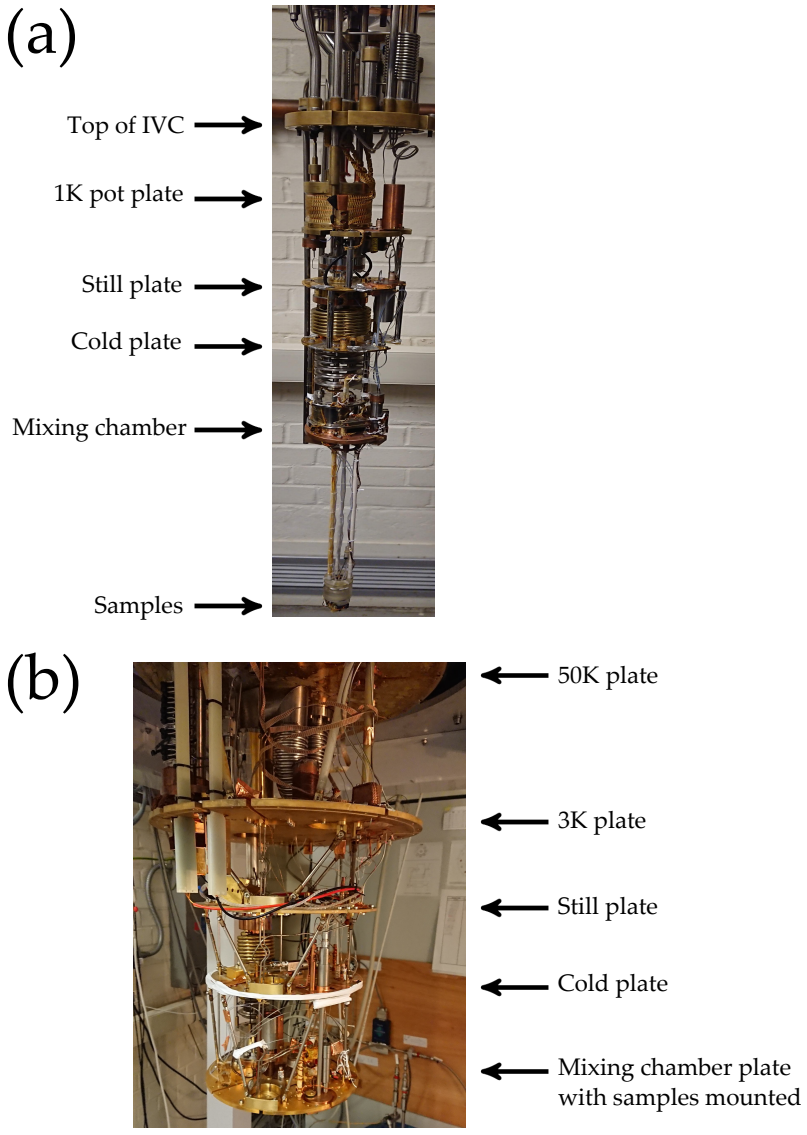

Figure 4.2: (a) The 'wet' Kelvinox 400 dilution refrigerator. In the conventional 'wet' refrigerator, the He Dewar has a neck with a small diameter to reduce the rate of He liquid boil off. (b) The 'dry' Triton 200 cryogen-free refrigerator. In a cryogen-free system, the plate diameter is not limited by this factor, because there is a small charge of ^{3}He and ^{4}He mixture, which is operated with a pulse tube refrigerator pre-cooling stage. Therefore, due to no He boil off, the experimental plates are much larger. When the cryogen-free dilution refrigerator is cooled below $T \approx 3\,\mathrm{K}$, the dilution system will continue the cooling process.

4.3 Thermometry

4.3.1 Primary and secondary thermometers

Temperature is the critical parameter when performing experiments at low T, and thus reliable thermometers are required to measure this. Therefore, accurate temperature measurement is required and the ideal calibrated thermometer will have low dissipation, rapid thermal response, cover a wide temperature range, be traceable to temperature scales and be independent of a magnetic field B.

Thermometers can either be primary, where they do not have to be calibrated against a fixed point, or secondary where they cannot be used reliably as temperature sensors unless calibrated at a fixed point or many fixed points.

Generally, commercial calibrated ruthenium oxide (RuO_2) resistance thermometers are mounted on various parts of the cryostat and work convincingly to $T \approx 50\,\mathrm{mK}$, but other thermometers such as current sensing noise thermometry (CSNT) developed at Royal Holloway[76] are used in this thesis for lower temperatures and better accuracy; the CSNT can accurately, to 1%, measure temperatures from $550\,\mu\mathrm{K}$ to $4\,\mathrm{K}$.

4.3.2 Current sensing noise thermometry

A calibrated fast-response CSNT is an effective essential tool in low-temperature measurements and was designed, built and tested with intention of mounting it onto the Kelvinox mixing chamber in the future; calibration was performed on the Triton 200 mixing chamber using a RuO_2 thermometer and a slower primary CSNT with previously published results, see Ref.[77]. Figure 4.3 shows the electrical diagram of a CSNT.

A CSNT operates by measuring the Johnson noise in a sensor resistor; Johnson noise is the electronic noise generated by the thermal movement of charge carriers in a conductor, inducing a small and measurable current to flow. The resistive element of a CSNT is coupled to a low T_c DC SQUID, used as the front-end amplifier and the thermal Johnson noise in the sensor is measured; the operation of a DC SQUID is described in detail in Ref.[78]. This resistor is a metal that has a resistance that does not vary below $T < 4\,\mathrm{K}$ and is assumed to be constant in these temperature ranges. The current noise measured in a CSNT is linked directly to the Boltzmann constant k_B so in principle, it can be used as a primary thermometer.

To measure the temperature T of a particular plate on a cryostat, such as the mixing chamber with a variable T, there is a thermal link made between the CSNT sensor resistor and the plate. It is inductively coupled to the SQUID, which is thermally linked to a fixed T plate such as the cold plate at $100\,\mathrm{mK}$. The SQUID amplifies the thermal noise current of the resistor and the room temperature electronics read out the output of the SQUID. The mean square current noise flowing through the SQUID input coil, per unit bandwidth is,

$$\langle I_N^2 \rangle = \frac{4k_BT}{R} \times \frac{1}{1+\omega^2\tau^2}, \tag{4.1}$$

where $\omega = 2\pi f$ and $\tau = L/R$; the inductance L is dominated by the DC SQUID input coil L_i, shown in Fig. 4.3.

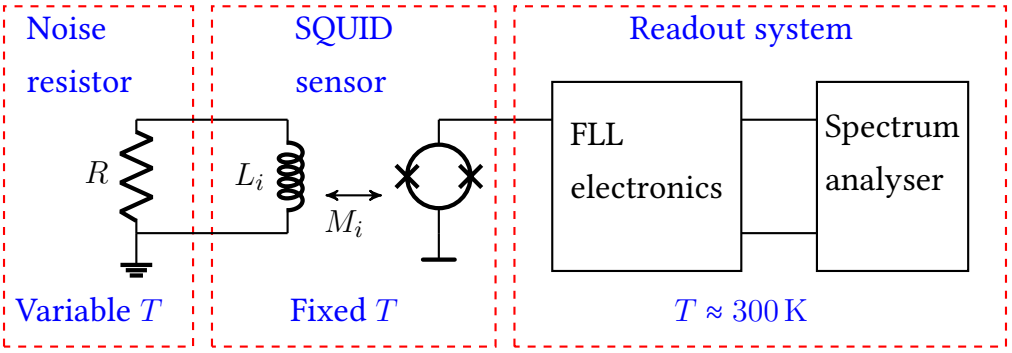

Figure 4.3: Schematic of the current sensing noise thermometer (CSNT), which measures the Johnson noise in a noise resistor. The resistive element is coupled to a low T_C DC SQUID that is used as the front-end amplifier to measure the thermal Johnson noise in the sensor. This resistor R is a metal that does not vary in resistance below $T < 4\,\mathrm{K}$.

The resistance R of the sensor is chosen either for reduction in measurement time or reduction in the noise temperature; this results in a fast, high resistance thermometer or a slow, low resistance thermometer; a fast CSNT with high R and larger bandwidth captures noise traces more quickly, but a slow CSNT with low R has a lower roll off frequency and a longer sampling time. The initial tests of the CSNT were performed at $4.2\,\mathrm{K}$ and once mounted on the Triton 200, the primary CSNT and RuO_2 thermometer verified the calibration at $T = 1\,\mathrm{K}$ ensuring reliability.

In Fig. 4.4(a), the fast CSNT is shown to connect to the input coil of the SQUID through a filtered pair of Nb screw terminal joints and a superconducting twisted pair of NbTi wires providing a superconducting connection. The NbTi wires connect the CSNT on the mixing chamber plate to the SQUID on the $100\,\mathrm{mK}$ plate, and are threaded through a PTFE sleeve with Apiezon N grease injected inside the sleeve to reduce any vibrations of the superconducting wire reducing unwanted the noise.

Figure 4.4(b) shows the sensor resistor is made up of Cu foil of $R = 2\,\mathrm{m\Omega}$ with one side grounded to the Cu base and the floating side spot welded to Nb foil via PtW wire; the heat leak to the floating side of the sensor is minimised by exploiting the poor thermal conductivity of superconducting Nb. The PtW wire link increases the total sensor resistance to a value $R = 256\,\mathrm{m\Omega}$. Good thermalisation between a sensor resistor and the thermometer holder is achieved by electrically grounding one end of the resistor to a large Cu volume; the electrons in the resistor are cooled by conduction through the direct link to the Cu mixing chamber plate in which the thermometer is mounted using a copper cone joint, see Fig. 4.4(c).

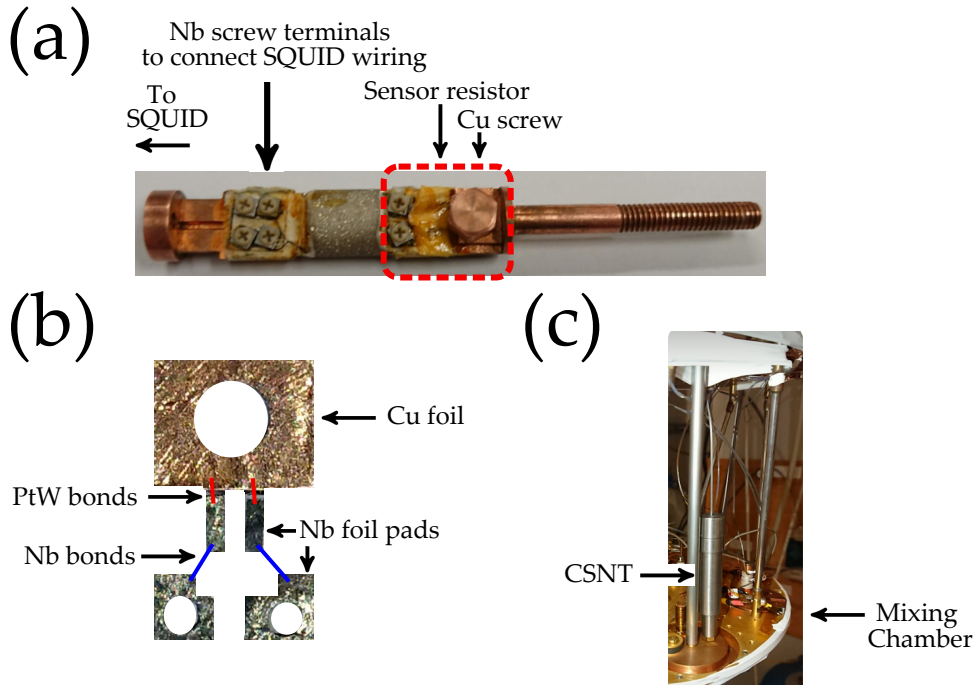

Figure 4.4: Design, assembly and mounting of the fast CSNT used in this thesis. (a) In a CSNT, the sensor resistor connects to the input coil of the SQUID through a pair of Nb screw terminals and a superconducting twisted pair of NbTi wires, providing the superconducting connection. To guarantee excellent thermalisation between the sensor resistor and the thermometer holder, one end of the resistor is electrically grounded using the Cu screw to clamp the sensor resistor circuit to the Cu body; this allows cooling of the electrons in the resistor by conduction through the direct link to the Cu plate in which the thermometer is mounted. (b) A photograph of the sensor resistor circuit. The Cu foil and Nb pads are spot welded together and then glued with GE varnish to the Cu body, electrical isolation between the sensor resistor circuit and the Cu body is ensured by using cigarette paper. The resistance for the sensor resistor comes from the PtW bonds connecting the Cu foil to the rectangular Nb pads. (c) The complete CSNT assembly mounted onto the mixing chamber. To stop excess noise pick up during measurements, Nb shielding surrounds the whole noise thermometer, SQUID and twisted pair.

To calibrate the fast CSNT, it is first mounted on the mixing chamber where both the RuO_2 resistance thermometer calibrated to $T \approx 50\,\mathrm{mK}$ and the primary CSNT with a sensor resistor of $R = 2.29\,\mathrm{m\Omega}$ is measured. The first fixed point on the fast CSNT is set when the temperature of the mixing chamber $T_{MC} = 1\,\mathrm{K}$ as measured by the RuO_2 resistance thermometer and the primary CSNT thermometer. Following this, different fixed temperature points were measured between $T_{MC} = 0.9\,\mathrm{K}$ and $T_{MC} = 0.1\,\mathrm{K}$ in steps of $0.1\,\mathrm{K}$, see Fig. 4.5(a); the noise spectrum defines the absolute temperature, if T is reduced the noise temperature T_N is lowered. Figure 4.5(b) shows the calibration of the fast CSNT against the primary CSNT and the RuO_2 resistance thermometer; the resistance of the RuO_2 is shown on the y-axis.

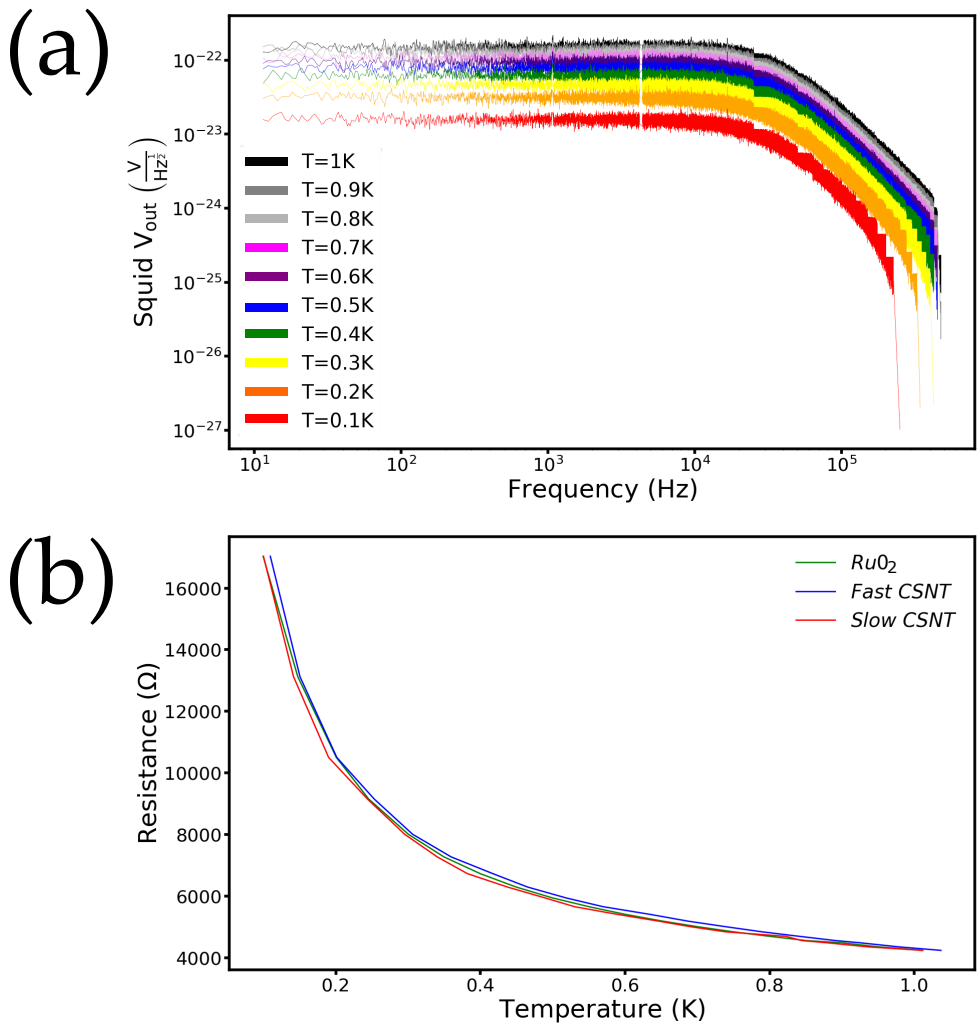

Figure 4.5: Calibration of the fast CSNT. (a) Frequency dependence of the SQUID output voltage as a function of temperature. The voltage noise measured in a noise thermometer is linked directly to the Boltzmann constant k_B so it can be used as a primary thermometer. (b) To calibrate the fast CSNT, the mixing chamber is stabilised at $1\,\mathrm{K}$ for fixed-point calibration against the previously calibrated RuO_2 resistance thermometer calibrated to $T \approx 50\,\mathrm{mK}$ and a slower CSNT used as the primary thermometer.

4.4 Electrical circuits for transport measurement

Resistance measurements are often made using the two-terminal (2T) method shown in Fig. 4.6. This is performed by a test current I flowing through the test leads and the resistance under test R. The voltage V is then measured across the R through the same set of test leads.

The problem with this method when applied to low resistance measurements, is that the total lead resistance R_{LEAD} is added to the measurement. Thus, the total measured two-terminal resistance R_{2T} between two Ohmic contacts is,

$$R_{2T} = 2R_C + R_{2DEG} + (2 \times R_{LEAD}), \tag{4.2}$$

where $R_{2DEG} = R_{\square} \times (L/W)$, which is the length over width ratio (L/W) multiplied by the resistance per square $R_{\square}$.

Due to the limitations of the 2T method, the four-terminal (4T) method shown in Fig. 4.7 is preferred because it reduces the effect of R_{LEAD} and R_C. In this configuration, I flows through resistance under test using one set of test leads, while the voltage is measured through a second set of leads. In practice, the voltage drop across the voltage leads is negligible and the voltage measured is essentially the same as the voltage across the resistance under test, resulting in a more accurately determined resistance value compared to the 2T method.

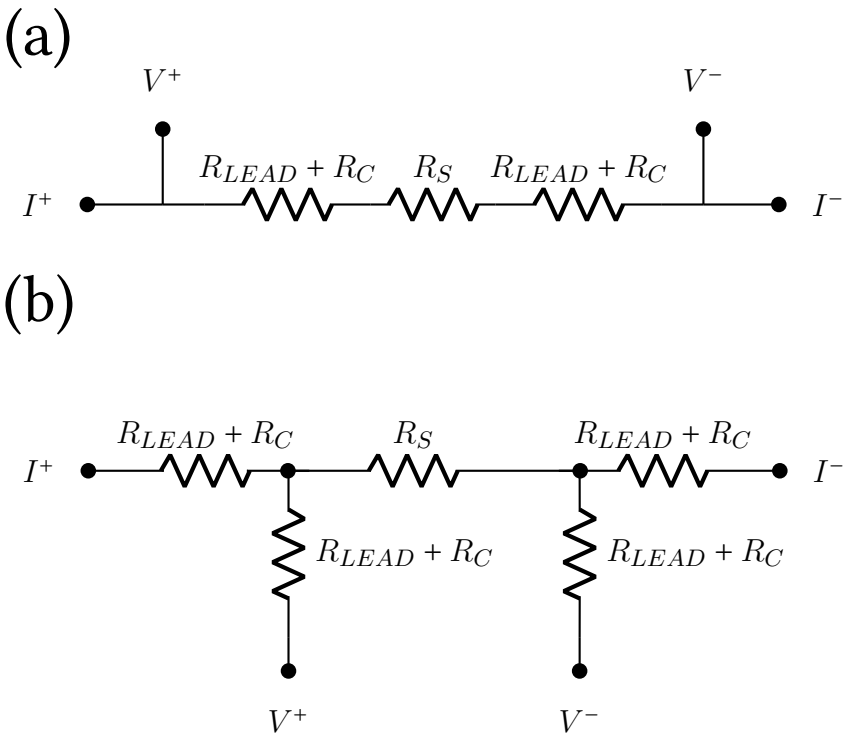

Figure 4.6: A simple contrast between two-terminal and four-terminal measurements. (a) The terminal circuit shows if a current I flows through the test leads and the sample resistance R_S, the voltmeter measures the resistance through the same set of test leads and the total lead resistance $R_{LEAD} \times 2$ and contact resistance $2R_C$ is added to the measurement therefore, $R_{2T} = R_S + 2R_C + (2 \times R_{LEAD})$. (b) The four-terminal measurement circuit shows when a current I flows through R_S using one set of test leads, the voltage across R_S is measured through the second set of leads. The resistance in the voltage probes is very large compared to the resistance of the sample, this means any current flowing through them is negligible and the voltage probes will only pick up the voltage drop between them, therefore, only R_S is measured.

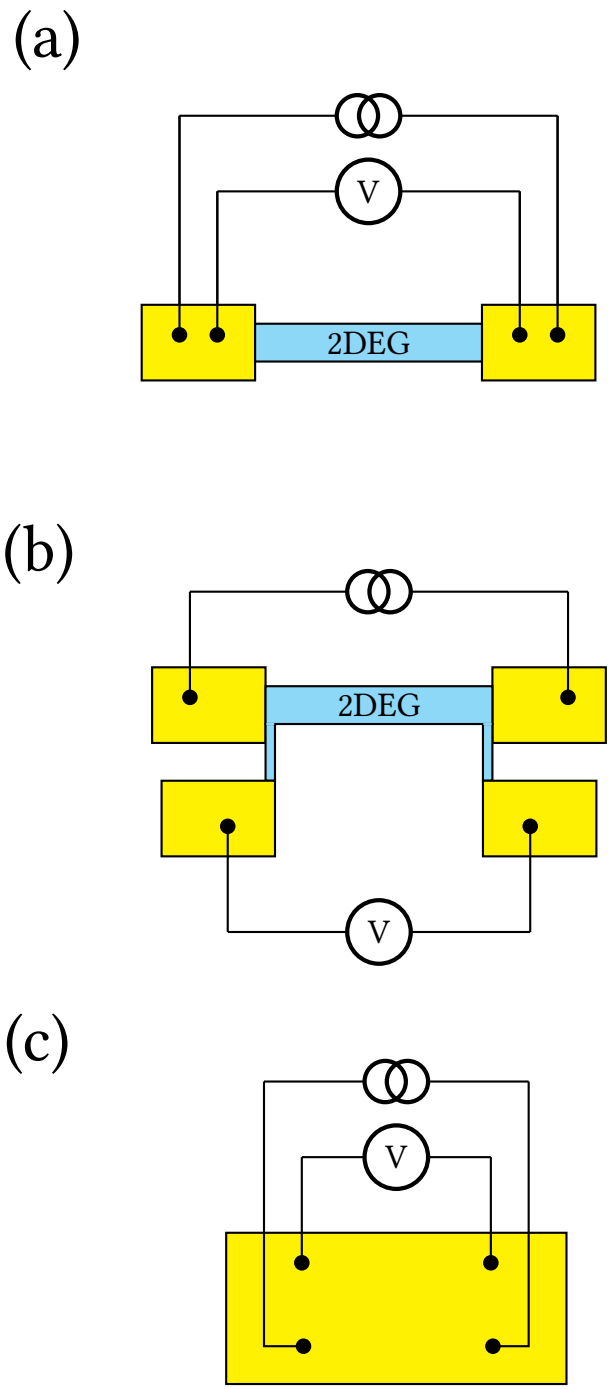

Figure 4.7: Examples of four-terminal measurements. (a) A four-terminal two-terminal $4T-2T$ circuit between two Ohmic contacts, in this circuit R_{2DEG} and R_C dominates. (b) A four-terminal measurement between four Ohmic contacts to measure R_{2DEG}. The current is attached across two Ohmic contacts and spans the intended area of measurement while the voltage probes, attached to separate contacts, are along the current path measuring the voltage drop between the probes. (c) A four-terminal measurement of one Ohmic contact.

Chapter 5

Simulations of arbitrary shaped 2DEGs

5.1 Introduction

In this chapter, we examine the electrical resistance, (and hence thermal resistance through the Wiedemann-Franz law) of the $4\,\mathrm{mm} \times 4\,\mathrm{mm}$ 2DEG device used in electron cooling experiments, see Ref.[79] and contact resistance measurements in this thesis.

The Wiedemann-Franz law (WFL) relates electrical conductivity

$$\sigma = \frac{ne^2\tau_\sigma}{m}, \tag{5.1}$$

and the thermal conductance

$$\kappa = \frac{\pi^2 n k_B^2 T \tau_\kappa}{3m}, \tag{5.2}$$

and defines the ratio of κ to σ of a material is directly relative to the temperature given as,

$$\frac{\kappa}{\sigma T} = L_0 T = \frac{\pi^2 k_B^2}{3e^2} T \tag{5.3}$$

where L_0 is the Lorenz number, n is carrier density, e is electron charge, m is mass and k_B is the Boltzmann constant.

WFL is observed in many metals and semiconductors, but is violated in superconductors where the electrical current is transported by Cooper pairs which, due to lack of entropy, do not carry heat.

By simulating current flow between two contacts, we can see the electrical resistance and therefore, the thermal resistance for a particular set-up. The numerical studies use FlexPDE to solve Laplace's equations. FlexPDE is a partial differential equation (PDE) solver and allows treatment of finite-element analysis as a mathematical tool.

The idea of FEA is to divide the domain of interest into sub-regions of simple shapes and to solve over each one of those simultaneously. The program divides the domain into cells of prisms of triangular cross-sections, this is a mesh-map and solves a PDE by determining the values of the dependent variable at the corners of the triangles and at the midpoints between corners.

5.1.1 Wiedemann-Franz law and thermal transport between two contacts

We now explain that to achieve a 2DEG low electron temperature, the total resistance R_T between two contacts need to be minimised.

To begin, Fourier's law of thermal conduction shows that the local heat flux density q, is given as,

$$q = -\kappa \nabla T. \tag{5.4}$$

where $-\nabla T$ is the negative local temperature gradient. Fourier's law in one-dimension in the x-direction is given as,

$$q(x) = -\kappa \frac{dT}{dx}. \tag{5.5}$$

We can also see that the Joule heating effect along a length can be written as,

$$\frac{d}{dx}\left[\frac{L_0 T(x)}{R}\frac{d}{dx}T(x)\right] = \frac{-V^2}{R} \tag{5.6}$$

where $L_0 = \frac{\pi^2 k_B^2}{3e^2}$ and $\frac{-V^2}{R}$ can be $\dot{Q}$. Solving this gives,

$$T(x) = \sqrt{T_0^2 + \frac{3}{\pi^2}x(1-x)(\frac{eV}{k_B})^2} \tag{5.7}$$

and

$$T^{\frac{1}{2}} = \frac{\sqrt{3}}{3\pi}\frac{eV}{k_B} \approx 0.22\frac{eV}{k_B}. \tag{5.8}$$

Demonstrating that the hottest part of a current carrying length is the middle. Therefore, to achieve a 2DEG low electron temperature, the total resistance R_T between two contacts need to be minimised, this is the contact resistance R_C and the 2DEG resistance R_{2DEG}.

5.1.2 Why it is important to reduce contact resistance R_C and 2DEG resistance R_{2DEG}

In this section, we discuss why it is important to reduce R_C and R_{2DEG} when cooling electrons in a 2DEG, which is the fundamental aim of this thesis.

The contact resistance R_C of a 2DEG is the resistance between the top of the Ohmic contact and the edge of 2DEG, it is the primary resistance determining the cooling of the sample through leads and arises during the annealing process; R_C is in series to the 2DEG and the 2DEG resistance R_{2DEG} cannot be measured without measuring R_C, see Fig. 5.1. Many experimental factors influence the R_C to a 2DEG: the depth of the 2DEG; the thickness of the AlGaAs layer; the sequence, thickness and composition of the contact metals layers; the target temperature of the rapid thermal annealer; the annealing time; the mobility of the 2DEG; and the quality of the sample surface before deposition. Thermal conduction from the lattice to the electron gas will occur predominantly through the Ohmic contacts of the sample and the leads connected to them, since the electron-phonon coupling is very weak below $T < 1\,\mathrm{K}$[80].

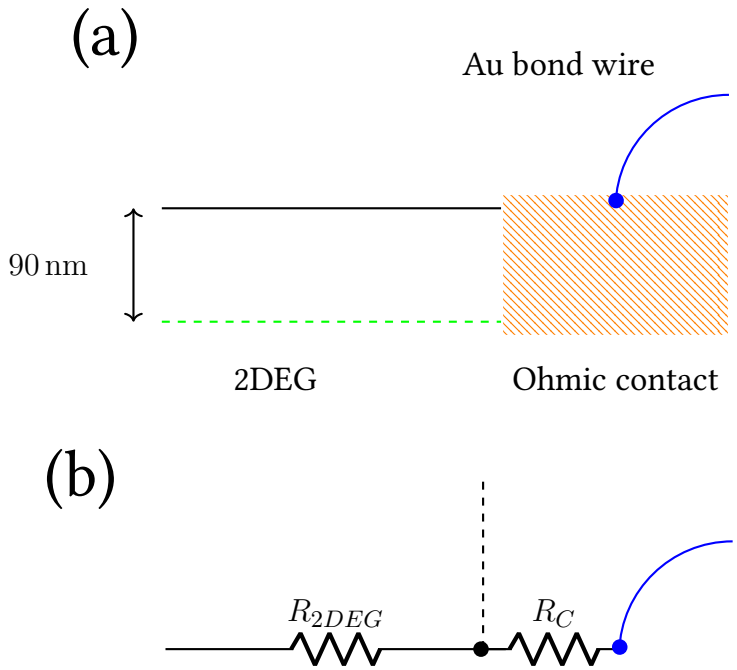

Figure 5.1: (a) A schematic of the 2DEG and Ohmic contact. To measure the 2DEG resistance R_{2DEG} the current must flow from the top of the Ohmic contact to the edge of the 2DEG, this is the contact resistance R_C. (b) Corresponding circuit showing the 2DEG resistance R_{2DEG} and contact resistance R_C are in series. To improve 2DEG cooling R_{2DEG} and R_C must be minimised.

At low T, the lattice and electrons thermally decouple, and if there is a heat leak to the 2DEG, the electrons will heat up to an electron temperature T_e that is higher than the lattice temperature T_L. The rate at which electrons thermalise and lose their excess energy to the lattice at T_L can be expressed as,

$$P = \dot{Q}(T_e) - \dot{Q}(T_L). \tag{5.9}$$

Heat $\dot{Q}$ as a function of temperature T in the system is experimentally[81] shown to be

$$\dot{Q}(T) = aT^5 + bT^2, \tag{5.10}$$

where aT^5 is electron-phonon cooling and the bT^2 is cooling via the Ohmic contacts.

We can explain this because surplus heat energy in a 2DEG is rapidly shared among the carriers through electron-electron interactions and an effective T_e is established, which may be considerably higher than the crystal T_L, to which both external thermometry and refrigeration are coupled.

The T^2 term represents heat conduction through the Ohmic contacts of the device; Ref.[81] has an experimental effective thermal conductance $\kappa \approx 1.0\mathrm{nWK}^{-2} \times T$, equivalent to a conductance $G \approx (20\Omega)^{-1}$. This term dominates at low temperatures when $T < 0.1\,\mathrm{K}$, where cooling of the electrons can be achieved only by thermal conduction through the contact wires. The magnitude of the thermal conduction term is important in device design for low temperature measurements, where it has proved difficult in the past to effectively cool a 2DEG below $50\,\mathrm{mK}$[5].

The T^5 dependence of $\dot{Q}$ is from the stimulated emission of acoustic phonons by hot 2D electrons, see Ref.[82]; coupling through a screened deformation potential (DP) yields $\dot{Q} \propto T^7$, whereas a screened piezoelectric (PZ) coupling gives $\dot{Q} \propto T^5$, so PZ coupling dominates at the lowest temperatures in GaAs when $T > 0.1\,\mathrm{K}$.

In summary, experimentally when $T > 0.1\,\mathrm{K}$ T^5 dominates, but when $T < 0.1\,\mathrm{K}$ the electrons are predominantly cooled through the contacts; for heat flow via electron diffusion, the power flowing out has a T dependence proportional to T_e^2 as compared to T_e^5 for the phonon case therefore, it is expected that phonon emission dominates at higher temperatures. Thus, to achieve $T_e \ll 0.1\,\mathrm{K}$ requires strong thermal coupling to the Ohmic contact, achieved by minimising R_C hence, in order improve the cooling of electrons in the 2DEG the two resistances that need to be minimised are the R_C and the R_{2DEG}.

The $4\,\mathrm{mm} \times 4\,\mathrm{mm}$ devices in this thesis, see Fig. 5.2, were designed to minimise R_C (with large area and perimeter) and R_{2DEG} (with small (L/W)) and then they were fabricated with two large $4\,\mathrm{mm} \times 1\,\mathrm{mm}$ Ohmic contacts on either side of a $4\,\mathrm{mm} \times 2\,\mathrm{mm}$ 2DEG and three $200\,\mu\mathrm{m} \times 200\,\mu\mathrm{m}$ contacts. There are two voltage $200\,\mu\mathrm{m} \times 200\,\mu\mathrm{m}$ probes on one side of the device and on the opposite side, a noise thermometer NT $200\,\mu\mathrm{m} \times 200\,\mu\mathrm{m}$ contact is placed the midpoint of the 2DEG, this will be bonded to a current sensing noise thermometer and models the cooling power as a simple resistor, obeying the Wiedemann-Franz resistance to heat model.

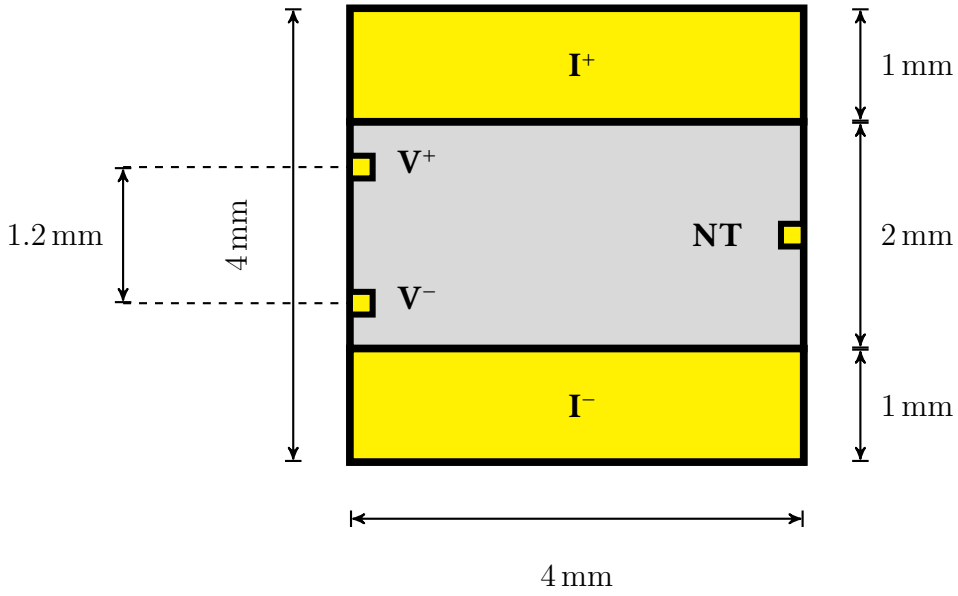

Figure 5.2: Schematic of a $4\,\mathrm{mm} \times 4\,\mathrm{mm}$ device. The Ohmic contacts are shown in yellow and the 2DEG in grey. The sample consists of two $4\,\mathrm{mm} \times 1\,\mathrm{mm}$ current contacts I^+ and I^-, on either side of a $4\,\mathrm{mm} \times 2\,\mathrm{mm}$ 2DEG. There are three $200\,\mu\mathrm{m} \times 200\,\mu\mathrm{m}$ contacts: two voltage probes V^+ and V^- and a noise thermometer contact labelled NT; in order to infer the electron temperature, a current-sensing noise thermometer[76] is attached to the 2DEG via NT and read out with a DC SQUID.

5.2 Background theory

Most materials are typically characterised by a bulk parameter called resistivity ρ, which can be thought of as a relationship between fields; ρ is an intrinsic property of materials that indicates how the current flows through the material by an electric field. If the current density $\vec{J}$ is at some point in the material and the electric field $\vec{E}$ is vector at that point, the two are related by Ohm's Law,

$$\vec{J} = \overleftrightarrow{\sigma}\vec{E}; \tag{5.11}$$

based on the current flow in Ohmic materials it is a diffusive motion of electrons driven by electric fields inside the materials. There are non-Ohmic materials in which Eq.5.11 does not apply because $\vec{J}$ has a very nonlinear dependence on $\vec{E}$. In a solid made of uniform Ohmic material, if two ends of a solid have Ohmic contacts, approximated as perfectly conducting, it is a resistor.

In a steady state problem, the charge density cannot change, and the divergence of $\vec{J}$ must vanish, or equivalently (since $\vec{J}$ and $\vec{E}$ are related by a constant),

$$\vec{\nabla} \cdot \vec{E} = \rho/\epsilon, \tag{5.12}$$

where the net electrical charge density is ρ. We can relate $\vec{E}$ to the electrostatic potential V by

$$\vec{E} = -\vec{\nabla}V, \tag{5.13}$$

and therefore, Eq. 5.12 is equivalent to Poisson's equation

$$\Rightarrow \nabla^2 V = \rho/\epsilon = \frac{-\rho}{\epsilon_0}. \tag{5.14}$$

where V is the electrostatic potential, ρ is the charge density and ϵ_0 is the dielectric constant.

The difference in the electrostatic potential V from one electrode to the other is the voltage applied across the resistor and the Laplace equation $\nabla^2 V = 0$ must be solved for the electrostatic potential V and the values of V at the electrodes must correspond to the voltages applied to the electrodes; $\nabla^2 V = 0$ is solved subject to the Dirichlet and Neumann boundary conditions. Further information on this topic is found in Refs.[83–85].

5.3 Simulation results

In this section, checks are performed to confirm the validity of the simulation, obtaining good agreement with theory, so that this is able to be employed to simulate the electrons in a $4\,\mathrm{mm} \times 4\,\mathrm{mm}$ 2DEG device; the numerical solutions of a simple device is used as an aid in estimating the resistances greater complexity and the analysis is able to show the current density at any point, this is useful when trying to avoid hot spots caused by nonuniform heating.

The typical method of experimentally assessing wafers is to measure carrier concentration n_{2D} and mobility μ using a four-terminal resistance measurement, the resistance R of a 2DEG is calculated as,

$$R = \frac{1}{\sigma} = \frac{1}{n_{2D} e \mu}, \tag{5.15}$$

where μ is the electron mobility and n_{2D} is the carrier density.

Resistance per square $R_\square$ is the sheet resistance of the 2DEG per square and is a characteristic property of a 2DEG, ρ and R have the same dimensions and are related by the dimensionless quantity L/W thus:

$$R = \rho L/W, \tag{5.16}$$

where L is the length and W is the width of the 2DEG channel and since $R_\square$ is independent of the size of each square, $\rho = R_\square$.

The total resistance R_T between two contacts is then given by

$$R_T = 2R_C + \frac{R_\square L}{W} = 2R_C + R_\square \times \frac{L}{W}, \tag{5.17}$$

where $L/W = N$ and R_C is the contact resistance, it is assumed the contact resistance for each contact is equal, see Fig. 5.3. For the following simulation checks, $R_C = 0$ and $R_\square = 1$ therefore, the problem to calculate the resistance, reduces to finding an effective N.

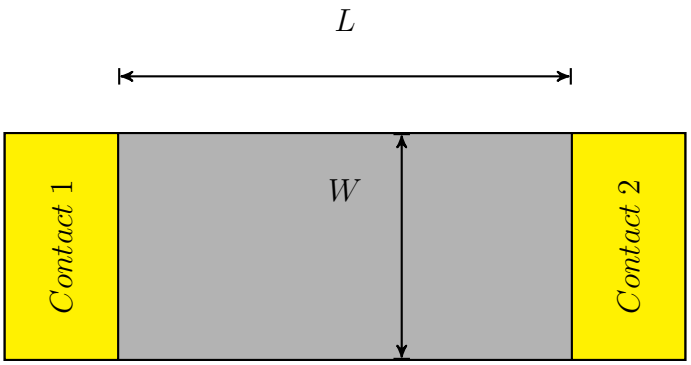

Figure 5.3: Schematic of a device showing length and width of a 2DEG channel. The total resistance R_T between two contacts is $R_T = 2R_C + R_\square \times \frac{L}{W}$, where R_C is the contact resistance, which is assumed to be equal, the contact resistance is not shown in this image.

5.3.1 Current flow around a bend

Shown in this section are two simulations of current flow around a bend, the first is when $N \gg 1$ and the second is $N \ll 1$, which therefore demonstrates the simulator. We begin with simulation of a simple device with current flow around a bend, this was originally theoretically calculated in Fig. 41 of Ref.[84] where $R_T = 2N + 0.57 \pm 0.01$. Fig. 5.4 shows two simulations of the device with a different L; the permittivity ϵ for the metal contacts is set to $\epsilon = 100$ and for the channel in between the contacts $\epsilon = 1$, this is the case for all simulations in this chapter. Figure 5.4(a) shows a device with dimensions of $L = 2\,\mathrm{mm}$ and $W = 1\,\mathrm{mm}$, in this geometry $N \gg 1$. From Ref.[84] the theoretical resistance of this geometry will be

$$R_T = 2 \times (2/1) + 0.57 \pm 0.01\Omega = 4.57 \pm 0.01\Omega. \tag{5.18}$$

In Fig. 5.4(d) the device now has dimensions $L = 0.5\,\mathrm{mm}$, $W = 1\,\mathrm{mm}$ and therefore, $N \ll 1$. The theoretical resistance is

$$R_T = 2 \times (0.5/1) + 0.57 \pm 0.01\Omega = 1.57 \pm 0.01\Omega. \tag{5.19}$$

The isopotential difference between the contacts for both devices is set to $10\,\mathrm{V}$ and 50% of the initial value is half way along the device, see Fig. 5.4(b) and Fig. 5.4(e). The current flow in both devices is uniform along the bar, flowing directly from one contact into the other and the current lines are closer together around the corner indicating a higher current density in this region, see Fig. 5.4(c) where the total current is 2.22 and Fig. 5.4(f) where the total current is 6.4. Therefore, the calculated resistance for the $2\,\mathrm{mm} \times 1\,\mathrm{mm}$ device is $V/I = R = 10/2.22 = 4.5\Omega$ and for the $0.5\,\mathrm{mm} \times 1\,\mathrm{mm}$ device, $V/I = R = 10/6.4 = 1.56\Omega$. From these values we can see that for both devices, the resistances are very close to the theoretical value, demonstrating the simulation method.

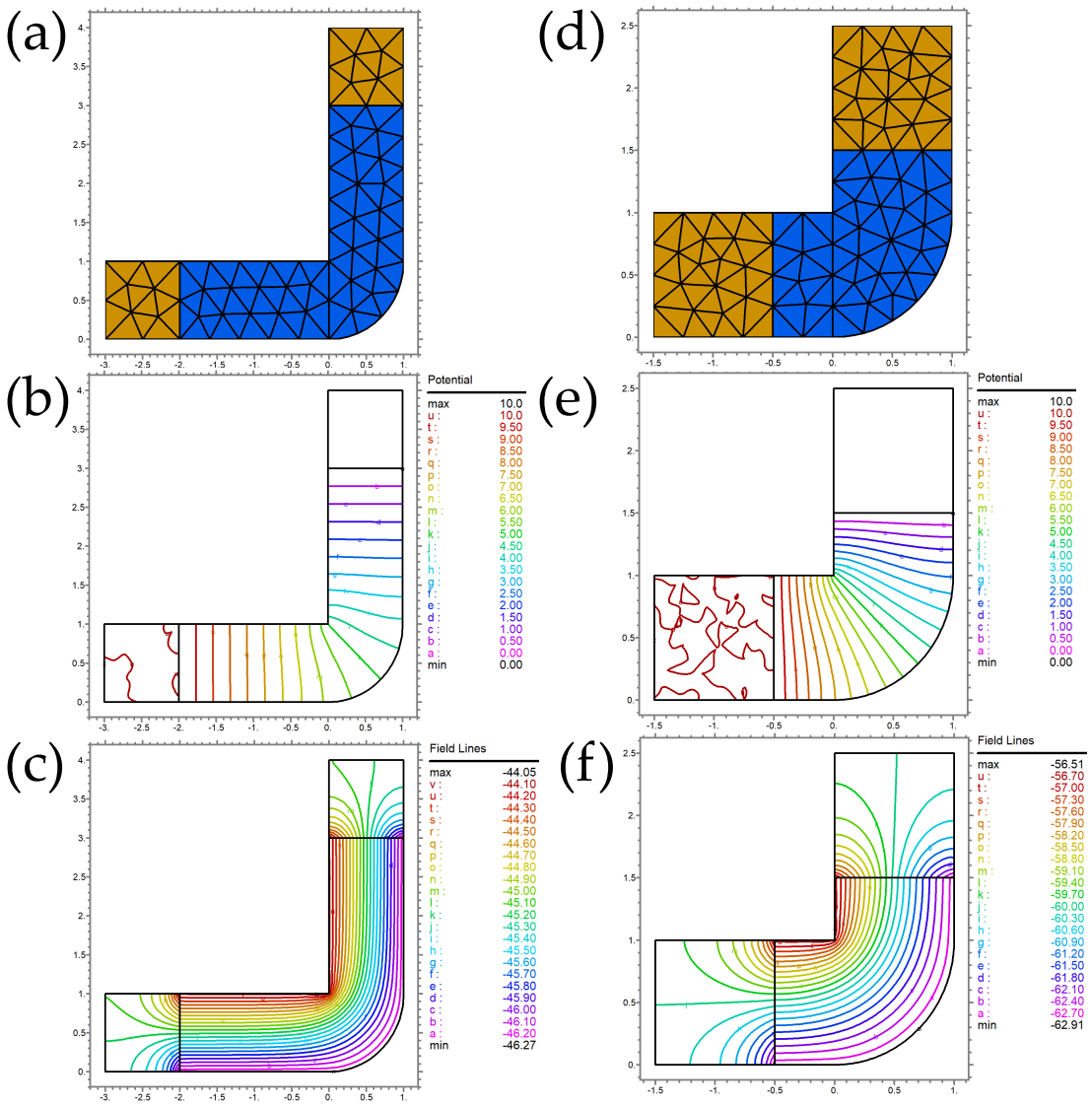

Figure 5.4: Simulations of a a $2\,\mathrm{mm} \times 1\,\mathrm{mm}$ device and a $0.5\,\mathrm{mm} \times 1\,\mathrm{mm}$ device with current flow around a bend. (a) The mesh-map of a for the $2\,\mathrm{mm} \times 1\,\mathrm{mm}$ device, the theoretical resistance is $R_T = 2 \times (2/1) + 0.57 \pm 0.01 = 4.57 \pm 0.01$. The mesa is blue and the contacts are yellow. (b) The potential difference (pd) for the $2\,\mathrm{mm} \times 1\,\mathrm{mm}$ device is set to $10\,\mathrm{V}$ drops by 50% of its initial value half way along the bar. (c) The field map shows the total current value is 2.22 and flow is uniform along the bar, flowing from one contact to the other with higher current density around the corner. The calculated resistance for the $2\,\mathrm{mm} \times 1\,\mathrm{mm}$ device is $R = 10/2.22 = 4.5\Omega$. (d) The mesh-map for the $0.5\,\mathrm{mm} \times 1\,\mathrm{mm}$ device, the theoretical resistance is $R_T = 2 \times (0.5/1) + 0.57 \pm 0.01 = 1.57 \pm 0.01\Omega$. (e) The pd for the $0.5\,\mathrm{mm} \times 1\,\mathrm{mm}$ device is dropped 50% half way along the bar. (f) The current flow is uniform and directly flows from one contact to the other with a higher current density around the corner and a total current value of 6.4. The calculated resistance for the $0.5\,\mathrm{mm} \times 1\,\mathrm{mm}$ device is $R = 10/6.4 = 1.56\Omega$.

5.3.2 Simulation of the J9 Hall bar device

Following the simulation of a simple device, we will next move onto a simulation of the J9 Hall bar device with dimensions $W = 80\,\mu\text{m}$ and $L = 1100\,\mu\text{m}$ thus, $R = N = 13.75$, see Fig. 5.5. This is commonly used by the Semiconductor Physics group and the University of Cambridge for measurements of electrical resistivity, carrier density n_{2D} and mobility μ. The device is measured by applying an electrical current on the end contacts and the voltage is measured between two voltage probes where the current is uniform, such as the middle and when the device is perpendicular to a B field, resistance $R(B_\perp)$ is measured; in the simulations presented, $B = 0$. 2D Hall bars are generally made with rectangular geometry, where the resistivity and thickness are uniform and the current I is supplied to and removed from the bar through contacts that have a lower resistance.

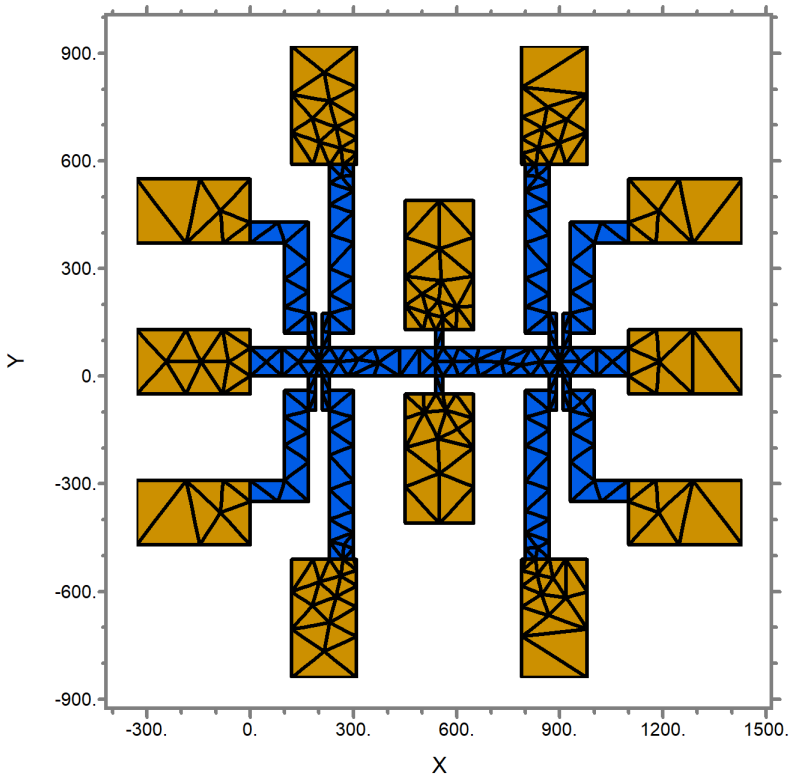

Figure 5.5: Simulation mesh-map of a J9 Hall bar showing the different regions, the mesa is blue and the contacts are yellow. The device has dimensions $W = 80\,\mu\text{m}$ and $L = 1100\,\mu\text{m}$, therefore the theoretical resistance without contributions from contact resistance or sheet resistance is $R = L/W = 13.75$. In a typical set-up, the current flows between the end contacts of the bar, situated on the x-axis in this picture and the voltage is measured between two probes, normally the middle probes these are situated either side of the Hall bar at X$\approx 550\,\mu\text{m}$.

Figure 5.6 shows isopotentials when 10V is applied to the end contacts, the simulation shows the potential difference (pd) half way along the bar is 50% of the initial value.

Figure 5.7 shows the current is not confined by the sides of the bar, there is a small bend in current flow along the entrances of the voltage probes. The calculated resistance from the simulation is $V/I = R = 10/0.73 = 13.69$, see the table in Fig. 5.7 for current values.

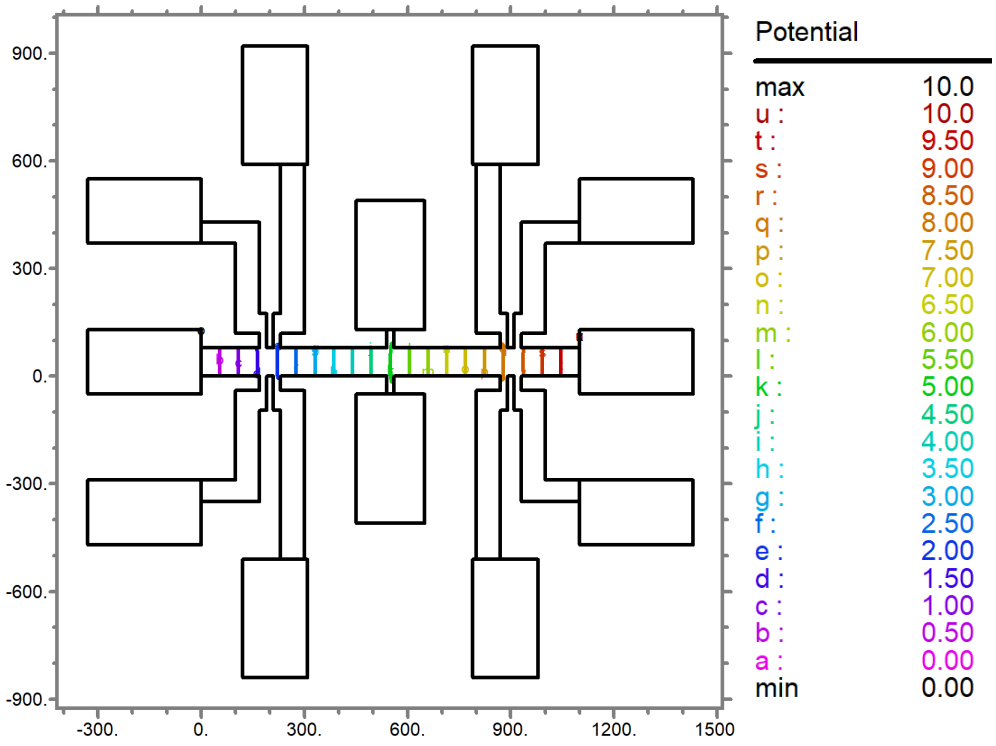

Figure 5.6: Simulation of a J9 Hall bar showing the potential between the current contacts. The potential, set to 10 V, is 50% of its initial value when half way along the bar.

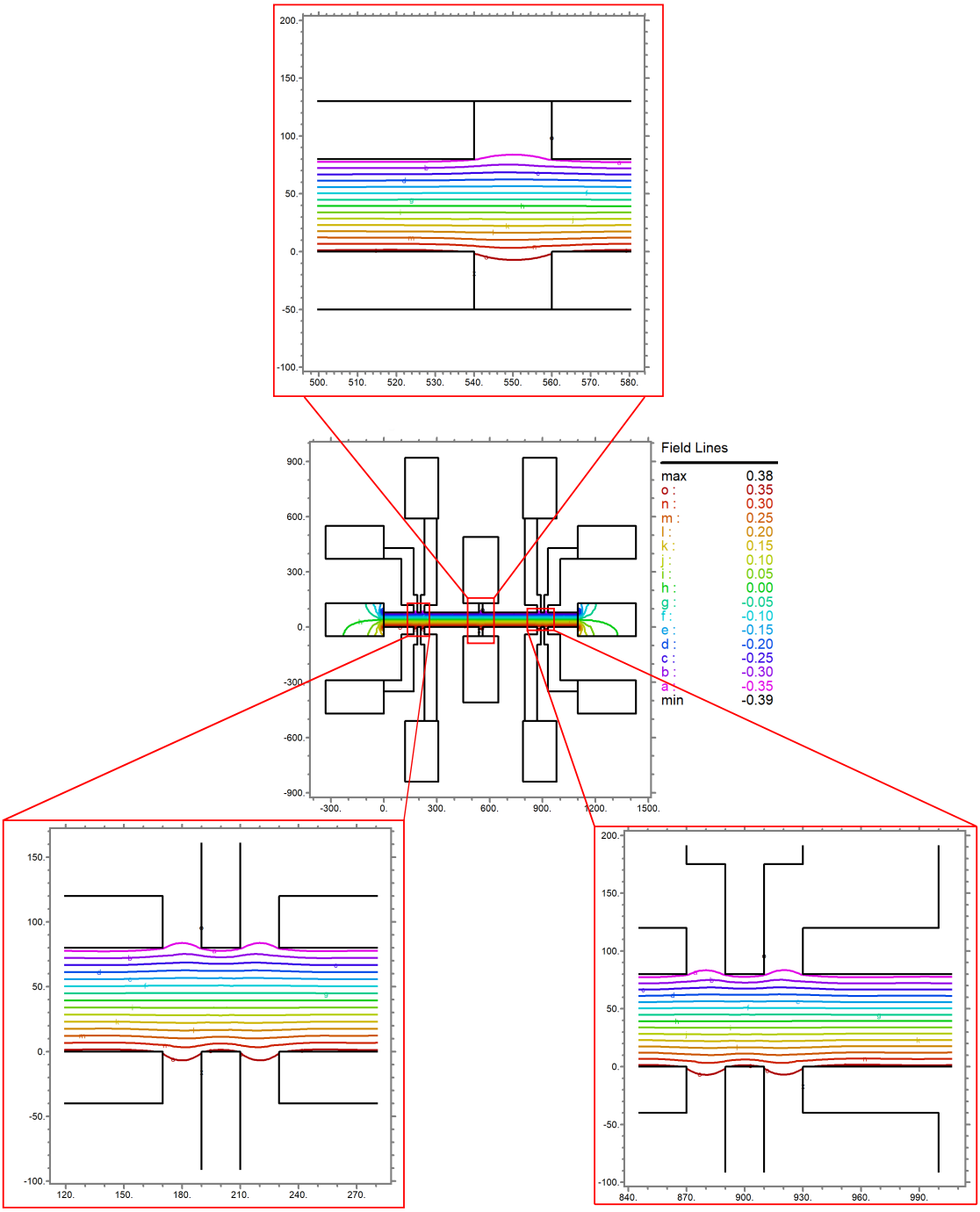

Figure 5.7: Simulation of a J9 Hall bar showing the current flow and close-ups near the different voltage probes along the J9 Hall bar. The simulation shows where the current is not confined by the channel boundary, the current bends into the voltage probe.

5.3.3 Simulation of the $4\,\mathrm{mm} \times 4\,\mathrm{mm}$ device

In this section simulations of the $4\,\mathrm{mm} \times 4\,\mathrm{mm}$ device are shown. The point is to calculate the resistance R between the different contacts, which will help to understand R for large small and contacts.

The device was designed for cooling electrons by having a low contact resistance R_C and 2DEG resistance R_{2DEG}. The contacts have large contact width and large area to minimise R_C to the 2DEG and to reduce R_{2DEG}, the 2DEG is $4\,\mathrm{mm} \times 2\,\mathrm{mm}$. Experimentally, the device has demonstrated an electron temperature T_e = $1\,\mathrm{mK}$ [79], with a heat leak to the 2DEG in the fW range.

Simulation of a $4\,\mathrm{mm} \times 4\,\mathrm{mm}$ device when a current is passed between I^+ and I^-

In the simulation a current flows between the two larger I^+ and I^- contacts, see Fig. 5.8. For calculation purposes, $R_\square = 1\Omega/\square$ therefore, the theoretical resistance for $R^{I^+I^-}$ is calculated as,

$$R^{I^+I^-} = 2R_C + R_\square \times (L/W). \tag{5.20}$$

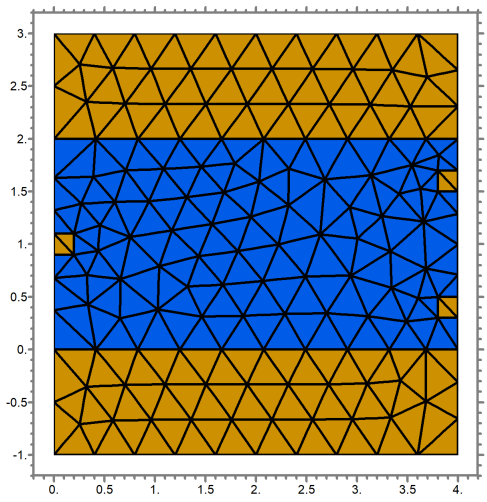

Figure 5.8: Simulation mesh-map of a $4\,\mathrm{mm} \times 4\,\mathrm{mm}$ device, the mesa is blue and the contacts are yellow. The 2DEG has dimensions width $W = 4\,\mathrm{mm}$ and length $L = 2\,\mathrm{mm}$. To calculate the resistance $R^{I^+I^-} = 2R_C + R_\square \times (L/W) = 2R_C + 1 \times 0.5$.

Figure 5.9(a) shows the isopotentials between the contacts is set to $10\,\mathrm{V}$ from the top I^+ contact, when the potential is half way across the device 50% of the initial pd value is dropped and the potential bends around the $200\,\mu\mathrm{m} \times 200\,\mu\mathrm{m}$ contacts.

The current in Fig. 5.9(b) flows from I^+ to I^- and bends into the contacts with greater density along the edge facing the centre of the 2DEG. The resistance calculated from the simulation is $R = (V/I) = (10/20) = 0.5\Omega$ and combining this with the real values for $R_\square$, the resistance $R^{I^+I^-} = 2R_C + 8 \times 0.5$. In [86] the experimental resistance with the same $R_\square$, measured between I^+ and I^- when $T = 1\,\mathrm{K}$ is $5.95\,\Omega$. To find R_C, the value of $5.95\,\Omega$ is combined with the simulated results as

$$5.95\,\Omega = 2R_C + 8 \times 0.5, \tag{5.21}$$

which rearranged gives,

$$R_C = (5.95 - 4)/2 = 0.975\,\Omega. \tag{5.22}$$

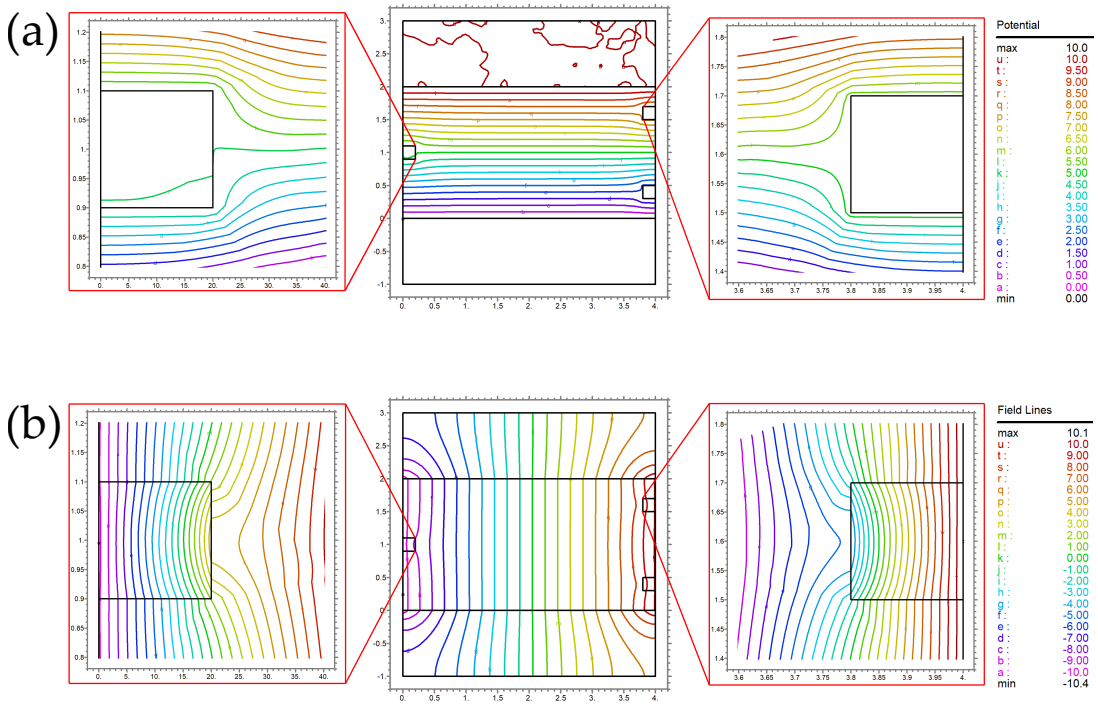

Figure 5.9: Simulation of a $4\,\mathrm{mm} \times 4\,\mathrm{mm}$ when a current is passed between the I^+ and I^- contacts. (a) A iso potential of $10\,\mathrm{V}$ is set from I^+ and drops by 50% when half way across the device. The close-ups show the pd bends around the smaller contacts. (b) The simulated current flows uniformly across the device and bends into the smaller contacts with greater density along the edge of the contact. From these simulations, the calculated resistance is $R = (V/I) = (10/20) = 0.5\,\Omega$.

Simulation of a $4\,\mathrm{mm} \times 4\,\mathrm{mm}$ device when a current is passed between V^+ and V^-

This section shows the simulated resistance $R^{V^+V^-}$ between the $200\,\mu\mathrm{m} \times 200\,\mu\mathrm{m}$ V^+ and V^- contacts, the contact resistance for these contacts are typically $R_C \approx 3\Omega$. When a current is passed between the contacts and $R_\square = 1\Omega/\square$, then the resistance $R^{V^+V^-}$ is,

$$R^{V^+V^-} = 2R_C + (1.2/4) \times R_\square = 2R_C + (0.3) \times 1 = 2R_C + 0.3\,\Omega. \tag{5.23}$$

The aim of this section is to understand the 2DEG resistance between the $200\,\mu\mathrm{m} \times 200\,\mu\mathrm{m}$ V^+ and V^- contacts.

Figure 5.10(a) shows the simulation of the iso potential where V^- is set to $10\,\mathrm{V}$ and 50% is dropped halfway between V^+ and V^-. The greatest current density is between V^+ and V^-, but the current does not flow directly between these contacts, it flows around the device and bends in toward NT, see Fig. 5.10(b). The resistance calculated from the simulation is $R = (V/I) = 2.9/10 = 0.29\,\Omega$ and when combined with $R_\square$, the resistance $R^{V^+V^-} = 2R_C + 1 \times 0.29 = 2R_C + 0.29\,\Omega$. Ref.[86] quotes the experimental R_C of a $200\,\mu\mathrm{m} \times 200\,\mu\mathrm{m}$ contact as $2\,\Omega$-$3\,\Omega$, by plugging this value back into the total resistance $R^{V^+V^-} = 2R_C + 1 \times 0.29 = 5 + 0.29\Omega \pm 1$.

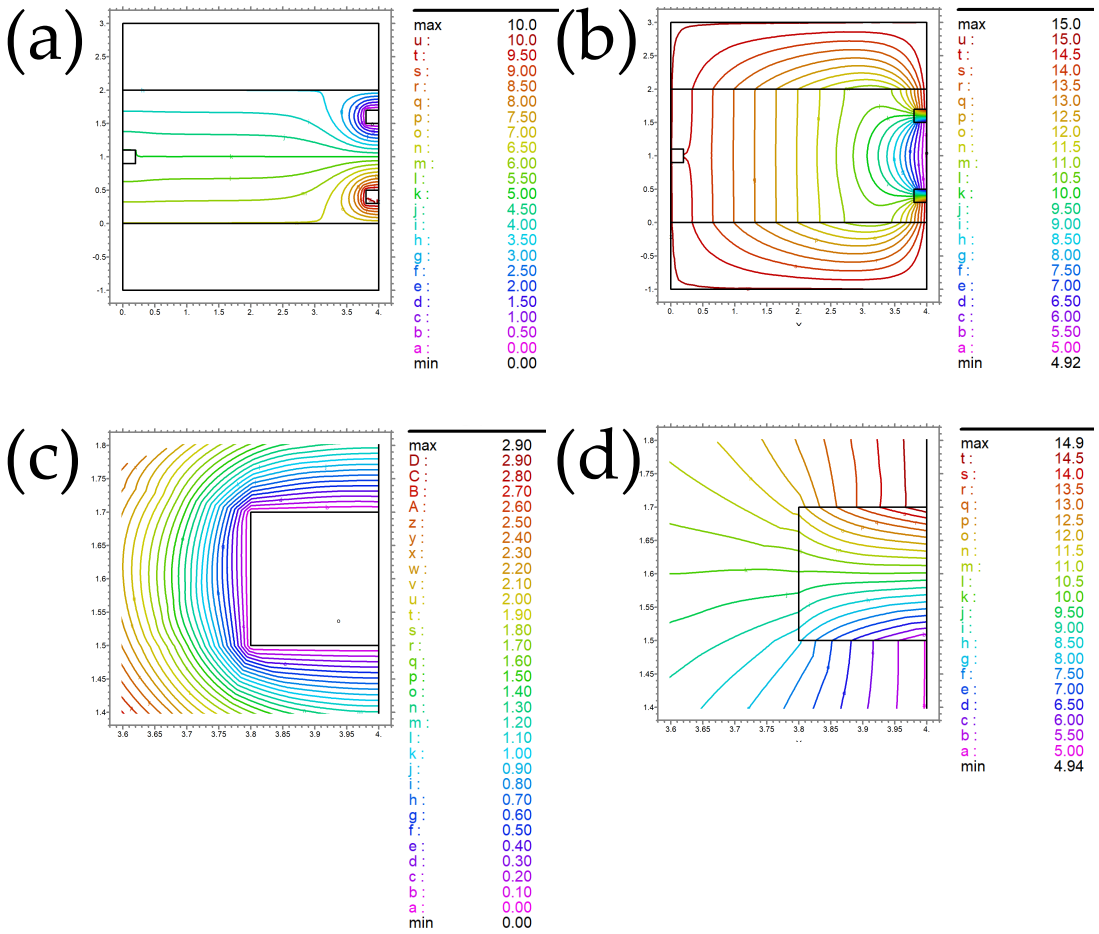

Figure 5.10: Simulation of a $4\,\mathrm{mm} \times 4\,\mathrm{mm}$ when a current is passed between the V^+ and V^- contacts. (a) The isopotential of $10\,\mathrm{V}$ is set from V^- and the potential map between V^+ and V^- shows that half of the potential is dropped halfway across the distance between the active contacts. (b) Some of the simulated current flows around the device, but the highest density is in between V^+ and V^-, which is the shortest current path. The current also bends near NT. (c) The potential bends around the V^+ contact. (d) The current sinks into V^+. By multiplying the simulated resistance of 0.29 together with $R_\square = 1\,\Omega$, the calculated resistance is $R_T = 2R_C + 0.29\,\Omega$.

Simulation of a $4\,\mathrm{mm} \times 4\,\mathrm{mm}$ device when a current is passed between I^+, V^+ and I^+,V^-

This section shows the simulated resistances when a current is passed between V^+ and I^+ noted as $R^{V^+I^+}$ and V^- and I^+ noted as $R^{V^-I^+}$.

If a current flows between either the V^+ and V^- contacts and I^+ the isopotential and current density will be different for each circuit, this is demonstrated in Fig. 5.10, where the potential for each circuit is set to $10\,\mathrm{V}$.

Figure 5.10(a) shows the isopotential between V^+ and I^+ where the highest potential is between these two contacts however, there is an 80% decrease in the pd at I^- and a 90% decrease near the NT contact. This can be compared to Fig. 5.10(b) where the simulation shows the isopotential between V^- and I^+. In this simulation, the isopotential is greatest nearer V^- and decreases along the device towards I^+, although 50% of the isopotential is dropped halfway along the device, it bends and can be picked up on I^-.

The current flow between V^+ and I^+ shows the current density is greatest in the distance between these two contacts with minimum density in the rest of the device see Fig. 5.10(c). However, when the current is passed between V^- and I^+, the current flow evenly distributed across the device to I^+, causing the current along the 2DEG path to have a larger current density, see Fig. 5.10(d); the current density is greatest on the right-hand side of the device, showing the current is taking shortest route. In this set-up, there is a higher current density in the bulk of the 2DEG compared to Fig. 5.10(c).

From the simulation results and $R_\square \approx 1\Omega/\square$, when a current flows between V^+ and I^+ then the resistance,

$$R^{V^+I^+} = 1 \times 0.5 = 0.5\,\Omega \tag{5.24}$$

and when a current flows between V^- and I^+ the resistance is,

$$R^{V^-I^+} = 1 \times 0.76 = 0.76\,\Omega. \tag{5.25}$$

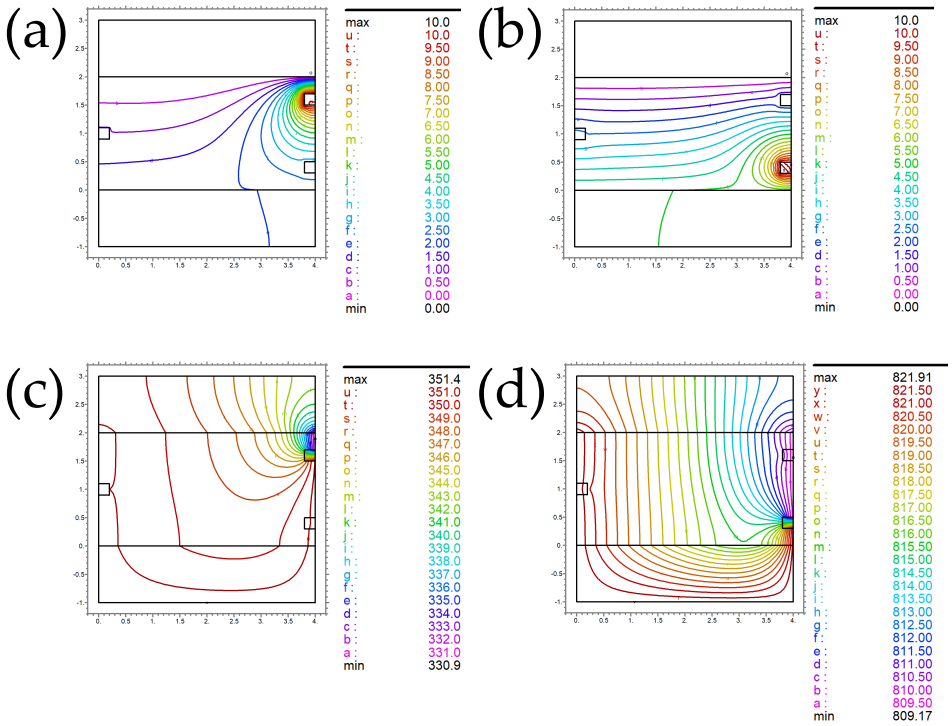

Figure 5.11: Simulation of a $4\,\mathrm{mm} \times 4\,\mathrm{mm}$ when a current is passed between V^+ and I^+ noted as $R^{V^+I^+}$ and V^- and I^+ noted as $R^{V^-I^+}$. (a) The isopotential is greatest between V^+ and I^+, but 20% of the potential can be picked up on I^-. (b) The isopotential between V^- and I^+ shows the potential is dropped along the device toward I^+, but 50% can be picked up on I^-. (c) When a current flows between V^+ and I^+ then the resistance, $R^{V^+I^+} = 1{\times}0.5$, where $R_\square = 1\Omega/\square$. The current density between V^+ and I^+ is greatest in the region between these two contacts, while the rest of the device has minimum density. (d) When a current flows between V^- and I^+ the resistance is, $R^{V^-I^+} = 1 \times 0.76$. The current between V^- and I^+ generally flows uniformly across the device, with the highest current density in the region between V^- and I^+.

Simulation of a $4\,\mathrm{mm} \times 4\,\mathrm{mm}$ device when a current is passed between I^+, I^- and NT and V^+, V^- and NT

Presented in this section are simulations showing the isopotential and current flow and therefore, the resistance between NT and I^+, I^- and NT and V^+, V^-.

Figure 5.12(a) shows the isopotential when a current is passed between NT and I^+, I^-. The potential is maximum value on both the larger contacts and bends around the NT symmetrically. The current flow between the larger contacts and NT has an asymmetric shape from the perspective of the centre of NT and the surrounding region has the highest current density, see Fig. 5.12(c). From these simulation results and $R_\square \approx 1\Omega/\square$ the resistance $R^{NTI^-I^+}$ is calculated as,

$$R^{NTI^-I^+} = 1 \times 0.64\Omega. \tag{5.26}$$

This can be compared to Fig. 5.12(b) where a current is passed between NT and I^+. In this set-up, 30% of the isopotential from I^+ drops across the bulk of the 2DEG before bending around NT. Figure 5.12(d) shows some of the current flowing around the device, eventually flowing into NT. In the region between I^+ and NT, there is a higher current density in this region because the current has taken the shortest path. From the results for this set-up, the resistance R^{NTI^+} is calculated as,

$$R^{NTI^+} = 1 \times 0.75\Omega. \tag{5.27}$$

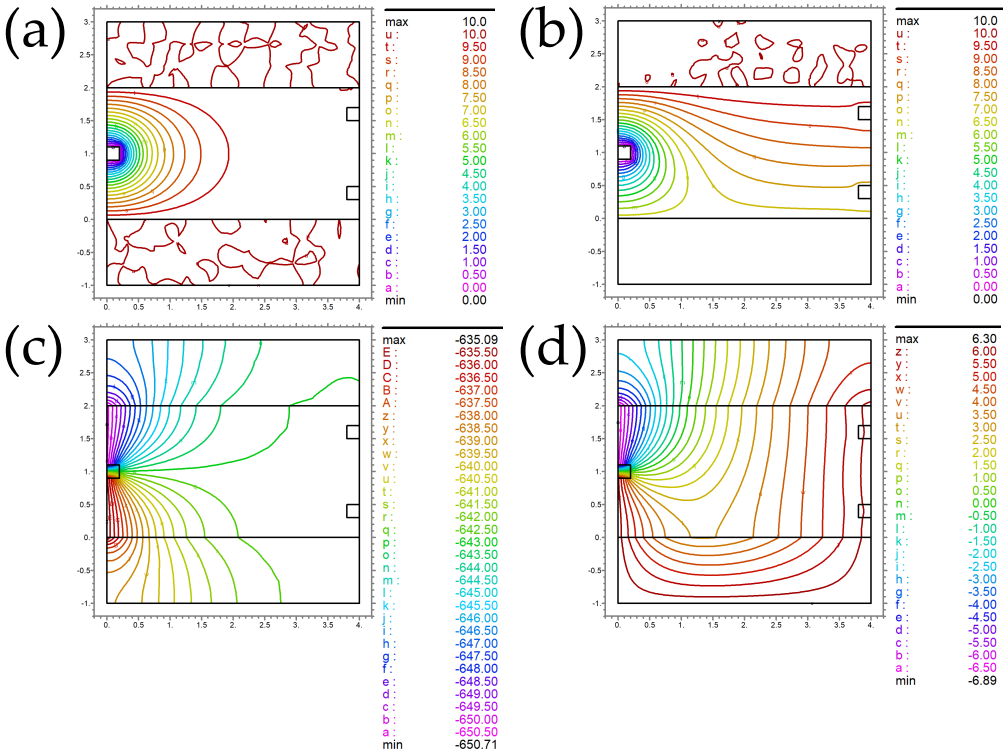

Figure 5.12: Simulation of a $4\,\mathrm{mm} \times 4\,\mathrm{mm}$ when a current is passed between NT and I^+, I^- and NT and I^+. (a) When the current is passed between NT and I^+, I^-, the potential lines bend around NT symmetrically. (b) When the current is passed between NT and I^+, the potential drops by 30% across the bulk of the 2DEG before bending around NT. (c) The current flow between NT and I^+, I^- is asymmetric when viewed from the centre of NT and the surrounding region has a high current density. The resistance $R^{NTI^-I^+} = 1{\times}0.64\Omega$, where $R_\square = 1\Omega/\square$. (d) When the current flows between I^+ and NT, some of the current bends around the bulk of the device and flows into NT from all sides, but the region of 2DEG with the highest current density is between I^+ and NT where the current takes the shortest path. The resistance $R^{NTI^+} = 1 \times 0.75\Omega$.

If the current source is passed between V^+, V^- and NT, 20% of the potential is dropped around V^+ and V^- and the remaining 70% is dropped around NT, see Fig. 5.13(a). Figure 5.13(b) shows the highest current density is in the regions around the contacts and the current from V^+, V^- bends towards the $4\,\mathrm{mm} \times 1\,\mathrm{mm}$ contacts before flowing into NT. In this configuration, the resistance $R^{NTV^+V^-}$ is calculated as,

$$R^{NTV^+V^-} = 1 \times 0.88\Omega. \tag{5.28}$$

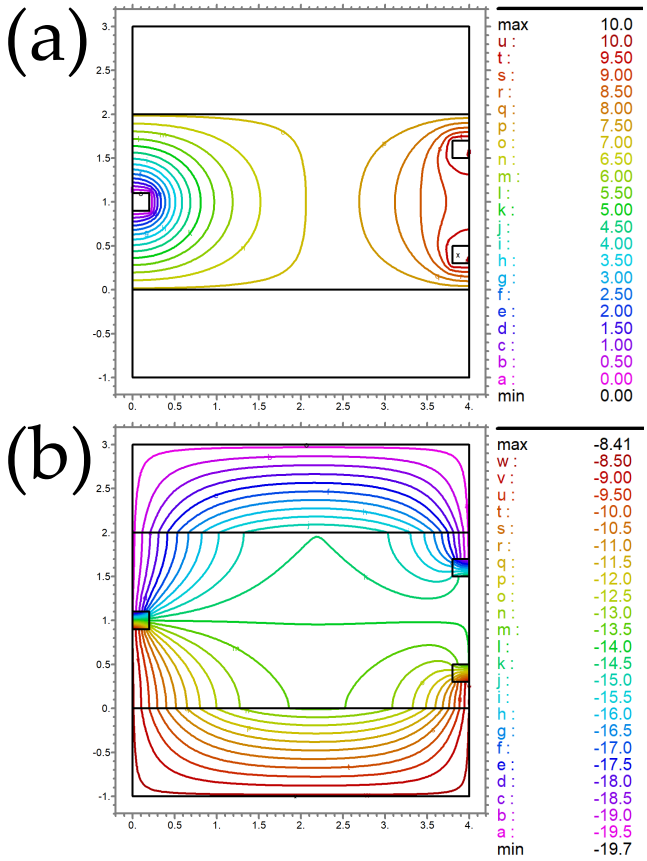

Figure 5.13: Simulation of a $4\,\mathrm{mm} \times 4\,\mathrm{mm}$ when a current is passed between NT and V^+, V^-. (a) 20% of the potential is dropped in the region around V^+ and V^- and then bends around NT. (b) The current bends into I^+ from V^+ and I^- from V^- before flowing into NT. The regions with the highest current density are between V^+ and I^+, V^- and I^- and around NT. In this set-up the resistance $R^{NTV^+V^-} = 1 \times 0.88\Omega$.

5.4 Summary

The whole aim of these simulations was to understand more clearly, the experimental values of R_C, which depend on whether it is a current ($4\,\mathrm{mm} \times 1\,\mathrm{mm}$) Ohmic contact or voltage ($200\,\mu\mathrm{m} \times 200\,\mu\mathrm{m}$) Ohmic contact and in what geometry it is being measured.

To achieve the lowest electron temperature, the original motivation to do the research, requires strong thermal coupling achieved by minimising the contact resistance R_C and the 2DEG resistance R_{2DEG}. The $4\,\mathrm{mm} \times 4\,\mathrm{mm}$ device simulated in this chapter is designed to minimise R_C with large area and perimeter and R_{2DEG} with small L/W. From the thermal model initially discussed at the beginning of this chapter, the highest temperature T_{max} is in the middle between two contacts and therefore, to achieve a low electron temperature the resistance between two contacts needs to be minimised; factors which contribute to this resistance are the resistance per square of the 2DEG $R_\square$, the geometry $L/W = N$ and the contact resistance R_C.

The results show that to achieve a low total resistance, the current should by passed between the $4\,\mathrm{mm} \times 1\,\mathrm{mm}$ contacts, where the $L/W = N = 0.5$ and $R_C \approx 0.8\,\Omega$ at $T = 1\,\mathrm{K}$, taken from Ref.[86]; in this set-up all the current flows from I^+ directly across the 2DEG to I^-. Although $N = 0.3$ when the current flows between V^+ and V^-, experimentally $R_C = 2\,\Omega$- $R_C \approx 3\,\Omega$ for $200\,\mu\mathrm{m} \times 200\,\mu\mathrm{m}$ contacts, see Ref.[86], so R_C is not minimised.

The simulations show that in all cases, $N < 1$ so when calculating the sample resistance $R = 2R_C + \frac{R_\square L}{W} = 2R_C + R_\square \times \frac{L}{W} = 2R_C + R_\square N = 2R_C + R_{2DEG}$, it can be seen that R_{2DEG} has been minimised and so the 2DEG can be cooled. The resistances for the simulations are summarised in Table 5.1.

Table 5.1: Summary of sample resistances for different geometries

Configuration	Resistance
I^+ to I^-	$0.5\,\Omega/\square$
V^+ to V^-	$0.3\,\Omega/\square$
I^+ to V^-	$0.76\,\Omega/\square$
I^+ to V^+	$0.5\,\Omega/\square$
I^+ to NT	$0.75\,\Omega/\square$
I^+,I^- to NT	$0.64\,\Omega/\square$
V^+,V^- to NT	$0.88\,\Omega/\square$

The table shows the sample resistance for different geometries, calculated when current is passed between different contacts of a $4\,\mathrm{mm} \times 4\,\mathrm{mm}$ device. The resistance is calculated by $R = R_\square \times \frac{L}{W}$, where and $R_\square = 1$, because $N < 1$ in all cases, the 2DEG resistance R_{2DEG} is minimised so can be cooled. This table shows, according to the simulations, which 2DEG resistance will be the lowest. From the table the lowest resistances are I^+ to I^- and V^+ to V^-. The R_C between I^+ to I^- is less the $1\,\Omega$ and the R_C between V^+ to V^- is between $2\,\Omega$ - $3\,\Omega$. Therefore, to achieve the lowest electron temperature, the original motivation to do the research, requires strong thermal coupling achieved by minimising R_C and R_{2DEG}. Therefore, to achieve a low electron temperature the resistance between I^+ to I^- needs to be minimised.

Chapter 6

Evidence of superconductivity in AuGeNi Ohmic contacts

6.1 Introduction

This chapter presents contact resistance R_C measurements that reveal the superconductivity in AuNiGe contacts. Further evidence is provided by top resistance R_{top} and vertical R_V measurements. These equilibrium transport measurements use small excitation currents $I = 0.1\,\mu\text{A} - 1\,\mu\text{A}$, and are measured in a magnetic field applied either perpendicular or parallel to the plane of the 2DEG.

6.2 Contact resistance R_C

6.2.1 Motivation

To measure the 2DEG resistance R_{2DEG} the current must flow from the top of the Ohmic contact to the edge of the 2DEG, this is the contact resistance R_C. The original motivation for the research was to be able to cool the electrons in a 2DEG, however to achieve this the R_{2DEG} and R_C need to be reduced. In Chapter 5, the 2DEG resistance of a $4\,\mathrm{mm} \times 4\,\mathrm{mm}$ device was simulated to be minimal, however simulations of the contact resistance were not done; in this section, measurements for R_C of a $4\,\mathrm{mm} \times 4\,\mathrm{mm}$ device are made. The sample has a $L/W = 0.5$ ratio and the large $4\,\mathrm{mm} \times 1\,\mathrm{mm}$ contacts are designed to have low resistance, so the contact resistance can be measured and understood for the thermal model.

6.2.2 R_C Measurement circuits

The contact resistance R_C is made up of contributions from the resistance under the Ohmic contact and the vertical resistance R_V. When a current flows between two contacts the two-terminal resistance $R_{2T} = V_{2T}/I$, has contributions from the 2DEG resistance R_{2DEG} and R_C for each contact so that:

$$R_{2T} = 2R_C + R_{2DEG}, \tag{6.1}$$

where it is assumed that the R_C for each contact is equal.

Therefore, to determine R_C, see Fig. 6.1 requires a measurement of R_{2DEG} which comes from a four-terminal measurement of the four-terminal resistance

$$R_{4T} = \frac{V_{4T}}{I} = \frac{1.2}{4} \times R_{\square} = 0.3 \times R_{\square}. \tag{6.2}$$

The 2DEG of length $2\,\mathrm{mm}$ and width $4\,\mathrm{mm}$ measured between I^+ and I^- has the two-terminal resistance

$$R_{2T} = 2R_C^I + R_{2DEG} = 2R_C^I + \frac{2}{4} \times R_{\square} = 2R_C^I + \frac{5}{3} \times R_{4T}, \tag{6.3}$$

where R_C^I is given by,

$$R_C^I = \frac{1}{2}(R_{2T} - \frac{5}{3}R_{4T}) = \frac{2R_{2T}}{2} - \frac{5}{6}R_{4T}. \tag{6.4}$$

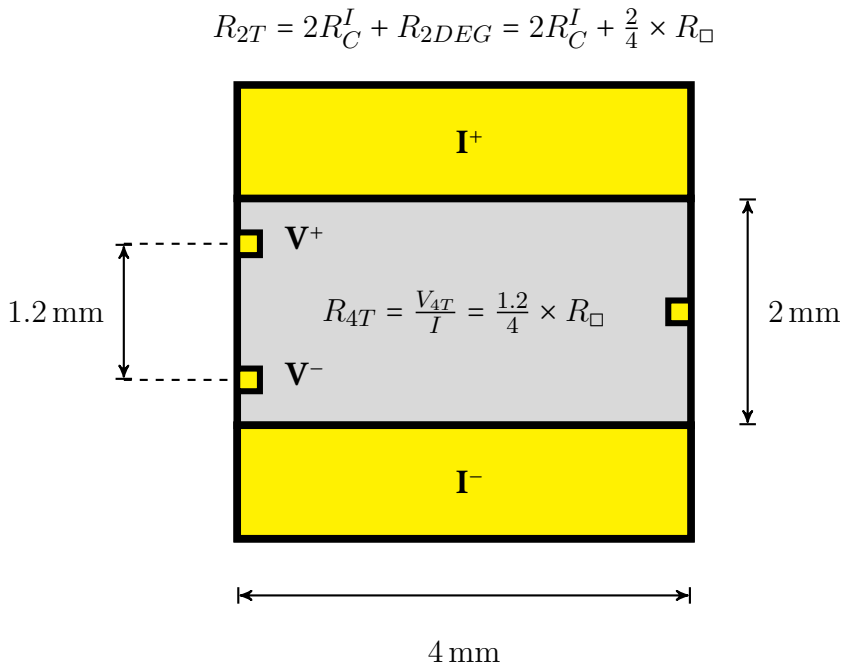

Figure 6.1: Schematic of a $4\,\mathrm{mm} \times 4\,\mathrm{mm}$ device showing that to measure R_C, requires a measurement of R_{2DEG}, this comes from the four-terminal resistance see Eq.6.2. The 2DEG of length $2\,\mathrm{mm}$ and width $4\,\mathrm{mm}$ measured between I^+ and I^- has the two-terminal resistance, see Eq.6.3.

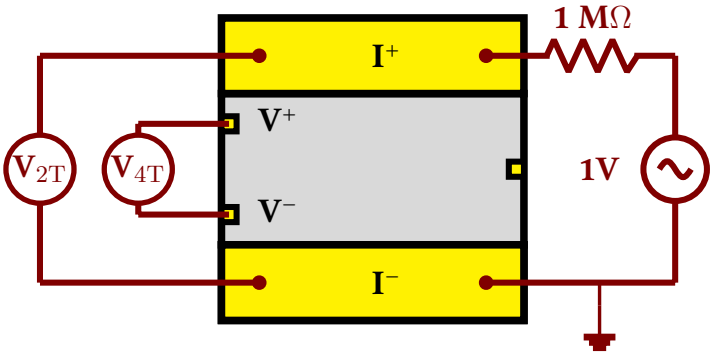

Figure 6.2: Four-terminal and two-terminal measurements of a $4\,\mathrm{mm} \times 4\,\mathrm{mm}$ device. The four-terminal resistance of the 2DEG between V^+ and V^- is given by $R_{4T} = V_{4T}/I$, when an AC current $I = 1\,\mu\mathrm{A}$ is passed between I^+ and $I-$. The corresponding $2T$ resistance between I^+ and I^- is $R_{2T} = V_{2T}/I$. If the contact resistances R_C to I^+ and I^- are equal, then the $2T$ resistance of a 2DEG of length $2\,\mathrm{mm}$ and width $4\,\mathrm{mm}$ is Eq.6.3. Figure originally shown in Ref. [86].

To measure R_C^V defined as,

$$R_C^V = \frac{1}{2}R_{2T}^V - \frac{1.2}{4} \times R_{\square}. \tag{6.5}$$

The set-up shown in Fig. 6.3 is used; in this circuit a $1\,\mu A$ AC current is driven between V^+ and V^- and the voltage V_{2T}^V measured between V^+ and V^- is the resistance.

Reciprocity theorem says that, $R_{mn,kl} = R_{kl,mn}$ that is, swapping current and voltage leads only works in $B = 0$. So by swapping between Fig. 6.2 and Fig. 6.3, the measured R_{4T} should be the same, then by comparing each R_{2T} the effect of the contact resistance is observed.

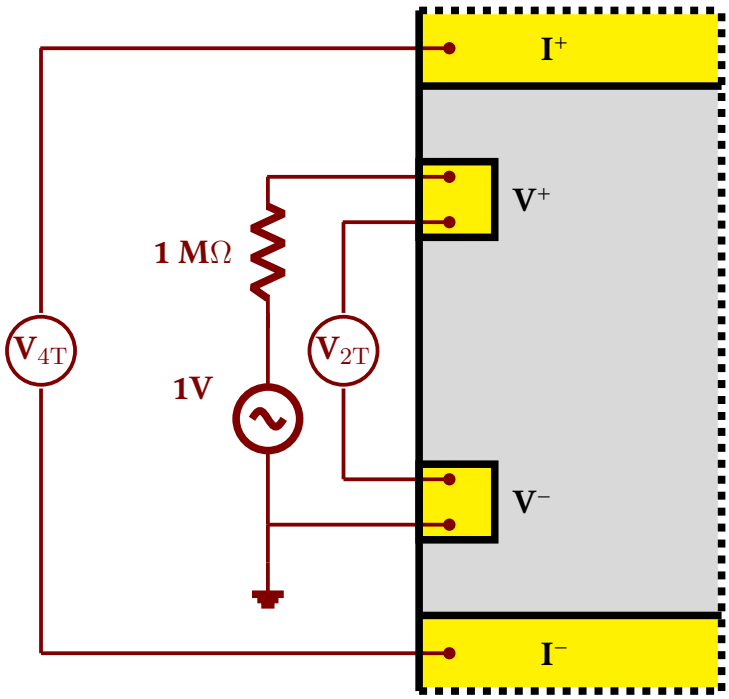

Figure 6.3: Measurement circuit of a $4\,\mathrm{mm} \times 4\,\mathrm{mm}$ device to determine the contact resistance of a voltage probe R_C^V. The four-terminal resistance is given by $R_{4T} = V_{4T}/I$, when an AC current $I = 1\,\mu A$ is passed between the V^+ and V^- contacts. The corresponding $2T$ resistance is $R_{2T}^V = 2R_C^V + \frac{1.2}{4} \times R_{\square}$. If the contact resistances R_C to V^+ and V^- are equal, then the $2T$ resistance is $R_C^V = \frac{1}{2}R_{2T}^V - \frac{1.2}{4}R_{\square}$, where 4 and 1.2 come from sample dimensions.

6.2.3 Results

In 2D systems, ρ and R of a sample have the same units (Ω) and are related via the dimensionless quantity L/W. In traditional Hall bar devices the longitudinal resistance R_{xx} is given by,

$$R_{xx} = \frac{V}{I} \tag{6.6}$$

and the transverse (Hall) resistance $R_{xy}(R_H)$ is expressed as,

$$R_{xy} = \frac{V_H}{I}, \tag{6.7}$$

where V_H is the measured Hall voltage. However, the $4\,\mathrm{mm} \times 4\,\mathrm{mm}$ device, which is short and wide is not a traditional Hall bar and the voltages measured across the sample produce a mixed signal made up of R_{xx} and R_{xy}, see Fig. 6.4(a) where the Hall effect is used to measure the carrier density n_{2D} of Sample A after illumination.

In both Sample A and Ref.[87], the current contacts span the whole width of the sample shorting the Hall voltage between them; even at low fields it is much larger than the voltage across R_{xx}. The effect this sample geometry has on this resistance is illustrated in Fig. 6.4(a) using theory in Ref.[88] by,

$$R_{2T}(B) = c\sqrt{R_{xx}^2 + R_{xy}^2}, \tag{6.8}$$

where c is of the order unity and the Hall resistance R_{xy} is,

$$R_{xy} = \frac{B}{n_{2D}e}. \tag{6.9}$$

As B increases, $R_{xy} \gg R_{xx}$, $c \to 1$ and $R_{2T} \to R_{xy}$. Therefore, to find the values of R_{xx}, if $c = 1$ then Eq. 6.8 can be rearranged as follows

$$R_{xx} = \sqrt{R_{2T}^2 - R_{xy}^2}. \tag{6.10}$$

Figure 6.4(a) shows $R_{2T}-R_{xy}$ plotted in red, where R_{2T} is the raw data and the resistance R_{xy} is labelled as R_H; Fig. 6.4(a) shows a linear Hall slope R_H is drawn, starting from zero, through the centre of the data. $R_{2T}(B)$ measurements show the linear $R_{2T}(B)$ has a gradient of $2050\,\Omega T^{-1}$, corresponding to $n_{2D} = 3.04\times10^{11}$ cm^{-2}, this is consistent with $n_{2D} = 2.94\times10^{11}$ cm^{-2} taken from the indexed Shubnikov de-Haas oscillations; using $n_{2D} = 3.04\times10^{11}$ cm^{-2} for Eq.6.9, R_{xy}^2 is shown in black. When $B < 0.1\,\mathrm{T}$ the Shubnikov-de Haas oscillations in R_{xx} become visible and the Landau level filling factors are indexed for $\nu = 50$ and 60.

The Landau level quantisation producing R_{xx} is periodic in $1/B$, these are the Shubnikov de-Haas oscillations, see Fig. 6.4(b). The resistance R_{xx} is periodic in $1/B$, the period being given by:

$$\Delta\left(\frac{1}{B}\right) = \frac{g_s e}{h n_{2D}} \tag{6.11}$$

where $g_s = 2$.

When $B = 0\,\mathrm{T}$, $R_{2T} \approx 5\,\Omega$, but with increasing B-field a linear magnetoresistance due to the Hall effect dominates as observed in $R_{2T}(B)$ measurements of graphene[87], where geometry effects the conductance of two-terminal devices in the quantum Hall regime and the quantum Hall plateaus exhibit conductance extrema that are stronger for wide and short samples. In Ref.[87], the authors systematically examine two-terminal conductance in the quantum Hall regime for a variety of sample aspect ratios and find that features depend on the sample aspect ratio, concluding while a two-terminal measurement is not as straightforward to interpret as the corresponding four-terminal measurement, it is simple to perform; the presence of non-zero longitudinal resistance causes quantum Hall plateaus measured in a two-terminal configuration to not be as quantised compared to the four-terminal measurement.

Figure 6.4(c) shows the $R_{2T}(T)$ in a B field; the traces at finite B field are vertically offset to align the resistances at $5.95\,\Omega$ for $T > 0.8K$; shifting down the sweeps removes the magnetoresistance of the 2DEG. When $B = 0\,\mathrm{T}$ there is a $1.2\,\Omega$ drop in resistance below $0.8\,\mathrm{K}$ and the 2DEG resistance at zero field $R_{2DEG}(T) = 4.32\,\Omega$; the R_C^I calculated in zero field, shows that $R_C^I = 0.8\,\Omega$ when $T = 1\,\mathrm{K}$, dropping to $R_C^I = 0.2\,\Omega$ when $T = 1\,\mathrm{K}$ at low temperatures.

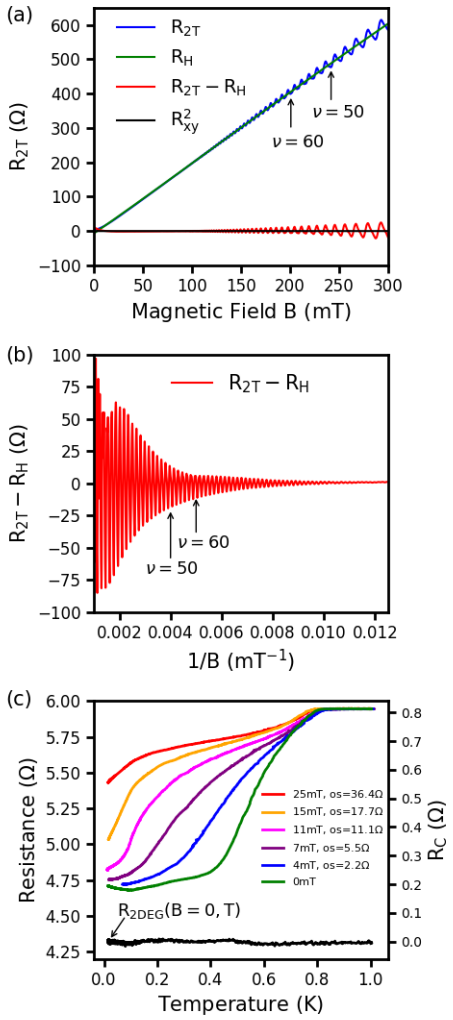

Figure 6.4: (a) Two-terminal resistance $R_{2T}(B)$ measurements of Sample A when $T = 0.3\,\mathrm{K}$ and $B < 0.3\,\mathrm{T}$. R_{2T} is the raw data measured which can be expressed by $R_{2T}(B) = c\sqrt{R_{xx}^2 + R_{xy}^2}$, where c is of the order unit and R_{xy} is the Hall resistance (R_H), expressed as $R_{xy} = \frac{B}{n_{2D}e}$; the Hall resistance $R_H = 2050\,\Omega T^{-1}$ is the linear Hall slope starting from zero through the centre of the data. The red trace shows $R_{2T} - R_{xy}$. R_{2T} shows the linear gradient corresponds to $n_{2D} = 3.04\times10^{11}$ cm^{-2}, this is consistent with $n_{2D} = 2.9410^{11}$ cm^{-2} taken from the indexed SdH oscillations; using $n_{2D} = 3.04\times10^{11}$ cm^{-2} for Eqn. 6.9, R_{xy}^2 is shown in black. When $B < 0.1\,\mathrm{T}$ the Shubnikov-de Haas oscillations in R_{xx} become visible and the Landau level filling factors are indexed for $\nu = 50$ and 60. (b) To see if there are oscillations present in R_{xx}, we plot the trace $R_{2T} - R_{xy}$ as a function of 1/B. (c) $R_{2T}(T)$ in different $B_\perp$ fields. Traces of $R_{2T}(T)$ at $B = 0, 4, 7, 11, 15$, and $25\,\mathrm{mT}$; the sweeps at finite B have been shifted down by the given offsets (os) to remove the magnetoresistance of the 2DEG. The contact resistance $R_C^I = (R_{2T} - R_{2DEG})/2$, where $R_{2DEG}(T)$ at $B = 0$ is the trace shown in green.

Next, we will introduce Sample B, which was measured to find R_C^V of the voltage $200\,\mu\mathrm{m} \times 200\,\mu\mathrm{m}$ Ohmic contacts on the $4\,\mathrm{mm} \times 4\,\mathrm{mm}$ device. To observe the effect of a parallel magnetic field, Sample B was measured $B_\parallel$, using the set-up shown in Fig. 6.2, following illumination of the 2DEG until saturation. Figure 6.5 shows magnetoresistance results when $T = 0.1\,\mathrm{K}$; Fig. 6.5(a) shows the two-terminal $R_{2T}(B_\parallel)$ has a Hall slope R_H with a gradient of $75\,\Omega T^{-1}$, corresponding to $n_{2D} = 9.54 \times 10^{12}$ cm^{-2}. This is due to misalignment of B, on other words, the field is parallel to 2DEG so its $B_\perp$ that is important. Using the results we ascertain the misalignment $B_\perp = Bsin\theta$. $B_\perp$ is giving rise to Hall effect and some SdH due to n_{2D} so to calculate the angle of misalignment,

$$R_H = \frac{B_\perp}{ne} = 75\,\Omega T^{-1} \tag{6.12}$$

however, the wafer is known to be,

$$R_H = \frac{B}{ne} sin\theta = 1050\,\Omega T^{-1}. \tag{6.13}$$

$\Rightarrow \theta sin^{-1}(\frac{75}{1050}) = 4.09\,\mathrm{deg}$. So the n_{2D} does not change with angle, the measured value is a consequence of misalignment not a 2DEG with a high n_{2D}; B is giving rise to the Hall effect and some SdH due to n_{2D}. The interesting result is the other frequency detected in the fast Fourier transform (FFT), see Fig. 6.5(d), but that is beyond the scope of this thesis.

When removing the Hall slope the plot in Fig. 6.5(b) is produced, which shows oscillations forming when $B \approx 1\,\mathrm{T}$ and the trace itself has an oscillation of a peak-to-peak amplitude of $\pm 2\,\Omega$; if the data is shown as function of $1/B$, see Fig. 6.5(c), the oscillations are clearer. In order to discern the contributions involved in the oscillations, a fast Fourier transform (FFT) performed on the data confirms two narrow peaks at $2\,\mathrm{T}(f_a)$ and $30\,\mathrm{T}(f_b)$, where the slight oscillations in f_b are due to misalignment with B, but it is not clear where the oscillations for f_a originate, see Fig. 6.5(d).

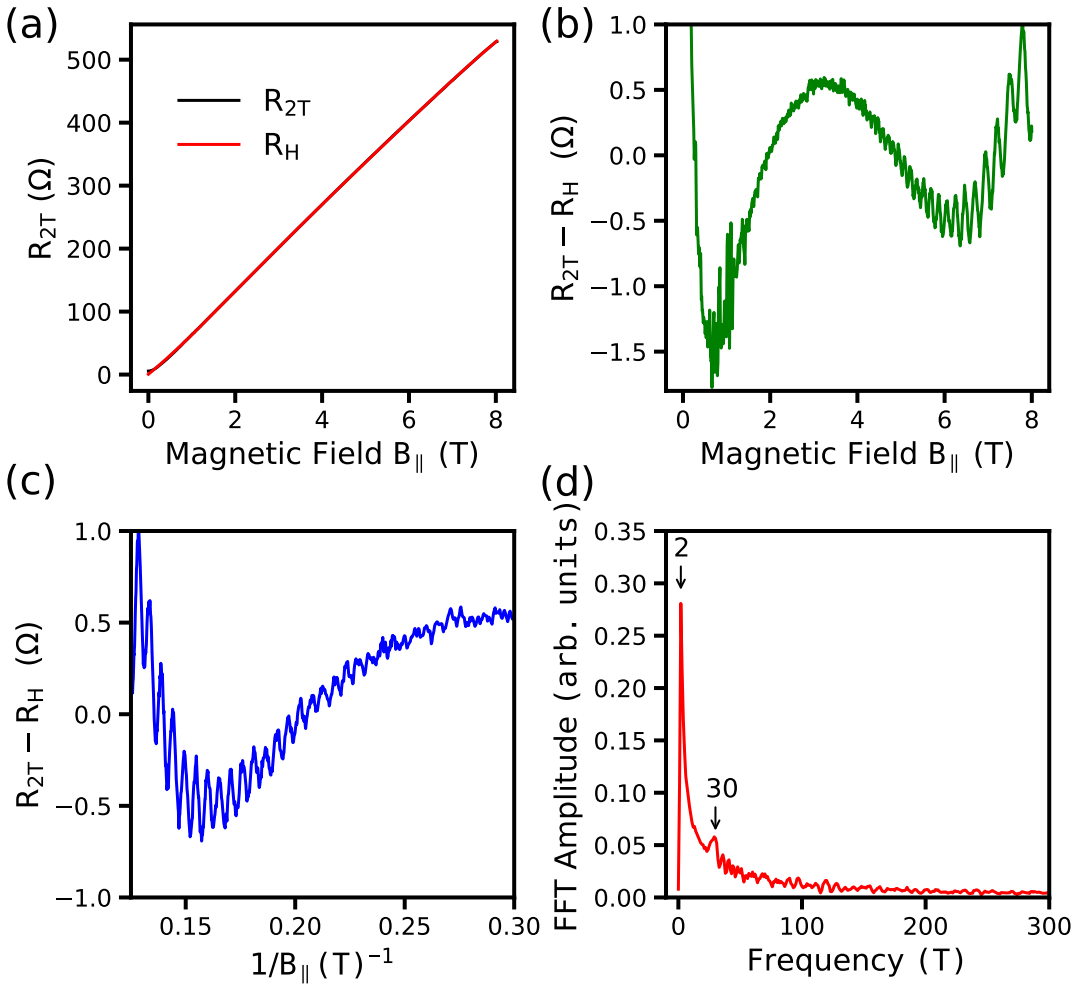

Figure 6.5: Magnetoresistance measurements of Sample B using the R_C^I circuit when $T = 0.1\,\mathrm{K}$. (a) The two-terminal resistance as a function of the parallel magnetic field $R_{2T}(B_\parallel)$. The linear Hall slope R_H has a gradient of $65\,\Omega T^{-1}$ corresponding to $n_{2D} = 9.54 \times 10^{12}$ cm^{-2} as a consequence of misalignment of $4.5\,\mathrm{deg}$, so the $n_{2D} = 9.54 \times 10^{12}$ cm^{-2} is a consequence of misalignment not a 2DEG with a high n_{2D}. (b) Removing R_H from the two-terminal data produces a plot indicating the presence of at least two oscillatory components. These small oscillations form when $B > 1\,\mathrm{T}$, which grow in amplitude as the magnetic field increases. The trace itself has an oscillation of a peak-to-peak amplitude of $\approx 1\,\Omega$ when $B > 1\,\mathrm{T}$. (c) Plotting the oscillation as a function of $1/B$. (d) Fourier transform of the data in (c) shows two main frequencies at $2\,\mathrm{T}(f_a)$ and $30\,\mathrm{T}(f_b)$.

The set-up shown in Fig. 6.3 to measure R_C^V is used in Fig. 6.6. This shows $R_{2T}(T)$ in different $B_\parallel$ fields for Sample B after flashing the 2DEG to saturation; in this configuration, the correction due to the magnetoresistance of the 2DEG is smaller compared to Sample A in $B_\perp$ because of misalignment. In the measurement, the superconductivity is suppressed with a parallel field of $B_\parallel = 202\,\mathrm{mT}$ and the traces at finite B field are also vertically offset to align the resistances at $8.25\,\Omega$ for $T > 0.8\,\mathrm{K}$; when $B = 0$ and $T = 1\,\mathrm{K}$, the contact resistance $R_C^V = \frac{1}{2}R_{2T}^V - \frac{1.2}{4} \times R_\square = 2.62\,\Omega$.

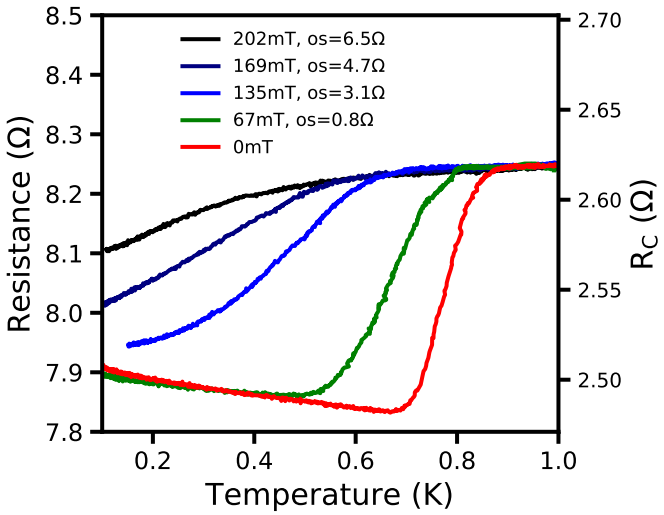

Figure 6.6: $R_{2T}(T)$ measurements of Sample B in different $B_\parallel$ fields using the R_C^V circuit after flashing the 2DEG to saturation. Traces of $R_{2T}(T)$ at $B = 0, 67, 135, 169$, and $202\,\mathrm{mT}$; the sweeps at finite B have been shifted down by the given offsets (os) to remove the magnetoresistance of the 2DEG. The contact resistance $R_C^V = \frac{1}{2}R_{2T}^V - \frac{1.2}{4} \times R_\square$ is the trace shown in red.

6.3 Vertical resistance R_V

A greater understanding of current-crowding and the modification of the 2DEG sheet resistance under the Ohmic contact is gained from vertical resistance measurement [55]; R_V measures the resistance of the alloy in the vertical direction. We show here the effect of the superconductivity on this resistance.

6.3.1 Motivation

For the purpose of this section, we can summarise the TLM model[51] and the Reeves model[55]. The TLM model measurements give the sheet resistance $R_\square$ and transfer length L_T from the x-intercept and the contact resistance R_C from the y-intercept; in the TLM model $R_\square = R_{sk}$ where R_{sk} is the 2DEG sheet resistance under the contact, and there are no ρ_C or vertical resistance R_V measurements. However, in the Reeves model, $R_\square \neq R_{sk}$ and by using R_C and R_V, L_T and ρ_C is obtained, as can the resistance underneath the contact. This can be explained because in the Reeves model if R_{sk} is modified, the correct value of ρ_C is found by measuring R_V. Therefore, the R_V measurement is fundamental in analysing Ohmic contacts. In the results presented, the R_V measurement is used to further understand superconductivity in the vertical direction of the Ohmic contact.

6.3.2 R_V Measurement circuit

Figure 6.7 shows the typical four-terminal R_V measurement circuit using a TLM sample. An AC current of $I = 0.01\,\mathrm{mA}$ was driven between the left-hand Ohmic contact and the centre contact and the vertical voltage V_V is measured between the centre and right-hand Ohmic contacts. The vertical resistance R_V is defined to be,

$$R_V = \frac{V_V}{I}. \tag{6.14}$$

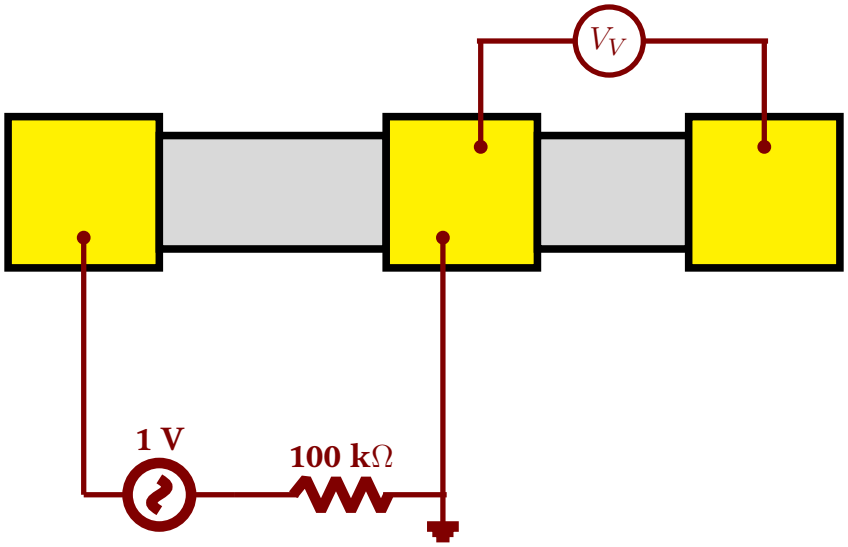

Figure 6.7: The vertical resistance R_V measurement circuit[55], on a TLM sample. With a current of $I = 0.01\,\mathrm{mA}$ driven between two adjacent contacts, the voltage V_V is measured between a second gold bond connection to the centre contact and the adjacent contact on the 'back' side. The resistance is $R_V = V_V/I$.

6.3.3 Results

Figure 6.8 shows $R_V(T)$ measurement of Sample F, see Table 3.2, in a magnetic field applied perpendicular to the plane. Sample F is a NTLM device, see Ref.[89], with a single 2DEG channel comprising of $\frac{1}{2}$, 1, 2, 4, 6, 8 and 10 square segments. The off-mesa voltage probes on either side of the on-mesa Ohmic contact allows the resistance of the 2DEG and Ohmic contact resistance parameters to be measured independently; the $200\,\mu\mathrm{m} \times 200\,\mu\mathrm{m}$ contacts are comparable to the V^+, V^- and NT contacts on the $4\,\mathrm{mm} \times 4\,\mathrm{mm}$ device.

Figure 6.8 shows traces of $R_V(T)$ at B = $0, 10, 15, 25$ and $150\,\mathrm{mT}$. When B = $0\,\mathrm{mT}$, the $R_V(T)$ shows ≈ $25\,\mathrm{m}\Omega$ drop in resistance below $0.8\,\mathrm{K}$; the superconducting transition is broad and $\Delta T_c \approx 0.5\,\mathrm{K}$, this transition is centred at T_c = $0.6\,\mathrm{K}$. The traces at finite B field are vertically offset to align the resistances at R_V = $25.5\,\mathrm{m}\Omega$ for $T > 0.8\,\mathrm{K}$.

From these results we observe that $R_V \ll R_C$ for a $200\,\mu\mathrm{m} \times 200\,\mu\mathrm{m}$ Ohmic contact where $R_C \approx 2\,\Omega - 3\,\Omega$ for $T > T_c$, see Fig. 6.6, and using the current crowding model[55], the transfer length $T_L \approx 40\,\mu\mathrm{m}$. It is also evident that R_V has a superconducting component that is suppressed at $150\,\mathrm{mT}$, a comparable field to the data shown in Fig. 6.6.

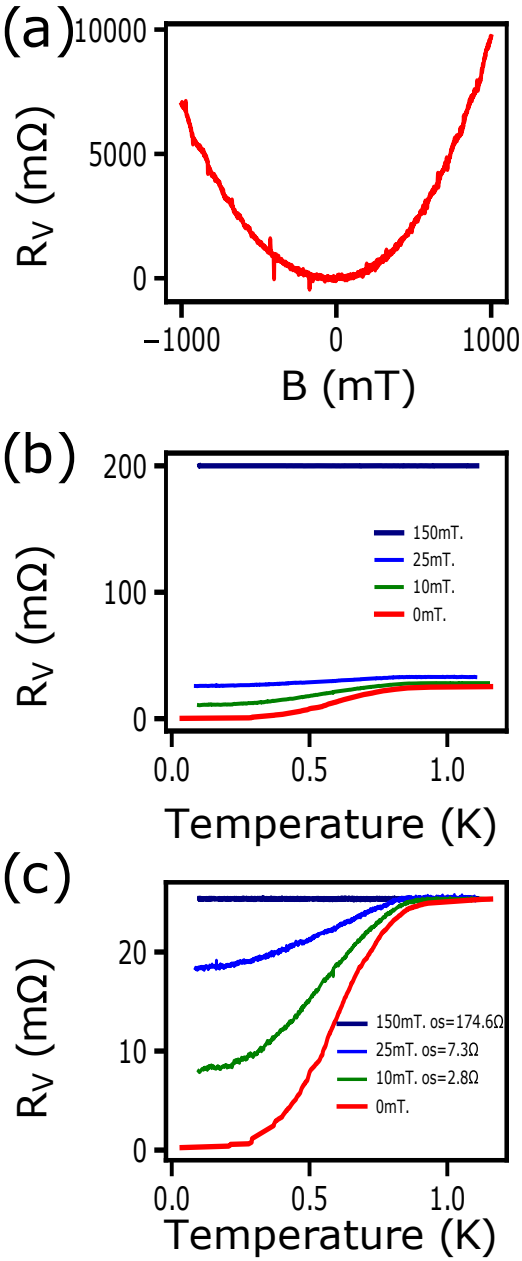

Figure 6.8: Vertical resistance $R_V(T)$ measurements of Sample F in different $B_\perp$ fields. (a) Vertical resistance $R_V(B)$ measurement of Sample F when $T = 0.1\,\mathrm{K}$. (b) The traces show raw $R_V(T)$ sweeps at $B = 0, 10, 15, 25$ and $150\,\mathrm{mT}$. (c) At $B = 0$, R_V shows a $\approx 25\,\mathrm{m\Omega}$ drop in resistance below $T = 0.8\,\mathrm{K}$. To remove the magnetoresistance, the traces at a finite B field are vertically offset to align the resistances at $25\,\mathrm{m\Omega}$ for $T > 0.8\,\mathrm{K}$. The drop in the resistance below $T = 0.8\,\mathrm{K}$ is due to the presence of a superconductor in the Ohmic contact. By increasing the $B_\perp$ field, the superconductivity is suppressed, decreasing the drop in R_V. ΔT_c is defined as the temperature difference, when $B = 0$, between the resistance when $T = 0.8\,\mathrm{K}$ and $R_V \approx 25\,\mathrm{m\Omega}$ and when $T \approx 0.3\,\mathrm{K}$ and $R_V \approx 0.1\,\mathrm{m\Omega}$.

Figure 6.10 shows the set-up and measurement of $R_V(T)$ for Sample G; this measurement is motivated by the idea that vertical current paths, and therefore, R_V depend upon the direction of the current flow. The experimental question is this: "When the current is driven between one side of the contact and then the other, what is the difference in the value for R_V?" If there is a difference, then there must be 'different ends' for vertical resistance, see Fig. 6.9, which are likely to be superconducting.

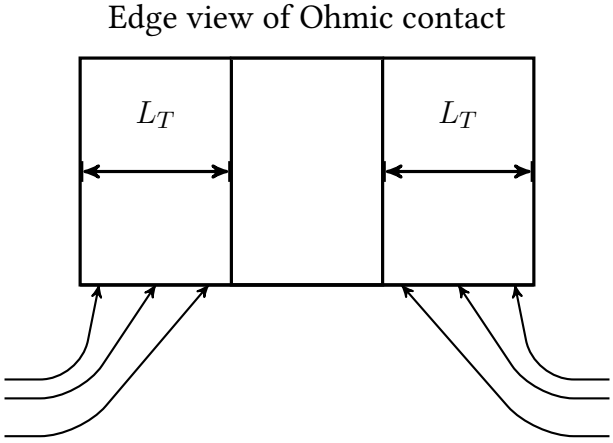

Figure 6.9: The schematic of the 'different ends' for vertical resistance shows the Ohmic contact has a transfer length L_T, the effective length needed for the current to transfer from the metal to semiconductor, for each side.

Sample G is a device designed for TLM measurements with Ohmic contact dimensions $60\,\mu\mathrm{m} \times 80\,\mu\mathrm{m}$ and bonding is on Au metal side pads connected to the contact; this device is the standard Cavendish laboratory TLM mask. In Fig. 6.10, the R_V of the same $60\,\mu\mathrm{m} \times 80\,\mu\mathrm{m}$ Ohmic contact is measured when the current flows in two different directions giving: R_{V1} and R_{V2} measurements; these are the vertical resistances of the contact measured from two different directions. Using the set-up in Fig. 6.10(a), R_{V1} is defined when the current $I = 0.01\,\mathrm{mA}$ is driven between the bottom two contacts and the voltage V_{V1} measured between the centre contact and the top contact measures $R_{V1} = V_{V1}/I$. However, if the current is driven between the top two contacts, the voltage V_{V2} measured between the centre contact and the bottom contact measures $R_{V2} = V_{V2}/I$, see Fig. 6.10(b). Figures 6.10(c)-(d) show that when $T > 0.8\,\mathrm{K}$, $R_{V1} = 80\,\mathrm{m\Omega}$ and $R_{V2} = 108\,\mathrm{m\Omega}$ and a single narrow superconducting transition at $T_c = 0.73\,\mathrm{K}$ is measured in both set-ups. However, when $T \ll T_c$, $R_{V1} \approx 0.1\,\mathrm{m\Omega}$, and $R_{V2} \approx 5\,\mathrm{m\Omega}$; the residual resistance in R_{V2} may be attributed to some resistance in series to the superconductor. This maybe attributed to either the bonding process, the semiconductor beneath or something else, this was beyond the scope of this thesis to investigate. For both directions, the difference between the normal state resistance and the superconducting state $\Delta T_c \approx 0.05\,\mathrm{K}$, this is defined as the difference in temperature between the transition when $T = 0.8\,\mathrm{K}$ and $R_{V1} \approx 80\,\mathrm{m\Omega}$, $R_{V2} \approx 105\,\mathrm{m\Omega}$ and when the superconducting transition has occurred at $T \approx 0.7\,\mathrm{K}$.

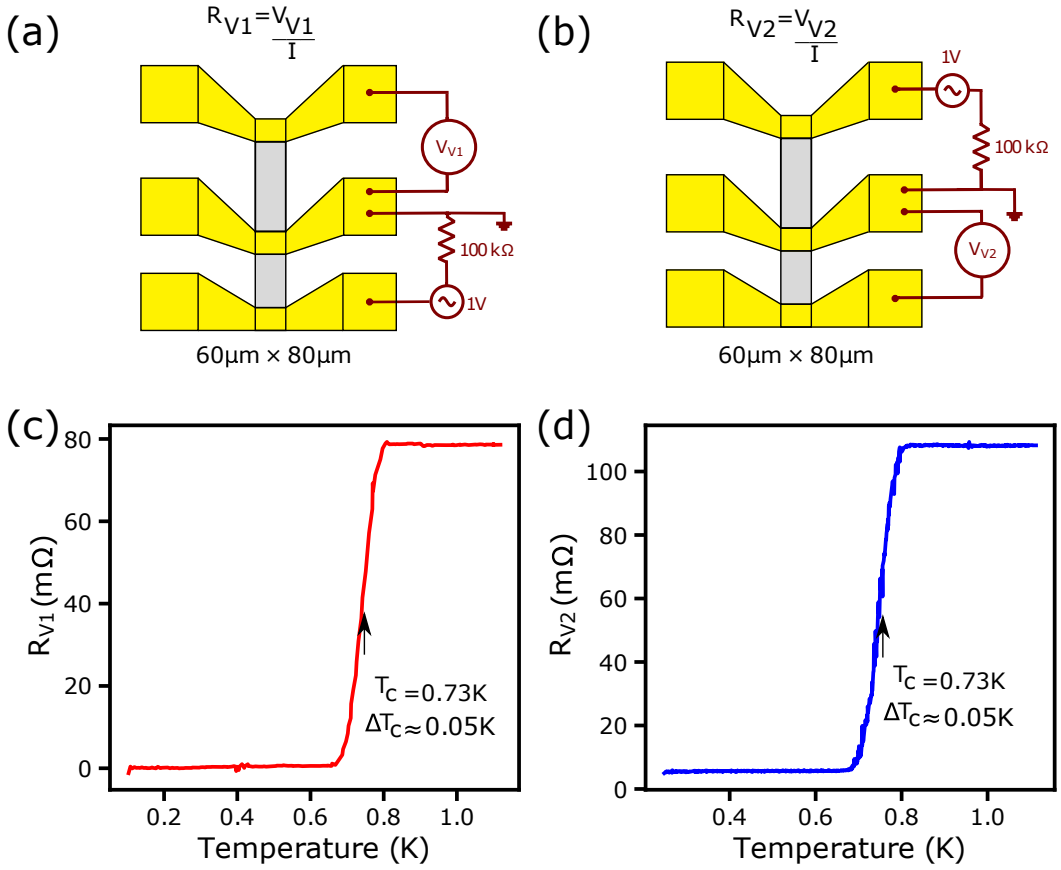

Figure 6.10: Sample G set-ups and results. The $60\,\mu\text{m} \times 80\,\mu\text{m}$ Ohmic contacts are annealed onto the mesa. (a) The set-up to measure the resistance R_{V1}, which is defined when the current $I = 0.01\,\text{mA}$ is driven between the bottom two contacts and measured by the voltage V_{V1}, therefore $R_{V1} = V_{V1}/I$. (b) To measure R_{V2}, the current of $I = 0.1\,\text{mA}$ is driven between the top two contacts and V_{V2} measures $R_{V2} = V_{V2}/I$. (c) The resistance $R_{V1}(T)$. When $T > 0.8\,\text{K}, R_{V1} = 80\,\text{m}\Omega$, but as the sample is cooled below $T < 0.8\,\text{K}$, there is a single narrow transition at $T_c = 0.73\,\text{K}$, with a $\Delta T_c \approx 0.05\,\text{K}$ and when $T < T_c$, $R_{V1} \approx 0.1\,\text{m}\Omega$. (d) The resistance $R_{V2}(T)$. When $T > 0.8\,\text{K}$, $R_{V2} = 108\,\text{m}\Omega$, as the sample is cooled below $T < 0.8\,\text{K}$ there is a single narrow transition at $T_c = 0.73\,\text{K}$ with a $\Delta T_c \approx 0.05\,\text{K}$; when $T < T_c$ $R_{V2} \approx 5\,\text{m}\Omega$.

The R_V measurements of samples H and I are presented next, these are NTLM devices, but using different Ohmic contact recipes, see Table 3.2. The circuits measure the vertical resistance of the centre Ohmic contact and use a mixture of Ohmic contacts some of which are not annealed onto the mesa to measure the voltage V_V. In both samples, there are multiple superconducting phase transitions in the step R_V, which we label $T_{c1}, T_{c2}...T_{cn}$.

Figure 6.11 shows the set-up and measurement of the $R_V(T)$ for Sample H; in this measurement the R_{V1} and R_{V2} of the centre $200\,\mu\mathrm{m} \times 200\,\mu\mathrm{m}$ Ohmic contact is measured. The set-up in Fig. 6.11(a) shows a current of $I = 0.01\,\mathrm{mA}$ being passed between the two left-hand side contacts and the voltage V_{V1} is measured between the off-mesa contact and the centre contact measures $R_{V1} = V_{V1}/I$. Figure 6.11(b) shows the current is passed between the off-mesa and the centre contact, the voltage V_{V2} is measured between the centre contact and the left-hand side contact measures $R_{V2} = V_{V2}/I$. Figures 6.11(c)-(d) shows that when $T > 0.9\,\mathrm{K}$, $R_{V1} = 30\,\mathrm{m\Omega}$ and $R_{V2} = 30\,\mathrm{m\Omega}$ and there are at least four different phases, three of which are superconducting; in both measurements when the temperature is lower than the lowest critical temperature, $R_V \approx 3\,\mathrm{m\Omega}$; this is evidence of a non-superconducting material in series with the superconductor in the vertical direction.

For Sample I, two off-mesa contacts are used to measure the R_V of the centre contact, see Fig. 6.12. To measure the resistance R_{V1}, the set-up in Fig. 6.12(a) is used where a current $I = 0.01\,\mathrm{mA}$ is driven between the left-hand off-mesa contact and the voltage V_{V1} measures $R_{V1} = V_{V1}/I$. To measure R_{V2} the current is driven between the right-hand off-mesa and the centre contact and the voltage V_{V2} measures $R_{V2} = V_{V2}/I$, see Fig. 6.12(b). The results in Figs. 6.12(c)-(d) shows that when $T > 1.3\,\mathrm{K}$, $R_{V1} = 25\,\mathrm{m\Omega}$ and $R_{V2} = 26\,\mathrm{m\Omega}$; in both measurements there are five phases, but when $T < T_{c5}$, $R_V \approx 0.1\,\mathrm{m\Omega}$. In the temperature range shown, as T increases so does R_V suggesting possible further transitions at higher temperatures.

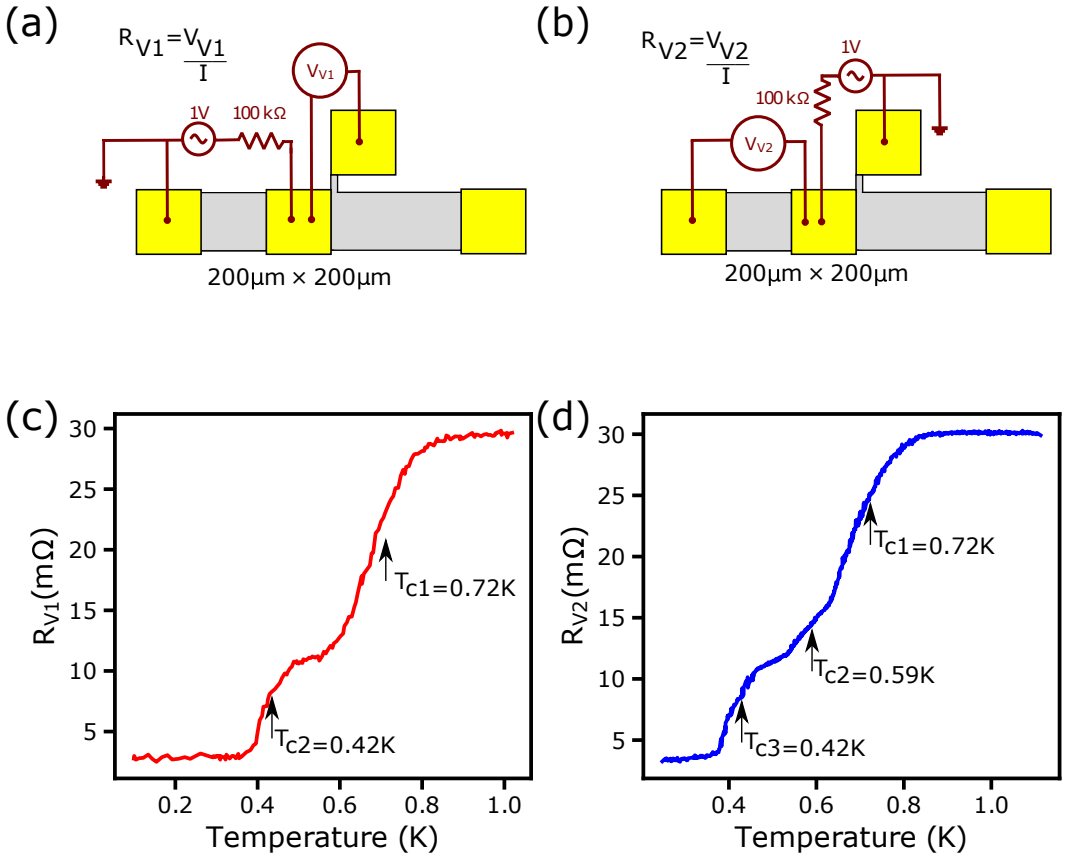

Figure 6.11: Sample H set-ups and results. (a) To measure the resistance R_{V1}, a current $I = 0.01\,\mathrm{mA}$ is driven between the two left-hand contacts and the voltage V_{V1} measured between the off-mesa contact measures $R_{V1} = V_{V1}/I$. (b) To measure the resistance R_{V2}, the current $I = 0.01\,\mathrm{mA}$ is driven between the centre contact and the off-mesa contact, the voltage V_{V2} measured between the centre contact and the left-hand contact measures $R_{V2} = V_{V2}/I$. (c) The measurement of $R_{V1}(T)$ shows when $T > 0.9\,\mathrm{K}$, $R_{V1} = 30\,\mathrm{m\Omega}$. There are at least two superconducting phases at $T_{c1} = 0.72\,\mathrm{K}$ and $T_{c2} = 0.42\,\mathrm{K}$, when $T < T_{c2}$ $R_{V1} \approx 3\,\mathrm{m\Omega}$. (d) The data for $R_{V2}(T)$ shows when $T > 0.9\,\mathrm{K}$, $R_{V2} = 30\,\mathrm{m\Omega}$. There are at least three superconducting phases at $T_{c1} = 0.72\,\mathrm{K}$, $T_{c2} = 0.59\,\mathrm{K}$ and $T_{c3} = 0.42\,\mathrm{K}$ and when $T < T_{c3}$, $R_{V2} \approx 3\,\mathrm{m\Omega}$.

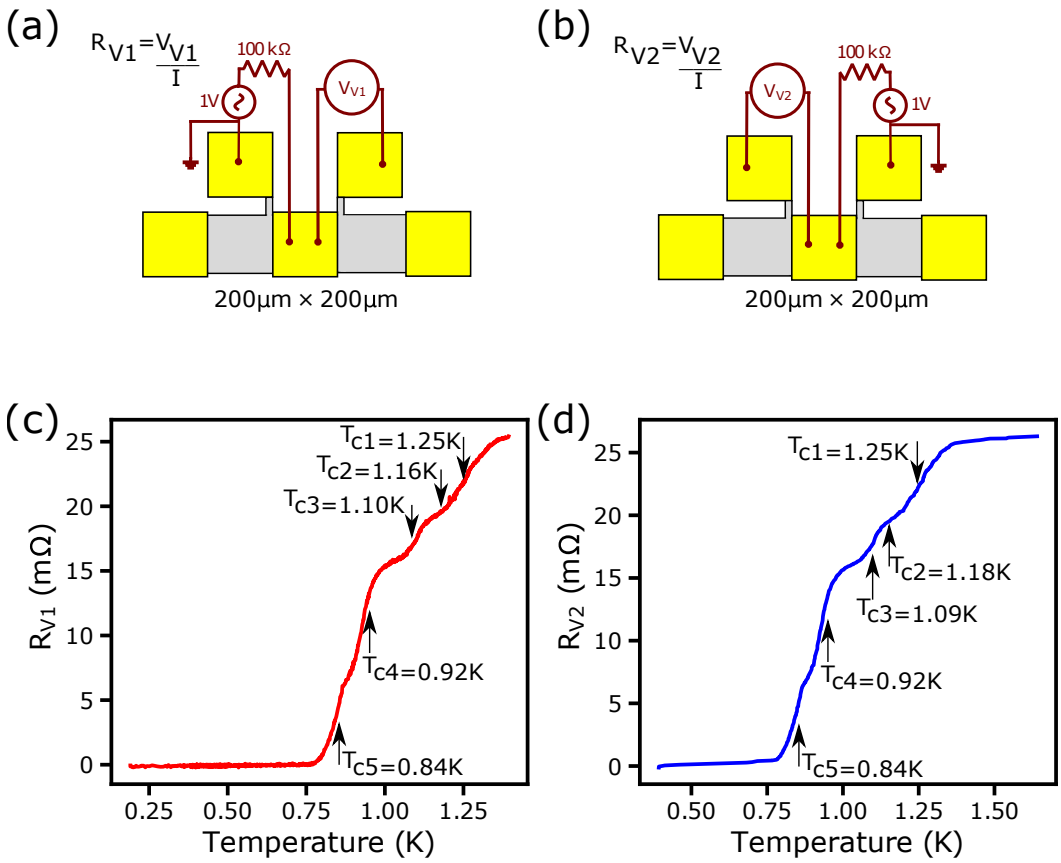

Figure 6.12: Sample I set-ups and results. (a) To measure the resistance R_{V1}, a current $I = 0.1\,\mathrm{mA}$ is driven between the central contact and the left-hand off-mesa contact, the voltage V_{V1} measures $R_{V1} = V_{V1}/I$. (b) To measure the resistance R_{V2}, the current $I = 0.1\,\mathrm{mA}$ is driven between the right-hand off-mesa and the centre contact, the voltage V_{V2} measures $R_{V2} = V_{V2}/I$. (c) The $R_{V1}(T)$ measurement shows five superconducting phases and when $T > T_{c1}$, $R_{V1} = 25\,\mathrm{m\Omega}$, but when $T < T_{c5}$, $R_{V1} \approx 0.1\,\mathrm{m\Omega}$. (d) The $R_{V2}(T)$ data shows at least five superconducting phases and when $T > T_{c1}$, $R_{V2} \approx 26\,\mathrm{m\Omega}$ however, when $T < T_{c5}$, $R_{V2} \approx 0.1\,\mathrm{m\Omega}$.

6.4 Top resistance R_{top}

6.4.1 R_{top} Measurements

Further evidence of superconducting behaviour, with a clearer drop to a low temperature zero-resistance state, is obtained from surface resistance measurements of a single Ohmic contact, this we call R_{top}, which is a four-terminal measurement providing clearer evidence of superconductivity because it only measures the surface of the contact alloy and has no contribution in the measurement from the semiconductor beneath or 2DEG below. In this section, we show R_{top} results for Samples C, D and E.

Sample C is a $4\,\mathrm{mm} \times 4\,\mathrm{mm}$ device with the same Ohmic contact recipe as other $4\,\mathrm{mm} \times 4\,\mathrm{mm}$ devices in this thesis, see Table3.2; by measuring R_{top} a comparison of the superconducting transition with and without a semiconductor can be made. Figure 6.13 shows the set-up for a R_{top} measurement for a $4\,\mathrm{mm} \times 4\,\mathrm{mm}$ device. The current $I = 0.01\,\mathrm{mA}$ is driven from one end of the contact to the other and the voltage V_{4T} is measured on the same contact.

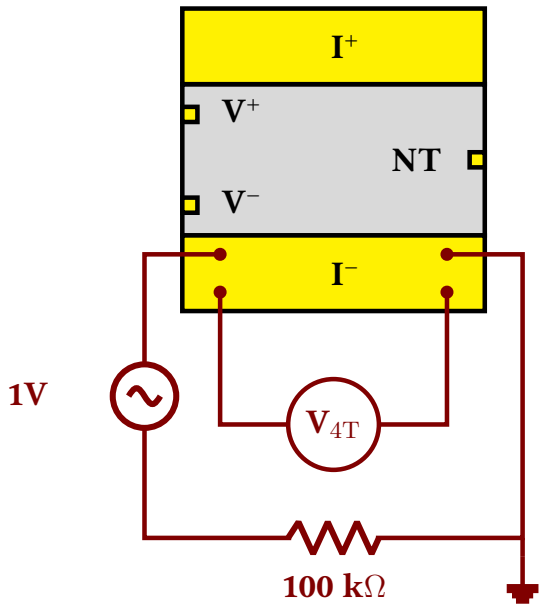

Figure 6.13: Set-up for a four-terminal measurement of R_{top} for a $4\,\mathrm{mm} \times 4\,\mathrm{mm}$ device. A current $I = 0.01\,\mathrm{mA}$ is driven across the contact and the voltage V_{4T} gives the resistance $R_{top} = V_{top}/I$.

6.4.2 Results

The $R_{top}(T)$ data for Sample C in Fig. 6.14(a) shows that when $B_{\perp} = 0\,\mathrm{mT}$, the resistance drops sharply from $R_{top} = 0.65\,\Omega \rightarrow R_{top} = 0.0\,\Omega$, with the superconducting transition centred at $T_c = 0.83\,\mathrm{K}$. However, as B increases, the drop in R_{top} shifts to lower T increasing the low T resistance and when $B = 176\,\mathrm{mT}$, $R_{top}(T)$ is constant. Figure 6.14(b) shows $R_{top}(B)$ sweeps at constant temperature. The data is taken by ensuring the sample is at a fixed temperature of interest and sweeping the magnetic field between $+200\,\mathrm{mT}$ and $-200\,\mathrm{mT}$, these values are chosen based on the experimental data in Fig. 6.14(a).

To characterise the superconductor, two critical fields are defined: $B_{6m\Omega}$ is the field where $R_{top} = 6\,\mathrm{m}\Omega$, and $B_{0.65\Omega}$ is when R_{top} first reaches $0.65\,\Omega$; these quantities as a function of T are shown in Fig. 6.14(c). Although the resulting phase diagram quantifies the effect of B, it is not an indication of whether the superconductor is type I or II.

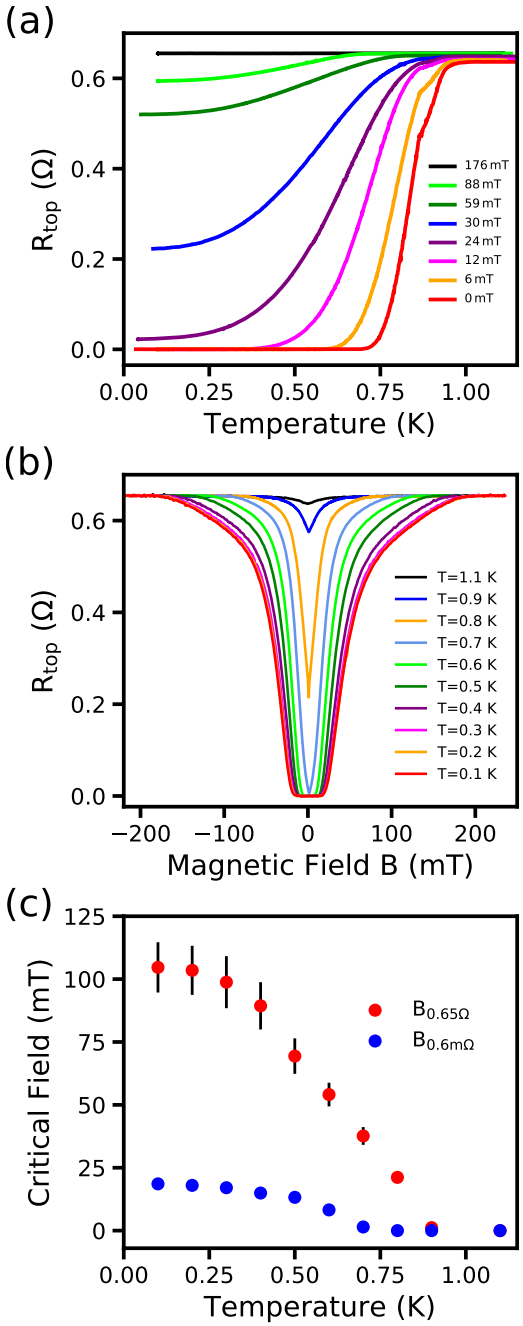

Figure 6.14: Surface resistance of an Ohmic contact R_{top} measurements of Sample C, reproduced from Ref.[86]. (a) $R_{top}(T)$ traces when cooled in constant B fields up to $176\,\mathrm{mT}$. (b) $R_{top}(B)$ sweeps at constant temperatures between $T = 0.1\,\mathrm{K}$ and $T = 1.1\,\mathrm{K}$. (c) "Critical fields": $B_{6m\Omega}$ is the field where $R_{top} = 6\,\mathrm{m}\Omega$, and $B_{0.65\Omega}$ is when R_{top} first reaches $0.65\,\Omega$.

We also measure $R_{top}(T)$ for Sample D and Sample E; D is a layered contact and E is a eutectic contact. The motivation for this measurement is to provide further evidence of superconductivity in other samples. Figures 6.15(a)-(b) show the set-ups for a two-terminal measurement used to measure the Ohmic contact surface resistance of D and E, in both cases there is a total of $14\,\Omega$ lead series resistance which is subtracted from the results shown; the individual lead resistance of the electrical wiring of the cryostat connected to the sample was $7\,\Omega$. For both set-ups, a current of $I = 0.1\,\mathrm{mA}$ is driven from one end of the contact to the other and the voltage V_{top} is measured; for Sample D, the probes are connected to the two off-mesa bond pads and for Sample E the current is driven along the top of the contact. In Fig. **??**(c) Sample D has a sharp transition at $T_c \approx 0.81\,\mathrm{K}$ and when $T < 0.75\,\mathrm{K}$, $R_{top} \approx 0.1\,\mathrm{m}\Omega$. Sample E has a transition that is broad with two possible phases at $T_{c1} \approx 0.64\,\mathrm{K}$ and $T_{c2} \approx 0.38\,\mathrm{K}$, when $T < 0.15\,\mathrm{K}$, $R_{top} \approx 0.1\,\mathrm{m}\Omega$, this is lower than the $T < 0.75\,\mathrm{K}$ value for Sample D, see Fig. 6.15(d). The broad transition of the eutectic contact may be a recipe effect, because this is a similar trace to that shown in Ref.[79] where $R_{top}(T)$ is measured on a eutectic contact of the same recipe. The transition in the layered contact is comparable to Sample G, a TLM device with layered Ohmic contacts from the same batch, see Table 3.2.

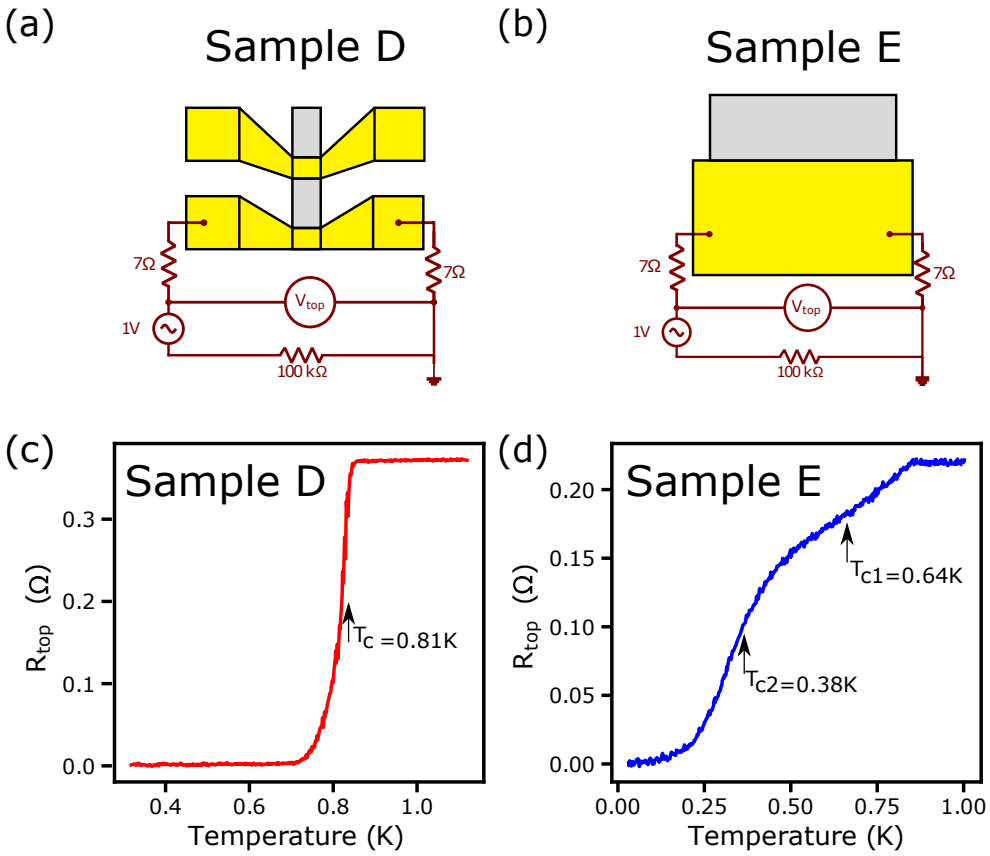

Figure 6.15: Measurements of the surface resistance of an Ohmic contact R_{top} for Sample D and Sample E. In a two-terminal circuit the lead resistance is added to the measured resistance, in this case, the individual lead resistance of the cryostat wiring connected to the sample was $7\,\Omega$ therefore; $14\,\Omega$ is subtracted from the results shown. (a) The set-up to measure R_{top} for Sample D. A current of $I = 0.1\,\mathrm{mA}$ is driven from one end of the contact to the other and the voltage V_{top} is measured between the current probes. The probes are connected to the two off-mesa bond pads which flank the $60\,\mu\mathrm{m} \times 80\,\mu\mathrm{m}$ Ohmic contact. (b) The set-up to measure R_{top} for Sample E. A current of $I = 0.1\,\mathrm{mA}$ is driven along the surface of the $210\,\mu\mathrm{m} \times 300\,\mu\mathrm{m}$ contact and the voltage V_{top} is measured. (c) The trace shows $R_{top}(T)$ for Sample D. There is a sharp transition at $T_c \approx 0.81\,\mathrm{K}$ and when $T < 0.75\,\mathrm{K}$, the resistance is $\approx 0.1\,\mathrm{m}\Omega$. (d) The trace shows $R_{top}(T)$ for Sample E. The transition is broad with two possible phases at $T_{c1} \approx 0.64\,\mathrm{K}$ and $T_{c2} \approx 0.38\,\mathrm{K}$.

6.5 Discussion

The fundamental measurement in this chapter is the contact resistance R_C of Sample A, to find and understand the R_C value is important for the thermal model and improving cooling electrons when $T < 0.1\,\mathrm{K}$. However, from the measurements of R_C, it is shown that the Ohmic contact is superconducting when $T < 0.8\,\mathrm{K}$, thus causing a problem when trying to cool electrons below $0.1\,\mathrm{K}$. This is shown in Sample A when $T > 0.8\,\mathrm{K}$, $R_C \approx 0.8\,\Omega$ and when $B = 0\,\mathrm{mT}$ there is a $0.6\,\Omega$ drop in the contact resistance per contact when $T < 0.8\,\mathrm{K}$. In Sample B, there is also superconductivity in the $200\,\mu\mathrm{m} \times 200\,\mu\mathrm{m}$ contacts, when $B = 0$ and $T > 0.8\,\mathrm{K}$, the contact resistance is $= 2.62\,\Omega$ and when $T < 0.8\,\mathrm{K}$, this reduces to $\approx 2.45\,\Omega$ and the superconductivity is suppressed when $B_{\parallel} = 202\,\mathrm{mT}$.

To further characterise the superconductivity, vertical resistance R_V measurements show that the superconducting component is suppressed at $150\,\mathrm{mT}$ and for a typical $200\,\mu\mathrm{m} \times 200\,\mu\mathrm{m}$ Ohmic contact, $R_V \approx 20\,\mathrm{m\Omega} - 30\,\mathrm{m\Omega}$ and for a $60\,\mu\mathrm{m} \times 80\,\mu\mathrm{m}$ Ohmic contact, $R_V \approx 80\,\mathrm{m\Omega} - 100\,\mathrm{m\Omega}$, a feature observed in some samples are multiple superconducting phases; however, not all vertical resistance samples have a superconducting transition to $\approx 0\,\mathrm{m\Omega}$ in some samples, there is a non-superconducting component in the series with the superconductor, see Table 6.1 summarising the maximum and the minimum resistances for each the sample. We speculate in that this could be the semiconductor beneath, a compound formed during the annealing process or an external effect such dirt or poor bonding, but it was beyond the scope of this thesis to investigate this further.

From R_V values when $T > T_c$ given in Table 6.1 and the current-crowding model, see Ref.[55], for $200\,\mu\mathrm{m} \times 200\,\mu\mathrm{m}$ Ohmic contacts the transfer length $T_L \approx 40\,\mu\mathrm{m}$ and for a $60\,\mu\mathrm{m} \times 80\,\mu\mathrm{m}$ Ohmic contact $T_L \approx 18\,\mu\mathrm{m}$; in this thesis although we do not measure R_C of Sample G, it is $4.7\,\Omega$. Measurements of devices with $200\,\mu\mathrm{m} \times 200\,\mu\mathrm{m}$ contacts show that, $R_C \approx 2.6\,\Omega$ and from Table 6.1, $R_V \approx 25\,\mathrm{m}\Omega$-$30\,\mathrm{m}\Omega$ for $T > T_c$; from this we can suggest that due to the low resistance in the vertical direction, the current will always take the vertical path direction.

For the resistance along the top of the contact, we see the broadest transitions are obtained with a AuGeNi eutectic slug contact and the narrowest transitions with the highest T_c are obtained in layered eutectic contacts, see Fig. 6.15; this effect is clearest in the $R_{top}(T)$ measurement of Sample C where a clear drop to a low temperature zero-resistance state is shown. The R_{top} measurements, which show the superconductivity without any semiconductor contribution gives clear evidence that the Ohmic contact is superconducting and can suppressed when $B \approx 176\,\mathrm{mT}$.

We have shown that for $T > T_c$, both R_{top} and R_V are constant up to $T \approx 20\,\mathrm{K}$, this is behaviour characteristic of a disordered alloy not the semiconductor underneath the Ohmic contact, but it is difficult to correlate the different superconducting phases observed with the processing conditions. These measurements show superconductivity can easily be measured by using a straightforward four-terminal measurement of the surface resistance of the Ohmic contact.

Table 6.1: Summary of measured vertical resistance results for Samples F, G, H and I showing R_V and T_c values

Sample	Approx. No. of transi-tions	R_{V1} when $T > T_c$	R_{V2} when $T > T_c$	R_{V1} when $T < T_c$	R_{V2} when $T < T_c$
F	1	$\approx 25\,\mathrm{m\Omega}$	-	$\approx 0.1\,\mathrm{m\Omega}$	-
G	1	$\approx 80\,\mathrm{m\Omega}$	$\approx 108\,\mathrm{m\Omega}$	$\approx 0.1\,\mathrm{m\Omega}$	$\approx 5\,\mathrm{m\Omega}$
H	2-3	$\approx 30\,\mathrm{m\Omega}$	$\approx 30\,\mathrm{m\Omega}$	$\approx 3\,\mathrm{m\Omega}$	$\approx 3\,\mathrm{m\Omega}$
I	5	$\approx 25\,\mathrm{m\Omega}$	$\approx 26\,\mathrm{m\Omega}$	$\approx 0.1\,\mathrm{m\Omega}$	$\approx 0.1\,\mathrm{m\Omega}$

The table shows $R_V(T)$ characteristics of TLM Samples F, G, H and I. In the table, for multiple phase samples, the T_c value refers to the highest or lowest T_c measured. For Sample F we only measured for R_{V1}, this was also measured in a magnetic field and showed superconductivity suppression when B = $150\,\mathrm{mT}$. From R_V, R_C and the current-crowding model, see Ref.[55], when $T > T_c$, the typical transfer length for a $200\,\mu\mathrm{m} \times 200\,\mu\mathrm{m}$ Ohmic contact is $T_L \approx 40\,\mu\mathrm{m}$ and for a $60\,\mu\mathrm{m} \times 80\,\mu\mathrm{m}$ contact $T_L \approx 18\,\mu\mathrm{m}$.

Chapter 7

Non-equilibrium measurements of superconductivity

7.1 Introduction

In this chapter, a number of characterisation measurements have been made of the superconducting properties of AuGeNi Ohmic contacts. Presented here are results for R_{top} and R_V, where the current-voltage characteristics $I - V$ and the differential resistance dV/dI, measured as a function of magnetic field $B_\perp$ and T, further characterise the superconductivity; information on non-equilibrium measurements on superconductors can be found in Ref.[90] and references therein.

7.2 Motivation

From the equilibrium results, we see multiple transitions in many of the R_V measurements, suggesting a system made up of different chemical phases, with different critical temperatures. However, we also see from SEM images of the Ohmic contact microstructure, see Chapter 3, the contacts are an inhomogeneous disordered or granular superconductor, consisting of metallic grains or clusters embedded in a AuGa matrix; this type of superconductor has a percolation effect for the onset of superconductivity[91]. In this type of system, the coupling between the grains or clusters is through the Josephson interaction and the collective behaviour accounts for the critical properties of the system, this coupling is random since the grain's sizes and the distances among them vary randomly through the contact.

A disordered clustered or granular superconductor is characterised by the Josephson coupling, accomplished randomly with a temperature-dependent probability. Since the coupling energy depends on T, more and more grains or clusters are coupled together as T is lowered[92], this can be inferred from the multiple phase transitions seen in $R_V(T)$ measurements, where different clusters, grains or chemical phases will have a different T_c. This mechanism is a percolation process; at a certain T, a cluster of coupled superconducting grains is formed and thus, a superconducting path throughout the contact is formed; for small grains or clusters it is only when T is lowered further and the percentage of participating grains or clusters is increased that bulk like behaviour begins to appear.

The motivation for the measurements presented here is to obtain a qualitative description of the electrical transition, in conjunction with the normal-state resistance; this is measured as a function of B and T. The primary aim is to not only contribute to, but also show a relationship between the onset of superconductivity (I_o) and the information already gained about these superconducting Ohmic contacts; some of the I_o data shown is also presented in Fig. 2(d) in Ref.[86].

7.3 R_{top} Measurement circuit and results

To measure the $I-V$ and dV/dI characteristics of R_{top}, we use the set-up shown in Fig. 7.1 which shows at the output of the signal adder, the AC and DC voltages are combined as, $V_{AC}+V_{DC}$ and when R_{Bias} is inserted into the circuit, the bias current $I_{Bias}=I_{AC}+I_{DC}$. The resistance of the sample R_{Sample} is related to the sample voltage by,

$$V=(I_{AC}+I_{DC})R_{Sample}=V_{AC}^{Sample}+V_{DC}^{Sample} \tag{7.1}$$

and the differential resistance

$$R=\frac{dV}{dI}. \tag{7.2}$$

$R=dV/dI$ is measured by sweeping I_{Bias} and recording V on the lock-in amplifier and the $I-V$ characteristics are measured by sweeping I_{Bias} and measuring the output DC voltage on the DC voltmeter. The AC source in the measurement is provided by the lock-in amplifier and is added to a variable DC source using a signal adder; the output voltage from the signal adder is converted to a current using R_{Bias}, driving the current through the circuit. Voltage probes (V1, V2 in Fig. 7.1) connected to the sample are fed to a differential voltage pre-amplifier; both the signal adder and pre-amplifier are powered by battery packs to reduce mains noise in the set up.

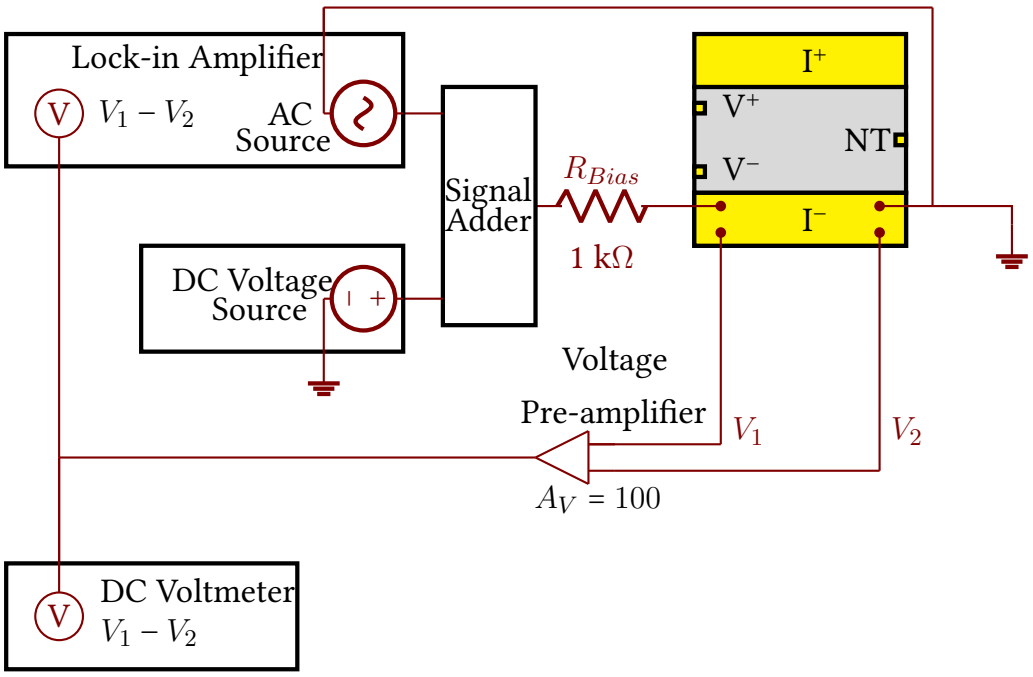

Figure 7.1: Non-equilibrium measurement set-up for the surface resistance of an Ohmic contact R_{top} on a $4\,\mathrm{mm} \times 4\,\mathrm{mm}$ device. At the output of the signal adder, the AC and DC voltages are $V_{AC} + V_{DC}$, generating a bias current when R_{Bias} is inserted into the circuit, the bias current $\frac{V_{AC}}{R_{Bias}} = I_{Bias}$. The resistance of the sample R_{Sample} is related to the sample voltage $V = (I_{AC} + I_{DC})R_{Sample} = V_{AC}^{Sample} + V_{DC}^{Sample}$ and the differential resistance $R = \frac{dV}{dI}$.

In the four-terminal $I - V$ characteristics when $T = 0.1\,\mathrm{K}$ and $B = 0\,\mathrm{mT}$, see Fig. 7.2(a), the DC voltage V_{DC} is measured as the DC current I_{DC} is swept at a rate of $10\,\mathrm{mA/h}$ and we can see there is hysteresis in the up-down characteristics. As a measure of the superconducting behaviour, we define an onset current I_o where the voltage becomes finite; the I_o, the re-entrant current I_r and the voltage gap V_g are taken for the values on the positive side of the trace. In Fig. 7.2(a) the $I - V$ characteristics show a clean supercurrent with the value for the R_{top} normal resistance $R_n = 0.65\,\Omega$, the onset current $I_o = 2.1\,\mathrm{mA}$ and $I_r = 1.05\,\mathrm{mA}$. The shunted voltage gap $V_g = 0.78\,\mathrm{mV}$ is likely shunted with a normal resistance $R_{shunt} = 1.95\,\Omega$, calculated from the slope between $V = 0.0\,\mathrm{mV}$ and $V_g = 0.78\,\mathrm{mV}$, where $\Delta I = 0.4\,\mathrm{mA}$. The dV/dI measurements confirm $I_o = 2.1\,\mathrm{mA}$ and $R_n = 0.65\,\Omega$, see Fig. 7.2(b).

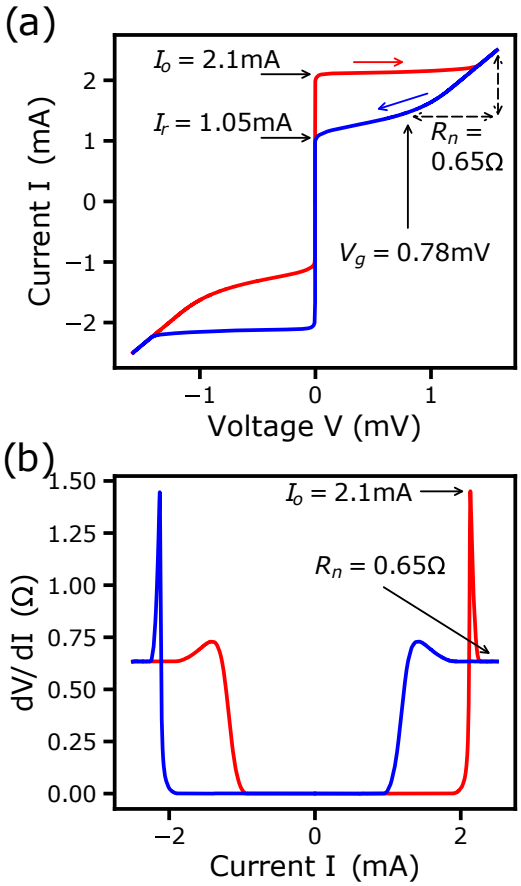

Figure 7.2: Non-equilibrium measurements of the surface resistance of an Ohmic contact R_{top} for Sample C when $T = 0.1\,\mathrm{K}$ and $B = 0\,\mathrm{mT}$. The red traces are up-sweeps and the blue traces are down-sweeps. (a) The $I - V$ characteristics show that the normal resistance $R_n = 0.65\,\Omega$, the onset current $I_o = 2.1\,\mathrm{mA}$, the re-entrant current $I_r = 1.05\,\mathrm{mA}$ and the shunted voltage gap $V_g = 0.78\,\mathrm{mV}$. (b) The dV/dI sweeps show the onset current $I_o = 2.1\,\mathrm{mA}$ and $R_n = 0.65\,\Omega$.

Figure 7.3(a) shows the four-terminal $I-V$ characteristics for different temperatures, we show only the up-sweeps. The characteristics show non-linear behaviour up to T_c = $0.9\,\mathrm{K}$. The dV/dI measurements for different temperatures show that when $T > 0.7\,\mathrm{K}$, the $\approx 0.1\,\mathrm{m\Omega}$ resistance increases and the I_o peaks decrease gradually until $T = 1.1\,\mathrm{K}$, see Fig. 7.3(b). The plotted values for the onset current I_o for different temperatures in Fig. 7.3(c) show that I_o approaches zero at $0.6\,\mathrm{K}$.

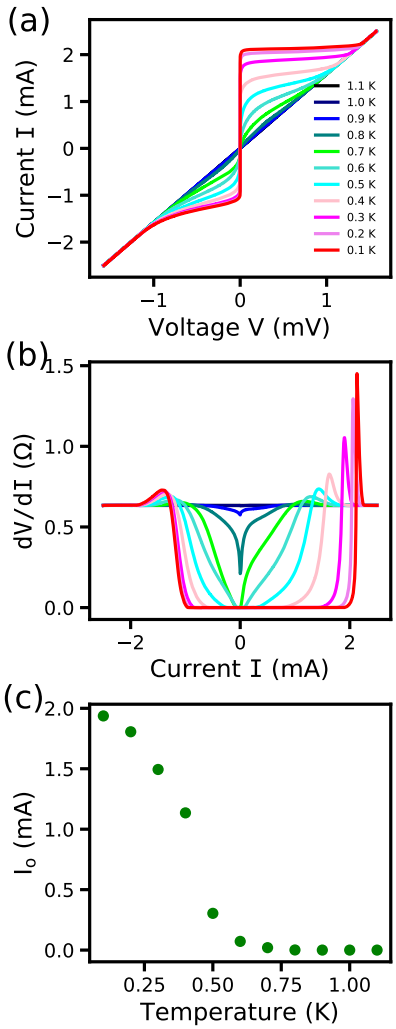

Figure 7.3: Non-equilibrium measurements of R_{top} for Sample C for different temperatures, only the up-sweeps are shown. (a) The $I-V$ characteristics show non-linear behaviour up to T_c = $0.9\,\mathrm{K}$. (b) The dV/dI measurements show as T increases, the I_o decreases, with the last peak at $T = 0.7\,\mathrm{K}$. (c) The onset current I_o plotted for different temperatures.

Figure 7.4(a) shows the four-terminal $I - V$ characteristics for different magnetic fields when $T = 0.1\,\mathrm{K}$, only the up-sweeps are shown. The characteristics show non-linear behaviour up to $B = 150\,\mathrm{mT}$, where $R_n = 0.65\,\Omega$ and that when $B \leq 10\,\mathrm{mT}$ the shunted V_g is still present. In Fig. 7.4(b) the dV/dI sweeps in different magnetic fields B shows that when $B > 25\,\mathrm{mT}$, there are no more I_o peaks, but there is a supercurrent up to $B = 150\,\mathrm{mT}$. The effect of B is also evident by the small increase of resistance of $\approx 0.025\,\Omega$ between the traces for $B = 0\,\mathrm{mT}$ and $B = 150\,\mathrm{mT}$. The plotted values for I_o for magnetic fields in Fig. 7.4(c) show that I_o approaches zero at $B = 10\,\mathrm{mT}$.

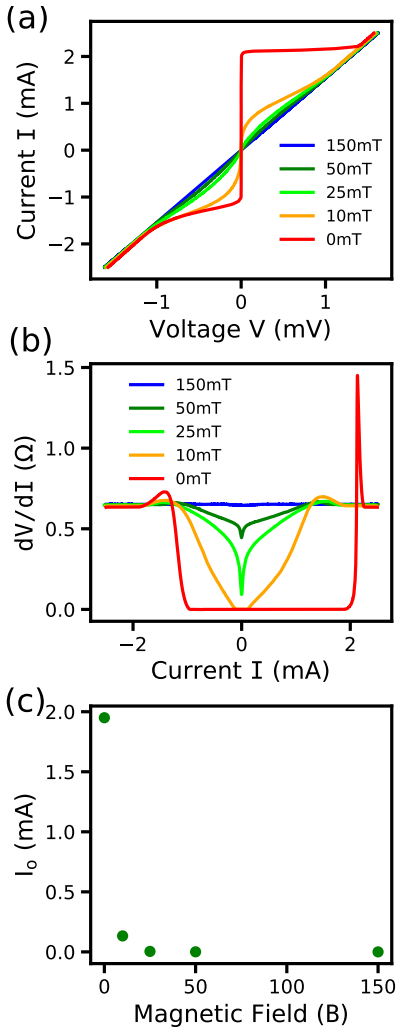

Figure 7.4: Non-equilibrium measurements the surface resistance of an Ohmic contact R_{top} for Sample C for different magnetic fields, only the up-sweeps are shown. (a) The $I-V$ characteristics show. There is non-linear behaviour up to $B = 150\,\mathrm{mT}$ where $R_n = 0.65\,\Omega$. When $B \leq 10\,\mathrm{mT}$ the shunted V_g is still observed. (b) The dV/dI measurements for different B shows when $B > 25\,\mathrm{mT}$, there are no more I_o peaks. The effect of B is evident by the increase of resistance $\approx 0.025\,\Omega$ between the traces for $B = 0\,\mathrm{mT}$ and $B = 150\,\mathrm{mT}$. (c) The onset current I_o plotted for different magnetic fields.

7.4 R_V Measurement circuit and results

To measure the $I-V$ and dV/dI characteristics of R_V, we use the set-up shown in Fig. 7.5. This circuit operates similarly to the circuit in Fig. 7.1, where AC and DC voltages are combined as, $V_{AC}+V_{DC}$ and when R_{Bias} is inserted into the circuit, the bias current $I_{Bias} = I_{AC} + I_{DC}$. The vertical resistance R_V of the sample is related to the vertical voltage V_V by,

$$V = (I_{AC} + I_{DC})R_V = V_{AC}^V + V_{DC}^V. \tag{7.3}$$

In this circuit, R_V is measured by sinking the current on the middle contact and measuring the voltage V_V dropped from the middle to the right-hand side contact using the voltages probes V_1 and V_2.

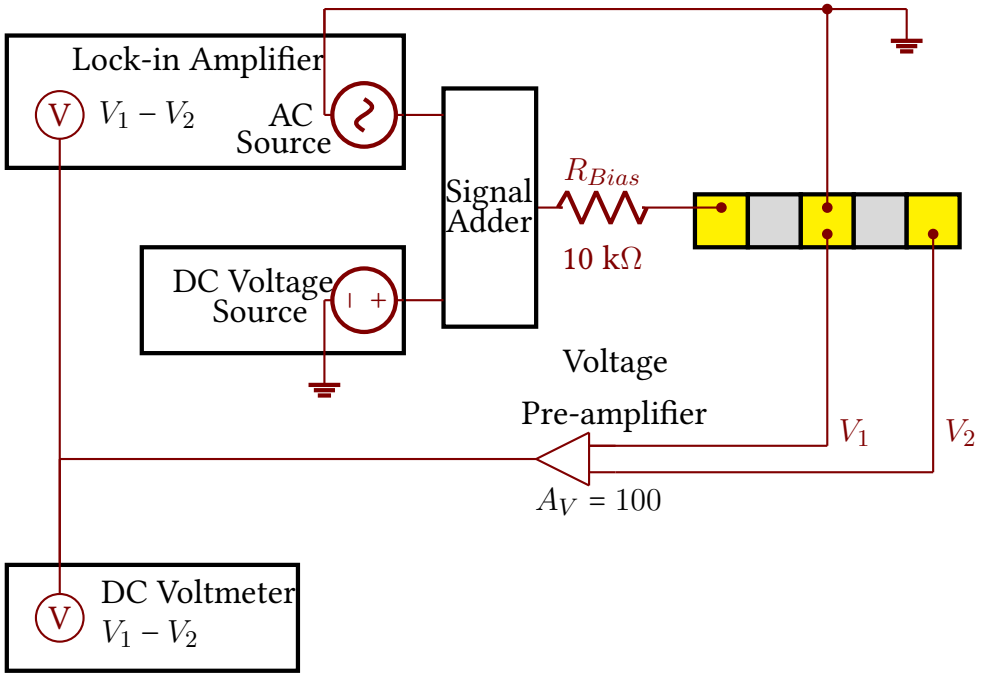

Figure 7.5: [Set-up for a vertical resistance R_V non-equilibrium measurement on a TLM device. At the output of the signal adder, the AC and DC voltages are $V_{AC}+V_{DC}$, generating a bias current when $R_{Bias} = 10\,\text{k}\Omega$ is inserted into the circuit, the bias current $\frac{V_{AC}}{R_{Bias}} = I_{Bias}$. The resistance R_V is related to the sample voltage $V = (I_{AC} + I_{DC})R_V = V_{AC}^V + V_{DC}^V$ and the differential resistance $R = \frac{dV}{dI}$.

In the four-terminal $I - V$ characteristics for Sample I, V_{DC} is measured as I_{DC} is swept at a rate of $2\,\mathrm{mA/h}$. Figure 7.6(a) shows the $I - V$ characteristics for different temperatures. The measurements show non-linear behaviour up to $T = 1.4\,\mathrm{K}$, where the normalised resistance $R_n \approx 30\,\mathrm{m\Omega}$; this is different to the $R_V(T)$ values of $R \approx 26\,\mathrm{m\Omega}$, a further superconducting transition at a higher temperature. When $T = 0.3\,\mathrm{K}$, the shunted voltage gap $V_g = 10.8\,\mu\mathrm{V}$ is shunted with a normal resistance $R_{shunt} = 33\,\mathrm{m\Omega}$, calculated from the slope between $V = 0\,\mu\mathrm{V}$ and $V_g = 10.8\,\mu\mathrm{V}$, where $\Delta I = 327\,\mu\mathrm{A}$. When $T = 0.3\,\mathrm{K}$, $I_o \approx 424\,\mu\mathrm{A}$, see Fig. 7.6(b). The dV/dI sweeps show when $T > 1\,\mathrm{K}$, there is structure on each trace in between the peaks for $I \approx -500\,\mu\mathrm{A}$ and $I \approx 500\,\mu\mathrm{A}$, these are in the resistance range $R \approx 15\,\mathrm{m\Omega}$ to $R \approx 20\,\mathrm{m\Omega}$. A feature of this particular sample is that the resistance increases when $I \gtrapprox 800\,\mu\mathrm{A}$.

The dV/dI characteristics for different temperatures for Sample G, see Fig. 7.6(c), shows when $T < 0.6\,\mathrm{K}$, $I_o \approx 123\,\mu\mathrm{A}$; it is in this temperature range that there is a negative resistance between $I \approx -100\,\mu\mathrm{A}$ and $I \approx 100\,\mu\mathrm{A}$. From the data we can see when $T > 0.8\,\mathrm{K}$, the resistance is $\approx 108\,\mathrm{m\Omega}$, this is also the case when $T < 0.4\,\mathrm{K}$ and $I > 220\,\mu\mathrm{A}$.

Figure 7.6(d) shows dV/dI characteristics for different temperatures for Sample H. In this sample there are no I_o peaks, however for the trace $T = 0.1\,\mathrm{K}$, there is some structure in the trace when $R \approx 13.5\,\mathrm{m\Omega}$, $R \approx 17\,\mathrm{m\Omega}$, $R \approx 21\,\mathrm{m\Omega}$. This can be compared to the $R_V(T)$ data in Fig.6.11 where there are superconducting phases with similar resistances.

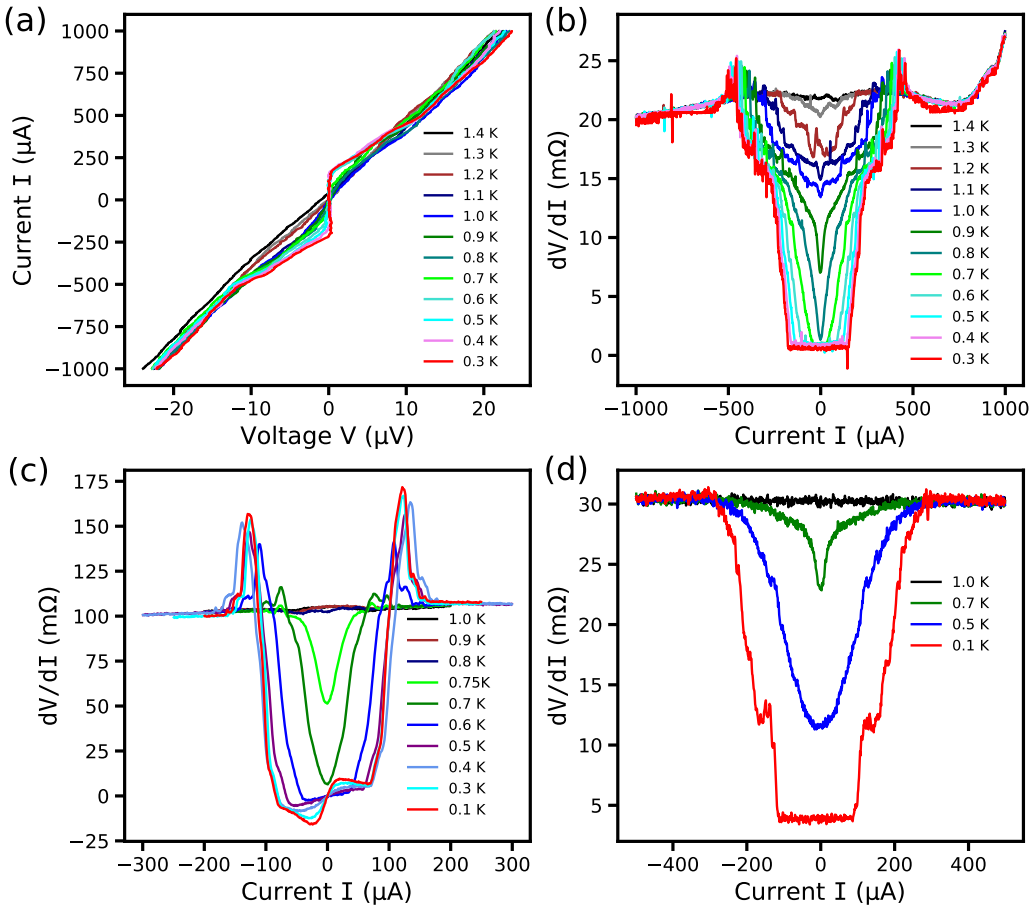

Figure 7.6: Non-equilibrium measurements of the vertical resistance R_V for Samples G, H and I for different temperature. (a) The $I - V$ for Sample I show non-linear behaviour up to $T = 1.4\,\mathrm{K}$, where $R_n \approx 30\,\mathrm{m\Omega}$. When $T = 0.3\,\mathrm{K}$, $I_o = 424\,\mu\mathrm{A}$ and $V_g = 10.8\,\mu\mathrm{V}$, shunted with a normal resistance $R_{shunt} = 33\,\mathrm{m\Omega}$. When $I >\approx 800\,\mu\mathrm{A}$, the resistance continues to increase and does not plateau. (b) The dV/dI sweeps for Sample I show that when $T > 1\,\mathrm{K}$, there are structures within each trace in between $I \approx -500\,\mu\mathrm{A}$ and $I \approx 500\,\mu\mathrm{A}$, these structures are in the range of resistance $R \approx 15\,\mathrm{m\Omega}$ to $R \approx 20\,\mathrm{m\Omega}$, suggesting there could be multiple superconducting transition in this sample. (c) The dV/dI characteristics for Sample G shows when $T < 0.6\,\mathrm{K}$, $I_o \approx 123\,\mu\mathrm{A}$ and there is a negative resistance in between $I \approx -100\,\mu\mathrm{A}$ and $I \approx 100\,\mu\mathrm{A}$. When $T > 0.8\,\mathrm{K}$, the resistance is $\approx 108\,\mathrm{m\Omega}$. (d) The dV/dI characteristics for Sample H shows there are no I_o peaks, however $I_o \approx 220\,\mu\mathrm{A}$ is taken as the value when $T = 0.1\,\mathrm{K}$. The sweep taken at $T = 0.1\,\mathrm{K}$, shows structure at $R \approx 13.5\,\mathrm{m\Omega}$, $R \approx 17\,\mathrm{m\Omega}$, $R \approx 21\,\mathrm{m\Omega}$, this is comparable to data in Fig. 6.11 where there are superconducting phases with similar resistances.

7.5 Discussion

In this chapter we have shown further characterisation of superconducting Ohmic contacts by measuring the $I-V$ and dV/dI characteristics of R_{top} and R_V, these are measurements of the Ohmic contact alloy. The measurements of R_{top} show a superconducting system, with a clear I_o, a single T_c and no subgap structure. The $I-V$ characteristics show when $T = 0.1\,\mathrm{K}$ and $B = 0\,\mathrm{mT}$ there is a supercurrent and hysteresis in the up-down sweeps, see Fig.7.2(a); at this temperature and magnetic field, $R_n = 0.65\,\Omega$, $I_o = 2.1\,\mathrm{mA}$ and $I_r = 1.05\,\mathrm{mA}$. There is a shunted voltage gap $V_g = 0.78\,\mathrm{mV}$ observed which is probably shunted with a normal resistance $R_{shunt} = 1.95\,\Omega$. When the I_o is plotted as a function of temperature when $B = 0$, we see that I_o approaches zero at $T = 0.6\,\mathrm{K}$, but when it is shown as a function of magnetic field when $T = 0.1K$, I_o approaches zero at $B = 10\,\mathrm{mT}$. The measurements of R_V for different samples when $T < T_c$ and $B = 0\,\mathrm{mT}$ shows that the I_o is different for every sample, see Table 7.1.

Table 7.1: Summary of the onset of superconductivity I_o for Samples C, G, H and I.

Sample	Name of Resistance	I_o	R_n
C	R_{top}	$\approx 2.1\,\mathrm{mA}$	$\approx 0.65\,\Omega$
G	R_{V1}	$\approx 0.123\,\mathrm{mA}$	$\approx 0.108\,\Omega$
H	R_{V2}	$\approx 0.220\,\mathrm{mA}$	$\approx 0.030\,\Omega$
I	R_{V1}	$\approx 0.424\,\mathrm{mA}$	$\approx 0.030\,\Omega$

The table shows the onset of superconductivity I_o and normalised resistance R_n for different samples. The I_o value is different for each sample.

A possible explanation of these results could be attributed to the alloys that make up the contact. The alloys could be made up of a different alloy phases of superconducting clusters coupled to normal metal clusters. If these clusters are said to be small and granular, they would be an array of Josephson junctions, acting as a single junction, this is possibly what we see. For instance, the Ohmic contacts in this thesis are comprised of different alloys and the interaction between different phases of alloys along their respective boundaries is described as grain boundary interaction; this describes a granular superconductor operation[93] which occurs when microscopic superconducting grains are separated by non-superconducting regions and Josephson tunnelling between the grains produces the macroscopic superconducting state[94]. Examples of granular superconductivity features that we observe are re-entrant behaviour and hysteresis[95].

The R_V measurements presented have subgap structure, see Fig.7.6. The inner gap or subgap structures can be explained by the proximity effect seen in transport characteristics of heterostructures with transition metals and novel superconductors[96]. This is due to disordered or dirty normal N and superconducting S and multiple Andreev reflection processes; it occurs when the junctions are shorter than the phase coherence length[97, 98].

The dV/dI characteristics for Sample G shows when $T < 0.6\,\mathrm{K}$ there is a negative resistance between $I \approx -100\,\mu\mathrm{A}$ and $I \approx 100\,\mu\mathrm{A}$; negative differential resistance happens between mesoscopic junctions, molecular junctions, granular and metal nanoclusters and is a signature of coherent tunnelling of single Cooper pairs; this effect is called cooper pair leakages and is due to the mismatch between the S and N electronic properties where quasiparticle excitations from the N layer, penetrate into the junction[99–101]. Granular and metal nanocluster superconductors are shunted systems[102] and we observe shunts in Fig.7.6(a) where $R_{shunt} = 33\,\mathrm{m}\Omega$ and in Fig.7.2(a) where $R_{shunt} = 1.95\,\Omega$.

To conclude this chapter, the basic postulate and motivations for these measurements was this: if the Ohmic contact is a granular superconductor, made up of different phases of Au, Ge, Ni, Ga, and As alloys, then we could describe the onset of superconductivity; that is, we could claim that a percolation process achieves the superconductivity. Qualitatively we achieved this by measuring the behaviour of the electrical resistance when it is close to the electrical transition, we refer to this as I_o. In the measurements shown, this is demonstrated because the electrical transition increases with current, temperature or magnetic field; it was also experimentally shown that in all samples, there is a different value for the I_o. From the results in this chapter, we can speculate from measured values of the onset of superconductivity, due to similarities between the data and granular, clustered or similar superconductors found in the literature, the Ohmic contacts in this thesis show a percolation effect, which is a sign of granular superconductivity.

Chapter 8

Summary

8.1 Introduction

In this chapter, the results of the electrical measurements and microstructure are summarised and speculation is made toward the possible superconductor.

8.2 Summary of superconductivity in Ohmic contacts

Electrical resistance measurements of R_C, R_{top}, and R_V of Ohmic contacts have shown superconducting behaviour, Table 8.1 summarises these results; this section discusses, with reference to the Ohmic contact microstructure, these results.

Table 8.1: Summary of T_c for different resistances and samples measured.

Sample	Name of Resistance	T_c
A	R_C	$\approx 0.77\,\mathrm{K}$
B	R_C	$\approx 0.80\,\mathrm{K}$
C	R_{top}	$\approx 0.80\,\mathrm{K}$
D	R_{top}	$\approx 0.81\,\mathrm{K}$
E	R_{top}	$\approx 0.64\,\mathrm{K}$
F	R_V	$\approx 0.6\,\mathrm{K}$
G	R_V	$\approx 0.73\,\mathrm{K}$
H	R_V	$\approx 0.72\,\mathrm{K}$
I	R_V	$\approx 1.25\,\mathrm{K}$

The table shows the critical temperature T_c for different resistances measured. For resistances that show multiple transitions, it is the highest value T_c that is quoted. In all R_{top} and R_V measurements, a magnetic field $B > 150\,\mathrm{mT}$ was able to suppress the superconductivity.

We show that for the $200\,\mu\mathrm{m} \times 200\,\mu\mathrm{m}$ contacts when $T > T_c$, $R_C \approx 2.8\,\Omega$, $R_V \approx 25\,\mathrm{m}\Omega$-$30\,\mathrm{m}\Omega$, $T_L \approx 40\,\mu\mathrm{m}$ and from Ref.[86], $R_{sk} \approx 16\,\Omega$, greater than the sheet resistance in the bulk 2DEG. For the $60\,\mu\mathrm{m} \times 80\,\mu\mathrm{m}$ contact when $T > T_c$, $R_C \approx 4.7\,\Omega$, $R_V \approx 80\,\mathrm{m}\Omega$-$100\,\mathrm{m}\Omega$ and $T_L \approx 18\,\mu\mathrm{m}$.

Equilibrium measurements have shown that when the resistance: R_C, R_{top}, or R_V is measured as a function of temperature, the narrowest transitions with the highest T_c are in AuGeNi layered contacts and the broadest transitions are obtained with eutectic contacts; Ref[86] shows before and after the 2DEG is illuminated to saturation with an LED, the T_c and the drop in resistance below T_c is similar, indicating a superconductor which lies in the material above the 2DEG and in series with the 2DEG. Although multiple superconducting phases are observed, particularly in the $R_V(T)$ measurements, we have drawn no correlation to the relationship between this and the processing conditions.

When the temperature is higher than the highest critical temperature, both R_{top} and R_V are constant for example, we have measured R_{top} up to $T \approx 20\,\mathrm{K}$. This behaviour is characteristic of a disordered alloy. R_{top} measures the Au-rich contact surface which consists of Ni, Ge and As-rich grains surrounded by Au, Ga and Al, this is a similar Ohmic contact surface structure also observed in Refs.[67, 69, 70]. The Au and Ga may be a form of AuGa alloy such as those shown in AuGeNi contacts, see Refs.[23, 38, 39, 42, 67, 71–73], some of which are identified as superconducting[103–110]; Al and Au may form the superconducting alloy of AuAl[106–110].

R_V measures the resistance between the top of the contact and the 2DEG, this comprises of the alloy below the surface of the contact; below the surface lies Ni, Ge and As-rich inclusions of order $\mu\mathrm{m}$ concentrated at the semiconductor interface which, in some cases, consumes some of the GaAs unevenly. This is commonly reported as NiAs, NiAs(Ge) or Ni_2GeAs[23, 25, 27–30, 36, 39, 40, 72]. At the edge, the inclusions are $<1\,\mu\mathrm{m}$. Due to their proximity to the 2DEG, these inclusions are possibly causing damage; larger examples of these structures visible from above as Ni-rich grains penetrate about $200\,\mathrm{nm}$ deeper than the Au-rich top layer, probably reaching the 2DEG. Edge EDX maps confirm reports[74] that Ge leaves the metal layers and diffuses into the GaAs to be the n-type dopant in the GaAs, see Fig. 3.9.

Table 8.2 summarises compounds and elements identified in AuGeNi Ohmic contacts, together with other superconductors that could be formed from Au, Ge, Ni, Ga, As and Al. Without a complete chemical study of the structure, which would show compounds and alloys, it is not possible to identify the superconductor or superconductors in these Ohmic contacts.

Table 8.2: The compounds and elements reported in AuGeNi Ohmic contacts on GaAs/AlGaAs and relating superconductivity made from compounds of Au, Ge, Ni, Ga, Al, and As.

Material	Present in AuGeNi Ohmic contacts yes(Y) or no(N)	Superconducting T_c and B_c properties
α-AuGa	Y[23, 36, 72]	$0.008\,\mathrm{K}$ – $0.264\,\mathrm{K}$[111]
β-AuGa, Au_7Ga_2	Y[15, 30, 31, 38, 69, 72, 112–115]	
Au_4Ga	Y[39, 71]	
Au_2Ga	N	
AuGa	N	$1.24\,\mathrm{K}$ – $1.3\,\mathrm{K}$, $30\,\mathrm{mT}$[104, 105, 108]
$AuGa_2$	Y[35]	$1.7\,\mathrm{K}$, $30\,\mathrm{mT}$[104–106]
α-Ga	Y [116]	$1.083\,\mathrm{K}$, $5.8\,\mathrm{mT}$ [117]
β-Ga	N	$6.04\,\mathrm{K}$, $57\,\mathrm{mT}$
Au(Ge,Ga)	Y[38]	
AuGe	Y[118, 119]	$3.1\,\mathrm{K}$[120]
Au/Ge layered	N	$0.6\,\mathrm{K}$ – $0.8\,\mathrm{K}$[121]
Al	N	$1.175\,\mathrm{K}$, $10.5\,\mathrm{mT}$
α-AuAl	N	$0.008\,\mathrm{K}$ – $0.385\,\mathrm{K}$[111]
$AuAl_2$	N	$0.18\,\mathrm{K}$, $1.2\,\mathrm{mT}$[106, 109, 110]
Au_4Al	N	$0.3\,\mathrm{K}$ – $0.7\,\mathrm{K}$[108]

Elements and compounds identified in AuGeNi Ohmic contacts, and other combinations of Au, Ge, Ni, Ga, Al, and As. Where possible, the critical temperature T_c and magnetic field B_c are provided. This table is also shown in Ref.[86].

The superconductivity is also evident in four-terminal $I-V$ and dV/dI characteristics, in these measurements there is hysteresis in the up-down characteristics; as a measure of the superconducting behaviour, we defined an onset current I_o where the voltage becomes finite. The I_o values obtained when $T < T_c$ shows a different value of I_o for each sample.

$I-V$ characteristics show the shunted resistance $R_{shunt} = 33\,\mathrm{m}\Omega$ for R_V and $R_{shunt} = 1.95\,\Omega$ for R_{top}. The R_{top} measurements suggest that there is a superconductor in parallel with a normal layer with a resistance of $0.65\,\Omega$, we can speculate, from the microstructure investigations of the Ohmic contact, that this latter layer is a disordered Au-rich layer with approximately constant resistance, even when $B < 150\,\mathrm{mT}$ and $T < 1.2\,\mathrm{K}$ are varied; this shunting layer complicates a measurement of the superconducting gap. We can calculate the total R_{top} resistance from $R_n = 0.65\,\Omega$ in parallel with $R_{shunt} = 1.95\,\Omega$ as $\approx 0.5\,\Omega$ and the total resistance calculated from $R_n \approx 25\,\mathrm{m}\Omega$-$30\,\mathrm{m}\Omega$ in parallel with $R_{shunt} = 33\,\mathrm{m}\Omega$ for R_V is $\approx 15\,\mathrm{m}\Omega$.

Using these results, it can be claimed that due to the inhomogeneous structure of the contact, there is not a uniform layer of superconductor, but a granular superconductor made of different normal and superconducting alloy phases in series and parallel. A granular superconductor operates when superconducting grains in close proximity to each other link up to form superconducting paths; it is suggested that the percolation process achieves this.

8.3 Discussion

In this section, we will discuss, speculate and make conjecture on the possible superconductors present in AuGeNi Ohmic contacts.

To begin, the SEM and EDX images show inhomogeneous microstructure within the top metal layer of the contact is consistent with previous studies, see Refs.[19, 30, 122]. The top is Au-rich and there are Ni- and As-rich inclusions positioned just above the interface with the GaAs; these inclusions are typically $0.1\,\mu\mathrm{m}$ – $0.5\,\mu\mathrm{m}$ in size and are spaced apart.

Structural studies[19] show that Ge forms compounds with Ni and As, prior to diffusing into the GaAs as the *n*-type dopant, displacing the Ga. The Ga will then diffuse into the upper part of the contact forming an alloy with Au. The most commonly observed[15, 30, 31, 38, 72, 115, 122] Au-Ga alloy in AuNiGe contacts is β-AuGa, but it is not known to be superconducting. However, there are other Ga-based superconductors with a $T_c \approx 1\,\mathrm{K}$, which could be present. This includes α-AuGa, formed when Ga dissolves into Au to form $Au_{1-x}Ga_x$; in this system, as x varies from 0.03 to 0.1, the T_c ranges between from $8\,\mathrm{mK}$ to $264\,\mathrm{mK}$[111]. Other compounds which could be formed might be AuGa with T_c = $1.1\,\mathrm{K}$ and B_c = $5.7\,\mathrm{mT}$[104], or $AuGa_2$ with T_c = $1.63\,\mathrm{K}$ and B_c = $10\,\mathrm{mT}$, the $I-V$ characteristics of R_{top} for different magnetic fields shows that when B = $10\,\mathrm{mT}$, the superconductor begins to suppress, suggesting $AuGa_2$ may be present. The Au:Ga phase diagram in Refs.[123, 124] show that for 50-67% atomic Ga concentrations, samples can be a mixture of AuGa and $AuGa_2$.

Upon cooling a Au:Ga alloy with > 65% atomic Ga, it will phase separate into α-Ga and $AuGa_2$, both of which are superconducting. α-AuGa has been observed[23, 36, 72] in contacts annealed at $600\,^{\circ}\mathrm{C}$, but if the contacts are annealed at $450\,^{\circ}\mathrm{C}$ they only contain β-AuGa. It is believed[116] the outmigration of Ga from the interface into the Au continues until the Au-Ga solid solubility limit is reached, at 12.5% atomic per cent Ga at $415\,^{\circ}\mathrm{C}$.

The remaining known superconducting elements which may be present, based on Refs.[123, 124], in the Au-rich matrix region is: β-Ga with T_c = 6.1 K and B_c = 57 mT and α-Ga, with T_c = 1.083 K and B_c = 5.8 mT; Ref.[117] studies a single-crystal α-Ga sample, where the $R(T)$, see Fig.1e of Ref.[117] is sensitive to changes of B up to $0.1\,\mathrm{mT}$, this study shows similar behaviour to the $R_{top}(T)$ measurements presented in Chapter 6, see Fig. 8.1.

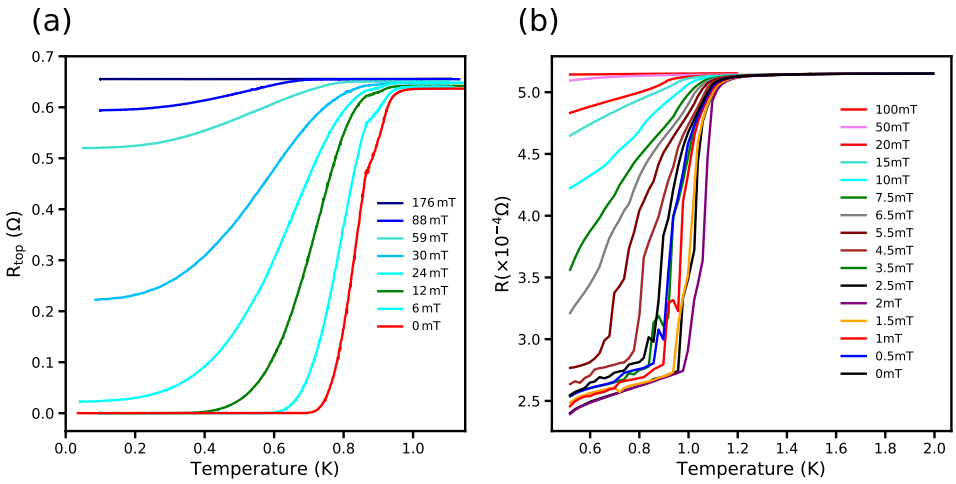

Figure 8.1: Comparison of the surface resistance of an Ohmic contact $R_{top}(T)$ data for Sample C with the $R(T)$ of α-Ga. (a) $R_{top}(T)$ measurements presented in Chapter 6. (b) The α-Ga study shown Fig.1e of Ref.[117]. In the study of a single-crystal α-Ga sample, the $R(T)$ is sensitive to changes of magnetic field up to $0.1\,\mathrm{mT}$ and shows a similar behaviour to (a). α-Ga is a type-I superconductor with T_c = 0.9 K and a critical field of $5.8\,\mathrm{mT}$.

In AuGeNi Ohmic contacts, there is a relation between AuGa α and β transitions. Ref.[125] measures the Au-Ga structure, by heating AuGeNi contacts to $438\,^{\circ}\mathrm{C}$, they report a mix of irregular connected α, α' and β islands of order $\approx 20\,\mu\mathrm{m}$ with $\approx 2\,\mu\mathrm{m}$ Ni-rich islands below the surface. In Ref.[126] β or Au_7Ga_2 dominates, but if cooling is done quickly an additional phase of superconducting Au_2Ga is identified; β-AuGa which is the stable compound Au_7Ga_2, and its presence in the contacts has also been widely reported[38] and Ref.[72] shows if AuGeNi contacts are annealed at $450\,^{\circ}\mathrm{C}$, they only contain β-AuGa, whereas if they are annealed at $600\,^{\circ}\mathrm{C}$ or above they are more resistive and contain α-AuGa; reports[39, 71] show Au_4Ga is not known to be superconducting.

The two phase system of islands is confirmed in Ref.[127] by showing that, upon heating to T = $450\,^{\circ}\mathrm{C}$ α dominates and when cooling to T = $400\,^{\circ}\mathrm{C}$, α diminishes and β or Au_7Ga_2 increases; however, in the transformation from α to β, not all α participates and so, not all α vanishes, leaving clusters; these α clusters are removed by heating the metal up to T = $528\,^{\circ}\mathrm{C}$.

Besides the Ga based compounds, we also detect Al on the surface of the contact, this is also shown to exist in Refs.[14, 70] towards the top of the contact, but in the literature there is no structural evidence of the superconducting (below $1\,\mathrm{K}$) compounds $AuAl_2$ and Au_4Al[106, 108]. The Au:Al phase diagram[111] shows the superconductor α-AuAl, forms when low concentrations of Al, $x \leq 0.15$, dissolve into Au to form $Au_{1-x}Al_x$; the T_c ranges from $8\,\mathrm{mK}$ to $385\,\mathrm{mK}$, as x varies from 0.04 to 0.14. We also detect some Ge on the surface and studies in Refs.[118–121] show Au and Ge can form superconductors.

To conclude, it is suspected that Ga is a constituent of the superconductor, especially as α-Ga, α-AuGa, AuGa, and $AuGa_2$ all have $T_c \approx 1\,\mathrm{K}$, which is what we measure. It could be speculated that R_{top} measures superconducting α-AuGa grains coupled to the normal metal β-AuGa producing a planar granular superconductor, but R_V measures a mixture of different Ga, As, Al, Ge and Au compounds and could be a layered granular superconducting system made up of layers. With the top layer being AuGa-phases, the middle layer being a mixture compounds with different T_c values and the larger Ni-rich inclusions being a shunting resistance, because it electrically shorts the top of the contact to the bottom near the 2DEG.

Chapter 9

Suggested future work and outlook

9.1 Introduction

This final chapter discusses future work and outlook. The chapter summarises how the initial aim of the thesis, cooling low dimensions electrons down, is impacted by the unexpected results of superconducting Ohmic contacts and suggestions are then made for future work to overcome the problems encountered in this field of research.

9.2 Future outlook

This thesis has shown that Ohmic contacts to GaAs based 2DEGs prepared from either AuGeNi eutectic or layered made up of AuGe eutectic and Ni, are superconducting with a typical $T_c \leq 0.9\,\mathrm{K}$ and $B_c = 0.15\,\mathrm{T}$; although we have shown some samples with multiple phases above and below this T_c. We have shown that for future experiments, the T_c and B_c are easily obtained from simple four-terminal R_{top} measurements. As AuNiGe contacts annealed at $400\,^{\circ}\mathrm{C}$ - $450\,^{\circ}\mathrm{C}$ are very common, it is highly likely that superconducting Ohmic contacts have been in previous studies and is probably ubiquitous.

For future transport experiments such as quantum conductance and quantum Hall measurements, the superconductivity will have little effect; as $B_c = 0.15\,\mathrm{T}$, superconductivity will not affect measurements of both the integer and fractional quantum Hall effect, because they use higher magnetic fields. The decrease of $1\,\Omega$ in the contact resistance will not affect the measured four-terminal resistance and because two-terminal conductance measurements are typically done on high resistance samples, this will be difficult to see.

However, for future experiments relating to electron cooling, although the contact resistance is lower below T_c, the main effect superconductivity has on the contacts is the reduction in ability to cool the 2DEG; this is because superconductors have low thermal conductivities κ. In the ultra-low temperature regime, Levitin et al.[79] reports that at $1\,\mathrm{mK}$ - $3\,\mathrm{mK}$, the κ through the contacts is $\approx 10\%$ of that expected from applying the Wiedemann-Franz law to their normal state electrical resistances when $R_C \approx 1\,\Omega$. This reduced cooling by the superconducting contacts when $B < 0.15\,\mathrm{T}$ could explain the historical experimental difficulty in cooling GaAs-based 2DEGs. Therefore, in future when cooling GaAs-based 2DEGs below $T < 1\,\mathrm{K}$, the use of Pd-Ge as a substitute could be of benefit, while Pd-Ga is not a known superconductor Al, Ga and Ge would still be in the contact; both Al and Ga are superconductors and Al, Ga and Ge can form superconducting alloys, but this can be verified using a simple four-terminal R_{top} measurement.

Further research of AuGeNi Ohmic contacts could be the following: probing how superconductivity effects the current-crowding model and investigating R_V and R_{top} as a function of different anneal temperatures because this may indicate when the contacts are superconducting.

Bibliography

[1] Y. Jompol *et al.*, "Probing Spin-Charge Separation in a Tomonaga-Luttinger Liquid," *Science*, vol. **325**, pp. 597–602, July (2009).

[2] S. M. Cronenwett, T. H. Oosterkamp, and L. P. Kouwenhoven, "A Tunable Kondo Effect in Quantum Dots," *Science*, vol. **281**, pp. 540–544, (1998).

[3] R. Willett *et al.*, "Observation of an even-denominator quantum number in the fractional quantum Hall effect.," *Physical Review Letters*, vol. **59**, p. 1776–1779, (1987).

[4] N. J. Appleyard *et al.*, "Direction-resolved transport and possible many-body effects in one-dimensional thermopower," *Phys. Rev. B.*, vol. **62**, pp. 275–278, (2000).

[5] A. Jones *et al.*, "Progress in cooling nanoelectronic devices to ultra-low temperatures," *Journal of Low Temperature Physics*, vol. **201**, pp. 772–802, dec (2020).

[6] Z. Iftikhar *et al.*, "Primary thermometry triad at 6 mk in mesoscopic circuits," *Nature Communications*, vol. **7**, p. 12980, (2016).

[7] S. P. Kurochka *et al.*, "Features of Creating Ohmic Contacts for GaAs/AlGaAs Heterostructures with a Two-dimensional Electron Gas," *Russian Microelectronics*, vol. **46**, pp. 600–607, (2017).

[8] C. Kittel, *Introduction to Solid State Physics*. Wiley, (2004).

[9] A. Baca *et al.*, "A survey of Ohmic contacts to III-V compound semiconductors," *Thin Solid Films*, vol. **308-309**, pp. 599 – 606, (1997).

[10] J. B. Gunn, "Instabilities of Current in III – V Semiconductors," *IBM Journal of Research and Development*, vol. **8**, pp. 141–159, (1964).

[11] N. Braslau, J. B. Gunn, and J. L. Staples, "Metal-semiconductor contacts for GaAs bulk effect devices," *Solid-State Electronics*, vol. **10**, pp. 381–383, (1967).

[12] R. A. Bruce and G. R. Piercy, "An improved Au-Ge-Ni Ohmic contact to n-type GaAs," *Solid-State Electronics*, vol. **30**, p. 729–737, (1987).

[13] A. Callegari *et al.*, "Electrical and thermal stability of AuGeNi ohmic contacts to GaAs fabricated with in situ RF sputter cleaning," *Solid-State Electronics*, vol. **29**, p. 523–527, (1986).

[14] O. Göktas *et al.*, "Alloyed ohmic contacts to two-dimensional electron system in AlGaAs/GaAs heterostructures down to submicron length scale," *Physica E: Low-Dimensional Systems and Nanostructures*, vol. **40**, p. 1579–1581, (2008).

[15] R. K. Ball, "Improvements in the topography of AuGeNi-based ohmic contacts to n-GaAs," *Thin Solid Films*, vol. **176**, p. 55–68, (1989).

[16] S. Tahamtan *et al.*, "A Study on AuGeNi Ohmic contact to n-GaAs Using Microstructural Characteristics," *Symposium on Photonics and Optoelectronics (SOPO)*, (2011).

[17] Z. Tkaczyk and A. Wolkenberg, "Influence of metallic spikes and non-uniform density of two-dimensional electron gas (2 DEG) on the contact resistance to AlGaAs/GaAs heterostructures," *Semiconducting and Insulating Materials 1998. Proceedings of the 10th Conference on Semiconducting and Insulating Materials (SIMC-X)*, (1998).

[18] R. P. Taylor *et al.*, "Investigation of the current injection properties of ohmic spikes in nanostructures.," *Superlattices and Microstructures*, vol. **24**, p. 337–345, (1998).

[19] M. Murakami, "Development of refractory ohmic contact materials for gallium arsenide compound semiconductors," *Science & Technology of Advanced Materials*, vol. **3**, pp. 1–27, (2001).

[20] S. J. Hawksworth *et al.*, "Contact resistance to high-mobility AlGaAs/GaAs heterostructures," *Semiconductor Science and Technology*, vol. **7**, pp. 1085–1090, (1992).

[21] G. S. Saravanan *et al.*, "Ohmic contacts to pseudomorphic HEMTs with low contact resistance due to enhanced Ge penetration through AlGaAs layers.," *Semiconductor Science and Technology*, vol. **23**, p. 025019, (2008).

[22] E. J. Koop *et al.*, "On the annealing mechanism of AuGe/Ni/Au ohmic contacts to a two-dimensional electron gas in GaAs/$Al_xGa_{1-x}As$ heterostructures," *Semiconductor Science Technology*, vol. **28**, p. 025006, (2013).

[23] T. S. Kuan *et al.*, "Electron microscope studies of an alloyed Au/Ni/Au-Ge ohmic contact to GaAs," *Journal of Applied Physics*, vol. **54**, pp. 6952–6957, (1983).

[24] T. K. Higman *et al.*, "Structural analysis of Au–Ni–Ge and Au–Ag–Ge alloyed ohmic contacts on modulation-doped AlGaAs–GaAs heterostructures," *Journal of Applied Physics*, vol. **60**, p. 677–680, (1986).

[25] A. K. Rai *et al.*, "Transmission-electron microscope studies of Au-Ni-Ge based ohmic contacts to GaAs-AlGaAs MODFET device," *Journal of Applied Physics*, vol. **61**, p. 4682–4688, (1987).

[26] J. B. Oliveira *et al.*, "Characterization of AuGeNi ohmic contacts on n-GaAs using

electrical measurements, Auger electron spectroscopy and X-ray diffractometry," *Vacuum*, vol. **41**, p. 807–810, (1990).

[27] E. Relling and A. P. Botha, "Solid state diffusion in GaAs/AuGe/Ni and GaAs/Ni/AuGe/Ni ohmic contacts," *Applied Surface Science*, vol. **35**, p. 380–387, (1989).

[28] D. Langer *et al.*, "Structure and Lateral Diffusion of Ohmic Contacts in GaAs/AlGaAs High Electron-Mobility Transistors and GaAs devices," *Journal of Vacuum Science and Technology B*, vol. **5**, pp. 1032–1033, (1987).

[29] V. I. Egorkin *et al.*, "Optimization of ohmic contacts to n-GaAs layers of heterobipolar nanoheterostructures," *Russian Microelectronics*, vol. **46**, p. 272–276, (2017).

[30] H. Goronkin *et al.*, "Ohmic contact penetration and encroachment in GaAs/AlGaAs and GaAs FETs," *IEEE Transactions on Electron Devices*, vol. **36**, p. 281–288, (1989).

[31] A. K. Rai *et al.*, "Alloying behavior of gold, Au-Ge and Au-Ge-Ni on GaAs," *Thin Solid Films*, vol. **114**, p. 379–398, (1984).

[32] T. S. Abhilash *et al.*, "Influence of Nickel layer thickness on the magnetic properties and contact resistance of AuGe/Ni/Au ohmic contacts to GaAs/AlGaAs heterostructures," *Journal of Physics D: Applied Physics*, vol. **42**, p. 125104, (2009).

[33] H. Lin *et al.*, "Optimization of AuGe-Ni-Au ohmic contacts for GaAs MOSFETs," *IEEE Transactions on Electron Devices*, vol. **50**, pp. 880–885, (2003).

[34] M. Murakami, "Development of ohmic contact materials for GaAs integrated circuits," *Materials Science Reports*, vol. **5**, pp. 273–317, (1990).

[35] Z. Liliental-Weber, "The structure and electrical properties of metal contacts on

GaAs," *Journal of Vacuum Science & Technology B: Microelectronics and Nanometer Structures*, vol. **5**, p. 1007, (1987).

[36] A. Callegari *et al.*, "Uniform and thermally stable AuGeNi ohmic contacts to GaAs," *Applied Physics Letters*, vol. **46**, p. 1141–1143, (1985).

[37] T. Kim and D. D. L. Chung, "Transmission electron microscopy study of the interfacial reactions in gold-based contacts to gallium arsenide," *Philosophical Magazine A*, vol. **62**, p. 283–317, (1990).

[38] Y. Shih *et al.*, "Effects of interfacial microstructure on uniformity and thermal stability of AuNiGe ohmic contact to n-type GaAs," *Journal of Applied Physics*, vol. **62**, p. 582–590, (1987).

[39] N. E. Lumpkin *et al.*, "The role of Ni in the formation of low resistance Ni–Ge–Au ohmic contacts to n^+ GaAs heterostructures," *Journal of Materials Research*, vol. **14**, pp. 1261–1271, (1999).

[40] A. K. Rai *et al.*, "Microstructural characterization of AlGaAs-GaAs modulation-doped field-effect transistor ohmic contacts formed by transient annealing," *Journal of Applied Physics*, vol. **63**, pp. 4723–4727, (1988).

[41] M. Heiblum *et al.*, "Characteristics of AuGeNi ohmic contacts to GaAs," *Solid-State Electronics*, vol. **25**, pp. 185–195, (1982).

[42] M. P. Grimshaw, *A Microstructural Investigation of NiAuGe ohmic contacts on to n-type GaAs with a zirconium diboride diffusion barrier*. Phd thesis, Department of Materials, Imperial College of Science and Technology, (1990).

[43] W. Schottky, "Vereinfachte und erweiterte Theorie der Randschichtgleichrichter," *Zeitschrift für Physik*, vol. **118**, pp. 539–592, (1942).

[44] J. Bardeen, "Surface States and Rectification at a Metal Semi-Conductor Contact," *Physical Review*, vol. **71**, pp. 717–727, (1947).

[45] F. A. Padovani, *Semiconductors and Semimetals*, vol. **7**. Academic Press, New York„ (1971).

[46] E. H. Rhoderick, "Metal-semiconductor contacts," in *Solid State and Electron Devices*, vol. **129**, (1982).

[47] V. L. Rideout, "A review of the theory and technology for ohmic contacts to group III-V compound semiconductors," *Solid-State Electronics*, vol. **18**, p. 541–550, (1975).

[48] A. Piotrowska *et al.*, "Ohmic contacts to III–V compound semiconductors: A review of fabrication techniques," *Solid-State Electronics*, vol. **26**, pp. 179–197, (1983).

[49] N. Braslau, "Contact and metallization problems in GaAs integrated circuits," *Journal of Vacuum Science & Technology A: Vacuum, Surfaces, and Films*, vol. **4**, pp. 3085–3090, (1986).

[50] T. J. Kim and P. H. Holloway, "Ohmic contacts to GaAs epitaxial layers," *Critical Reviews in Solid State and Materials Sciences*, vol. **22**, p. 239–273, (1997).

[51] W. Shockley, *Theory and experiment on current transfer from alloyed contact to diffused layer.* Technical Documentary Report No. AL TDR 64-207, (1964).

[52] H. H. Berger, "Models for contacts to planar devices," *Solid-State Electronics*, vol. **15**, p. 1145–158, (1972).

[53] H. Murrmann and D. Widmann, "Current crowding on metal contacts to planar devices," *IEEE Transactions on Electron Devices*, vol. **16**, p. 1022–1024, (1969).

[54] I. F. Chang, "Contact resistance in diffused resistors," *Journal of The Electrochemical Society*, vol. **117**, p. 368, (1970).

[55] G. K. Reeves and H. B. Harrison, "Obtaining the specific contact resistance from transmission line model measurements," *IEEE Electron Device Letters*, vol. **3**, pp. 111–113, (1982).

[56] M. Tinkham, *Introduction to Superconductivity*. McGraw-Hill, second ed., (1996).

[57] A. C. Rose-Innes and H. Rhoderick, eds., *Introduction to Superconductivity*. Pergamon, (1978).

[58] K. v. Klitzing, G. Dorda, and M. Pepper, "New Method for High-Accuracy Determination of the Fine-Structure Constant Based on Quantized Hall Resistance," *Physical Review Letters*, vol. **45**, pp. 494–497, (1980).

[59] D. Tsui, H. L. Stormer, and A. C. Gossard, "Two-Dimensional Magnetotransport in the Extreme Quantum Limit," *Physical Review Letters*, vol. **48**, p. 1559–1562, (1982).

[60] T. J. Thornton *et al.*, "One-Dimensional Conduction in the 2D Electron Gas of a GaAs-AlGaAs Heterojunction," *Physical Review Letters*, vol. **56**, pp. 1198–1201, (1986).

[61] A. Y. Cho and J. Arthur, "Molecular beam epitaxy," *Progress in solid state chemistry*, vol. **10**, pp. 157–191, (1975).

[62] R. Dingle *et al.*, "Electron Mobilities in Modulation-Doped Semiconductor Heterojunction Super-Lattices," *Appl. Phys. Lett.*, vol. **33**, pp. 665–667, (1978).

[63] R. Fletcher *et al.*, "Persistent photoconductivity and two-band effects in GaAs/$Al_xGa_{1-x}As$ heterojunctions," *Physical Review B*, vol. **41**, p. 10649–10666, (1990).

[64] K. Barham and D.Vvedenksy, eds., *Low-dimensional semiconductor structures*, Cambridge University Press, (2001).

[65] T. J. Drummond *et al.*, "Photoconductivity effects in extremely high mobility modulation-doped (Al,Ga)As/GaAs heterostructures," *Journal of Applied Physics*, vol. **53**, p. 1238–1240, (1982).

[66] E. V. Erofeev and V. A. Kagadei, "Study of the improvement of the AuGeNi ohmic contacts to n-GaAs," *2008 18th International Crimean Conference - Microwave & Telecommunication Technology*, (2008).

[67] O. Göktas, *Small alloyed ohmic contacts to 2DES and submicron scale Corbino devices in strong magnetic fields: observation of a zero bias anomaly and single-electron charging*. Phd thesis, Max-Planck-Institut für Festkörperforschung Stuttgart, (2009).

[68] M. Kamada *et al.*, "Investigation of orientation effect on contact resistance in selectively doped AlGaAs/GaAs heterostructures," *Applied Physics Letters*, vol. **49**, p. 1263–1265, (1986).

[69] D. Kumar, "Au/AuGeNi contacts to GaAs Formed by Rapid Electron-Beam Processing," *Physica Status Solidi (a)*, vol. **139**, pp. 433–441, (1993).

[70] A. Christou and N. Papanicolaou, "Redistribution of aluminum in MODFET ohmic contacts," *Solid-State Electronics*, vol. **29**, p. 189–192, (1986).

[71] M. Procop *et al.*, "The importance of the Ni to Ge ratio and of the annealing cycle for the resistivity and morphology of NiAuGe ohmic contacts to n-GaAs," *Physica Status Solidi A*, vol. **104**, pp. 903–916, (1987).

[72] M. Murakami, "Microstructure studies of AuNiGe Ohmic contacts to n-type GaAs," *Journal of Vacuum Science and Technology B: Microelectronics and Nanometer Structures*, vol. **4**, p. 903, (1986).

[73] X. Zhang, *A Microstructural Investigation of AuGe and NiAuGe ohmic contacts on GaAs*. Phd thesis, Department of Materials, Imperial College of Science and Technology, (1987).

[74] R. P. Gupta *et al.*, "Influence of gallium in a metallisation on GaAs.," *IEE Proceedings I Solid State and Electron Devices*, vol. **135**, p. 25, (1988).

[75] F. Pobell, *Matter and Methods at Low Temperatures*. Springer – Verlag, 2 ed., (1996).

[76] A. J. Casey *et al.*, "Current Sensing Noise Thermometry: A Fast Practical Solution to Low Temperature Measurement," *Journal of Low Temperature Physics*, vol. **175**, pp. 764–775, (2014).

[77] A. Shibahara *et al.*, "Primary current-sensing noise thermometry in the millikelvin regime," *Philosophical Transactions A*, vol. **374**, (2016).

[78] J. Clarke and A. I. Braginski, eds., *The SQUID Handbook - Vol I Fundamentals and Technology of SQUIDs and SQUID Systems*, vol. **1**. WileyVCH, (2004).

[79] L. V. Levitin *et al.*, "Preprint: Ultra-low-temperature platform for transport measurements on low-dimensional electron systems," (2020).

[80] A. Mittal *et al.*, "Electron temperature and thermal conductance of GaAs 2D electron gas samples below 0.5 K," *Physica B: Condensed Matter*, vol. **194-196**, pp. 167–168, (1994).

[81] N. J. Appleyard *et al.*, "Thermometer for the 2D Electron Gas using 1D Thermopower," *Physical Review Letters*, vol. **81**, pp. 3491–3494, (1998).

[82] P. J. Price, "Hot electrons in a GaAs heterolayer at low temperature," *Journal of Applied Physics*, vol. **53**, p. 6863–6866, (1982).

[83] D. K. Cheng, *Field and wave electromagnetics*. Addison-Wesley Publishing Company, (1983).

[84] P. M. Hall, "Resistance calculations for thin film patterns," *Thin Solid Films*, vol. **1**, pp. 277–295, (1969).

[85] P. M. Hall, "Resistance calculations for thin film rectangles," *Thin Solid Films*, vol. **300**, p. 256–264, (1997).

[86] C. B. Beauchamp *et al.*, "Superconductivity in AuNiGe Ohmic contacts to a GaAs-based high mobility two-dimensional electron gas," *Applied Physics Letters*, vol. **117**, p. 162104, (2020).

[87] J. R. Williams *et al.*, "Quantum Hall conductance of two-terminal graphene devices," *Physical Review B*, vol. **80**, p. 045408, (2009).

[88] D. A. Abanin and L. S. Levitov, "Conformal invariance and shape-dependent conductance of graphene samples," *Physical Review B*, vol. **78**, p. 035416, (2008).

[89] J. Iqbal *et al.*, "Characterization of low-resistance ohmic contacts to a two-dimensional electron gas in a GaAs/AlGaAs heterostructure.," *The European Physical Journal Applied Physics*, vol. **89**, p. 20101, (2020).

[90] J. A. Pals *et al.*, "Non-equilibrium superconductivity in homogeneous thin films," *Physics Reports*, vol. **89**, p. 323–390, (1982).

[91] G. Deutscher *et al.*, "Percolation description of granular superconductors," *Physical Review B*, vol. **21**, p. 5041–5047, (1980).

[92] O. Entin-Wohlman, A. Kapitulnik, and Y. Shapira, "Dependence of T_c on the normal-state resistivity in granular superconductors," *Physical Review B*, vol. **24**, p. 6464–6468, (1981).

[93] D. Massarotti *et al.*, "What happens in Josephson junctions at high critical current densities," *Low Temperature Physics*, vol. **43**, p. 816–823, (2017).

[94] E. Simaánek, *Inhomogeneous Superconductors: Granular and Quantum Effects*. Oxford University Press, (1994).

[95] R. Fazio and H. van der Zant, "Quantum phase transitions and vortex dynamics in superconducting networks," *Physics Reports*, vol. **355**, p. 235–334, (2001).

[96] J. Xiang *et al.*, "Ge/Si nanowire mesoscopic Josephson junctions," *Nature Nanotechnology*, vol. **1**, p. 208–213, (2006).

[97] E. Zhitlukhina *et al.*, "Anomalous Inner-Gap Structure in Transport Characteristics of Superconducting Junctions with Degraded Interfaces," *Nanoscale Research Letters*, vol. **11**, (2016).

[98] B. A. Aminov *et al.*, "Quasiparticle current in ballistic constrictions with finite transparencies of interfaces," *Physical Review B*, vol. **53**, p. 365–373, (1996).

[99] M. Watanabe and D. B. Haviland, "Quantum effects in small-capacitance single Josephson junctions," *Physical Review B*, vol. **67**, p. 094505, (2003).

[100] T. Matsui and H. Ohta, "Low-voltage negative-resistance mixers of nanometer SNS junctions," *IEEE Transactions on Applied Superconductivity*, vol. **11**, p. 191–195, (2001).

[101] R. E. Howard *et al.*, "Small-area high-current-density Josephson junctions," *Applied Physics Letters*, vol. **35**, p. 879–881, (1979).

[102] I. S. Beloborodov *et al.*, "Granular electronic systems," *Reviews of Modern Physics*, vol. **79**, p. 469–518, (2007).

[103] R. F. Hoyt *et al.*, "Low-temperature specific heat and superconductivity of α-phase Au-Ga alloys," *Physical Review B*, vol. **14**, pp. 441–447, (1976).

[104] R. Hein *et al.*, "Superconducting properties of AuGa and $AuGa_2$ compounds," *Journal of the Less Common Metals*, vol. **62**, pp. 197–209, (1978).

[105] R. A. Hein *et al.*, "The $AuGa_2$ Dilemma - Superconducting version," *High-Pressure and Low-Temperature Physics*, pp. 419–431, (1978).

[106] J. H. Wernick *et al.*, "Superconducting, thermal and magnetic susceptibility behavior of some intermetallic compounds with the fluorite structure," *Journal of Physics and Chemistry of Solids*, vol. **30**, pp. 1949–1956, (1969).

[107] H. R. Khan, "Superconducting gold alloys," *Gold Bulletin*, vol. **17**, pp. 94–100, (1984).

[108] D. C. Hamilton *et al.*, "Some new superconducting compounds," *Journal of Physics and Chemistry of Solids*, vol. **26**, pp. 665–667, (1965).

[109] S. Schöttl *et al.*, "Evaluation of SRD_{1000} superconductive reference devices," *Journal of Low Temperature Physics*, vol. **138**, pp. 941–946, (2005).

[110] S. J. Soulen *et al.*, "The superconductive energy gap of $AuAl_2$," *Physica B + C*, vol. **108**, p. 823–824, (1981).

[111] R. Hoyt and A. Mota, "Superconductivity in α-phase alloys of Cu, Ag and Au," *Solid State Communications*, vol. **18**, pp. 139 – 142, (1976).

[112] A. Barańska *et al.*, "Ohmic contacts for room-temperature AlGaAs/GaAs quantum cascade lasers (QCL)," *Optica Applicata*, vol. **43**, p. 5–15, (2013).

[113] T. J. Magee and J. Peng, "Electron Microscopy Studies of the Alloying Behavior of Au on GaAs," *Physica Status Solidi (a)*, vol. **32**, pp. 695–700, (1975).

[114] J. M. Vandenberg and E. Kinsbron, "Interface reaction of gold films with n-type $Ga_{0.7}Al_{0.3}As$ and GaAs," *Thin Solid Films*, vol. **65**, pp. 259–265, (1980).

[115] A. J. Barcz, E. Kaminska, and A. Piotrowska, "Fundamental and practical aspects of alloying encapsulated gold-based contacts to GaAs," *Thin Solid Films*, vol. **149**, pp. 251–260, (1987).

[116] D. C. Hamilton *et al.*, "Some new superconducting compounds," *Journal of Physics and Chemistry of Solids*, vol. **26**, pp. 665–667, (1965).

[117] B. Chen *et al.*, "Large magnetoresistance and superconductivity in α-gallium single crystals," *Npj Quantum Materials*, vol. **3**, p. 40, (2018).

[118] H. L. Luo, M. F. Merriam, and D. C. Hamilton, "Superconducting metastable compounds," *Science*, vol. **145**, pp. 581–583, (1964).

[119] A. C. Mota and R. F. Hoyt, "Dependence of the superconducting transition temperature on electron per atom ratio and lattice deformation in noble metal alloys," *Solid State Communications*, vol. **20**, pp. 1025–1028, (1976).

[120] C. Granqvist and T. Claeson, "The superconducting energy gap measured by tunneling into quench-condensed germanium-gold," *Physics Letters A*, vol. **39**, pp. 271–272, (1972).

[121] Y. Seguchi, T. Tsuboi, and T. Suzuki, "Magnetic-field-enhanced superconductivity in alloy films of Au-Ge," *Journal of the Physical Society of Japan*, vol. **62**, pp. 2564–2567, (1993).

[122] Y. Shih *et al.*, "Summary Abstract: Transmission electron microscopy studies of the microstructure of AuNiGe ohmic contact to n-type GaAs," *Journal of Vacuum Science & Technology A: Vacuum, Surfaces, and Films*, vol. **5**, p. 1485–1486, (1987).

[123] C. J. Cooke and W. Hume-Rothery, "The equilibrium diagram of the system gold-gallium," *Journal of the Less Common Metals*, vol. **10**, pp. 42–51, (1966).

[124] D. Jendrzejczyk-Handzlik, "Thermodynamic study and re-optimization of the Au-Ga binary system," *Journal of Phase Equilibria and Diffusion*, vol. **38**, pp. 305–318, Jun (2017).

[125] R. Ginley, D. D. L. Chung, and D. Ginley, "Structural effects of heating gold-based contacts to Gallium Phosphide," *Solid-State Electronics*, vol. **27**, p. 137, (1983).

[126] X. Zeng and D. D. L. Chung, "In situ x-ray diffraction study of melting in gold contacts to Gallium Arsenide," *Solid-State Electronics*, vol. **27**, pp. 339–345, (1984).

[127] E. Beam and D. D. L. Chung, "Phase transitions in gold contacts to GaAs," *Thin Solid Films*, vol. **128**, p. 321–332, (1985).